Appendix A: Peer-Reviewed Papers

Simulating U-C Associations: An Experimental Approach to Modelling the Mineralization Processes in the Witwatersrand Basin, South Africa

Tremain H. Woods[a]

[a]School of Geosciences, Witwatersrand Basin Research Team, DST-NRF Centre of Excellence for Integrated Mineral and Energy Resource Analysis, Private Bag 3, WITS 2050, South Africa

Gillian R. Drennan[a]

[a]School of Geosciences, Witwatersrand Basin Research Initiative, DST-NRF Centre of Excellence for Integrated Mineral and Energy Resource Analysis, Private Bag 3, WITS 2050, South Africa

Gillian.drennan@wits.ac.za

Shane H. Durbach[b, c]

[b]Molecular Sciences Institute, School of Chemistry, University of the Witwatersrand, Johannesburg 2050, South Africa

[c]DST-NRF Centre of Excellence in Strong Materials, University of the Witwatersrand, Private Bag 3, WITS 2050, South Africa

Abstract

The Witwatersrand Basin is one of the largest sources of gold ever found. The highest concentrations of gold are found in close association with uranium and carbonaceous materials (the latter in the form of carbon seams and nodules). An attempt was made to recreate the U-C associations using the catalytic chemical vapour deposition (CCVD) technique using acetylene as a hydrocarbon source for the reaction. The technique resulted in the formation of carbon nanostructures (CNSs) on uranium-bearing powders at atmospheric pressure. In numerous successful experiments, CNSs were formed at temperatures between 300°C and 600°C. Although the mass increases of these uranium-bearing powders were small, TEM micrographs showed that CNSs (including: carbon nanotubes, nanofibers, sheet-like materials and complex spirals within larger tubes) were formed on the < 32 µm and the 32 - 75 µm powder size fractions. Visually the form of these experimental products was found to be similar to that of carbon seams in the Witwatersrand Basin, being completely encapsulated in carbonaceous material. Additionally the signatures of their Raman spectra closely matched that of carbon from the Basal and Carbon Leader Reefs in the Witwatersrand Basin. Significantly the growth of CNSs was found to be correlated with high concentrations of U, i.e. greater than 2000 µg/g, where the highest yields were observed at 600°C for the < 32 µm powder size fraction. However, anomalously high carbon growth of CNSs for samples with low concentrations of U were also noted. These anomalies were found to be the result of additional metal catalysts like: Cu, Sr and Mo, which were concentrated in the uraniferous powders. When U was leached from one such uraniferous powder (which also contained Cu, Sr and Mo) HILG19 < 32 µm the yield of CNSs decreased by 35%. This strongly suggested that although these other metals had played a role in catalysing CNSs formation, U played the more significant one. Hence this study has reported the first ever catalysed growth of CNSs on uranium-bearing powders, where their growth has been directly correlated to U. Based upon these observations, the mechanism proposed in this paper is therefore suggested to provide a possible explanation for the formation of carbon seams around uranium-bearing minerals in the Witwatersrand Basin.

46 Keywords. Experimental, Uranium, Carbon, Nanostructure, Witwatersrand Basin

47

1) Introduction

The Witwatersrand Basin is the single largest source of gold in the world (Frimmel, 2005) and has been studied and mined for well over 100 years. However, controversy still surrounds the genesis and details of the formation of the Witwatersrand Basin. The Witwatersrand Basin is a meta-sedimentary basin with abundant gold and uranium mineralisation (Phillips, 2011). Up to 40% of this gold is associated with hydrocarbons (Mossman *et al.*, 2008). Similarly, these carbons include uranium-bearing minerals in the Reefs (Gray *et al*., 1998). However, a number of contradictory theories regarding the origin of this association have been postulated (e.g. Gray *et al.*, 1998; Mossman *et al.*, 2008; Frimmel and Hennigh, 2015). This research proposes a potential mechanism for the formation of hydrocarbon materials (particularly carbon seam-like materials) around uranium-bearing minerals in the Witwatersrand Basin.

The Witwatersrand Basin is comprised of mainly quartzite, shale and conglomerate horizons (Feather and Koen, 1975). Gold, uranium and hydrocarbon materials occur in conglomerate layers within the reefs (Feather and Koen, 1975; Gray *et al.*, 1998). Initial models of formation accounted only for the sedimentological features, where the placer model was the prevalent view for many years (Smith and Minter, 1980; Koglin, Zeh, *et al*., 2010). However, the abundance of metamorphic minerals and hydrothermal features has caused some to question the validity of the placer model (Phillips *et al*., 1987; Phillips and Law, 1994). The current model of genesis that is most widely accepted for the Witwatersrand Basin, amongst modern researchers, is the modified placer model (Frimmel and Gartz, 1997; Robb *et al*., 1997; Mathur *et al.*, 2013; Large *et al.*, 2013). This model states that the gold in the Witwatersrand Basin was originally deposited as detrital grains by fluvial processes and was later remobilized (Robb and Meyer, 1995; Drennan et al., 1999; Mathur et al., 2013).

The origin of the sediments in the Witwatersrand Basin has long been agreed to be from a combined felsic/mafic source (Robb *et al*., 1991; Koglin, Frimmel, *et al*., 2010; Depiné *et al.*, 2013). The source of the sediments are believed to be from granite-greenstones (Robb *et al.*, 1991; Stanistreet and

McCarthy, 1991). Evidence from detrital zircons show that the closest modern analogue to the proposed source sediments are the greenstone belts of the Murchison Belt (Robb *et al*., 1997). The detrital gold and uranium that is concentrated in the Witwatersrand Basin is thought to have originated from this type of material which was then shaped by detrital processes and then deposited by fluvial systems when the basin formed (Robb *et al.*, 1991; Depiné *et al.*, 2013). The proceeding metamorphism and hydrothermal alteration then altered many of the materials within the Basin.

Hydrocarbons in the Witwatersrand Basin occur as either carbon seams up to a few centimetres thick, or nodules approximately 1 mm or less in diameter (Gray et al., 1998; Drennan et al., 1999; England et al., 2002). Hydrocarbon material in the seams exhibit 'fibres' or 'spindles' that appear to be perpendicular to the original seam boundaries (Gray *et al.*, 1998; Smieja-Król *et al.*, 2009). Hydrocarbon seams contain abundant uraninite grains (Minter, 1976). These uraninite grains are rounded in nature, but are also highly fractured and fragmented (Drennan and Robb, 2006). The shape of the hydrocarbon materials in the seam carbon as well as their maturity has provided evidence for researchers to believe that they were remobilized from their original source inside the Witwatersrand Basin (Schidlowski, 1981; Robb and Meyer, 1995). This is in contrast to the suggestion that these carbonaceous materials represent algal mats or solid matter that formed at the time of deposition of the placers (Hallbauer, 1975; Mossman *et al.*, 2008). Yet an alternative view is that migrating oils which carried, gold and other metals, gave rise to these hydrocarbons in the Witwatersrand Basin through radiolytic means (Robb and Meyer, 1995; Spangenberg and Frimmel, 2001). In this way it is believed that the resulting solid hydrocarbon materials concentrated gold in direct association with uraninite.

Further evidence for fluid remobilization of carbon and other elements including gold, was found in fluid inclusions from quartz veins. Drennan *et al.* (1999a) characterized the fluids within veins in the Witwatersrand Basin and identified as many as four fluid systems. These systems included: H_2O-CO_2, H_2O-CH_4-CO_2, CH_4-N_2 rich fluids as well as aqueous fluids (Drennan et al., 1999; Safonov and Prokof'ev, 2006). The presence of these fluids appears to constrain the conjectured temperatures of carbon

98 formation. For instance, Drennan *et al*. (1999a) have suggested that temperatures in the
99 Witwatersrand Basin were likely between 200 and 400°C. The presence of some metamorphic
100 minerals appears to support these conjectured temperatures, while others indicate that local
101 temperatures may have reached as high as 500°C (Phillips and Law, 2000; Safonov and Prokof'ev,
102 2006; Grové and Harris, 2010). Pressures in the Witwatersrand Basin were in the range of 1.5 to 3.00
103 KBar during metamorphism (Phillips and Law, 1994; Robb *et al.*, 1997; Safonov and Prokof'ev, 2006).

104 It is believed that these processes and subsequent conditions would have been vital to mineralisation
105 in the Witwatersrand Basin. The aim of this study was therefore to establish whether U-C associations
106 could be replicated in the context of the Witwatersrand Basin using experimental techniques like
107 chemical vapour deposition.

108

109 2) Methodology

110 2.1) Experimental Growth of Carbon Nanostructures (CNSs)

111 Researchers in the field of heterogeneous catalysis have been producing solid carbon nanostructures
112 (CNSs) on metallic surfaces for a number of years (Dupuis, 2005; Coville *et al.*, 2011). CNSs in the form
113 of light-weight single and multi-walled nanotubes, nanospheres, nanofibers and other nanoscale
114 carbon structures have been shown to display some extra-ordinary physical properties, including
115 their: super-strength, variable electrical conductivity, thermal conductivity, etc. (Thostenson *et al.*,
116 2001; Magrez *et al.*, 2005). Their ability to impart these properties into composites has made them
117 very interesting to chemists and material scientists (Thostenson *et al.*, 2001; Coleman *et al.*, 2006;
118 Coville *et al.*, 2011; Shaikjee and Coville, 2012). However, the organometallic association has been of
119 importance in these cases. CNSs have been formed in a reducing environment, where the carbon gas
120 was precipitated into a solid nanostructured phase onto the surfaces of: nano-dispersed copper,
121 cobalt, nickel and gold (Dupuis, 2005; Zhou *et al*., 2006; Durbach *et al*., 2009; Li *et al*., 2009). The
122 catalytic growth of CNSs onto a uranium-bearing powder is a novel idea, with previous studies having

123 only focussed on the effects of radiation on such materials (Krasheninnikov and Nordlund, 2004). For
124 instance energised particles have been shown to disrupt the growth of CNSs by creating junctions or
125 by welding them together (Krasheninnikov and Nordlund, 2004; Dupuis, 2005). In this work, the
126 catalytic chemical vapour deposition (CCVD) technique was adapted in an attempt to grow CNSs onto
127 uranium-bearing phases in granitic and meta-sedimentary material.

128 Approximately 100 mg of either granitic or meta-sedimentary powders were placed under CCVD
129 conditions. These powders had U concentrations which varied from 420-7900 μg/g (Table 1). Both
130 source rocks were from Swakop Uranium mine in Namibia. The chemical composition of each was
131 somewhat similar. The granite powder represented a relatively unaltered source similar to that
132 postulated for the provenance of the Witwatersrand Basin. The meta-sediment powder represented
133 sediments that had been exposed to surface processes, deposited and then metamorphosed to a
134 lower grade. All powders were crushed, milled and sieved into two different size fractions: <32 μm
135 and 32 μm - 75 μm, to establish if powder size had played any role in these reactions.

136 X-ray fluorescence (XRF) analyses were performed on both size fractions in order to establish the U
137 concentrations and whole rock geochemistry (see supplementary materials).

138 **Table 1.** Powdered substrates placed under CCVD conditions, arranged in increasing uranium
139 concentration per size fraction.

<32 μm powders			**32 - 75 μm powders**		
Sample	**Source Rock**	**U concentration (μg/g)**	**Sample**	**Source Rock**	**U concentration (μg/g)**
HILG19	Granite	504.77	HILG19	Granite	419.06
DH034	Granite	2445.83	DH034	Granite	1347.55
IDAM10	Meta-sediment	6729.08	HILG13	Granite	3251.84
HILG13	Granite	7904.27	IDAM10	Meta-sediment	5293.85

140

Upon closer examination it appeared that the sieving process had affected the concentration of certain trace elements within the powdered fractions (Table 1). For instance powders that were sieved to <32 µm were enriched in uranium as compared to their larger-sized counterparts (Table 1). In order to establish if uranium had played any role in these CCVD experiments, powders of both size fractions (i.e. <32 µm and 32 - 75 µm) of HILG19 were used where the uranium had been leeched from them. A mass of 1 g of each powder size fraction of HILG19 was subjected to 20 mL of a 0.1 M solution of sodium bicarbonate ($NaHCO_3$) and agitated on a shake-table for 6 hours. After leeching each mixture was centrifuged and the resulting powder separated off and dried at 50°C for 12 hrs. The concentration of U that was leeched in each case was quantified using inductively coupled plasma optical emission spectroscopy (ICP-OES). These powders had been selected as the low levels of U posed the least health and safety risks during the leeching process.

The experimental set-up for the CCVD technique used in these experiments is shown in Figure 1. Each of the powders referred to in Table 1 (as well as the leeched powder) were individually loaded into a quartz boat. The loaded boat was then placed into a quartz tube, into which hydrogen (H_2 - a reducing gas), acetylene (C_2H_2 – a carbon source) and argon (the inert carrier gas) were passed.

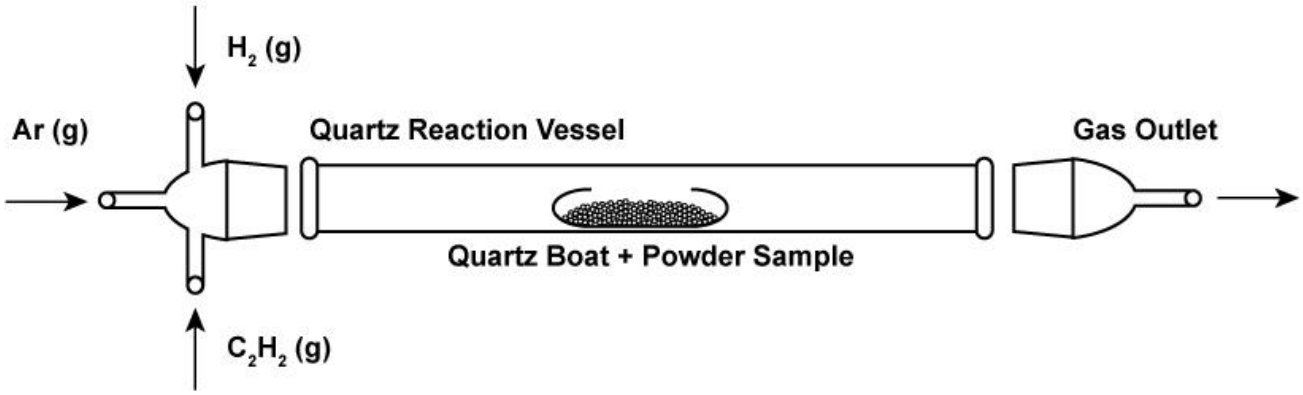

Figure 1. CCVD experimental set-up, showing a quartz reaction tube with gas inlets for: H_2, C_2H_2 and Ar with a gas outlet. A quartz boat with 100 mg of powder was loaded into the tube which was sealed and placed into a temperature-controlled furnace.

In every reaction the flow rate was kept constant at 100 mL/min for each of the 3 gasses. The quartz tube was sealed and heated in a temperature-controlled furnace from room temperature up to reaction temperatures of: 300°C, 450°C and 600°C at 10°C/min for various experiments. During the heating procedure argon was continually passed over the sample. Once the reaction temperature was achieved, hydrogen and then acetylene were introduced and the reaction was conducted for 2 hrs for all experiments.

2.2) Analytical Procedures

2.2.1) Bulk Geochemistry

Powdered uraniferous samples were analysed using X-ray fluorescence (XRF) spectroscopy at the Earth Sciences Laboratory at the University of the Witwatersrand. XRF data was obtained with the PANalytical PW2404 XRF spectrometer. Samples that were leeched of U were analysed using ICP-OES to determine the change in the amount of U. ICP-OES was chosen as only a small mass of powder was required for the technique, and the mass of powder that was available was limited. The analyses were conducted using a Spectro Genesis Spectrometer with a method designed to detect As, Sr, Mo, Cu and U.

2.1.2) Laser Raman Spectroscopy

Laser Raman spectroscopy (LRS) was used to acquire the spectral signature of the products that were synthesised. Spectra were acquired using the 514.5 nm line of an argon ion laser on a Horiba Jobin-Yvon LabRAM HR Raman spectrometer. The laser was focused onto the sample via a microscope objective and the backscattered light was dispersed onto a liquid nitrogen cooled CCD detector via a grating with 600 lines/mm.

2.2.3) Electron Microscopy

Each experiment was conducted in triplicate, where individual mass changes were recorded and averaged. Unreacted and reacted uranium bearing powders were mounted onto copper grids covered with lacy carbon mesh for analysis by transmission electron microscopy. A FEI Tecnai T12 transmission electron microscope (TEM) was then used at an accelerating voltage of 120 kV to capture electronic images of these uranium bearing powders and their reaction products. Additional images and analyses were obtained using scanning electron microscopy on a Zeiss Evo LS15 tungsten filament SEM platform. Images and electron dispersive X-ray spectroscopy (EDS) were conducted at 25kV with a beam current of ~ 1.3 nA. Spectra for EDS were analysed by a Bruker XFlash® 6|30 EDS detector.

2.2.4) Thermal Analysis

Thermogravimetric analysis (TGA) was used to analyse the resulting products of CCVD reactions. TGA analyses were performed by a Perkin Elmer STA 6000 thermogravimetric analyser. About 10 mg of each sample was placed in a ceramic pan and then placed in the instrument furnace. The temperature of the sample was increased from room temperature to 900°C at 10°C /min under an oxidative atmosphere (air, 50 mL/min).

3) Results

3.1) Product Mass

The initial uranium-bearing powders underwent changes as a result of being exposed to the above-mentioned CCVD conditions. This was confirmed both visually (by a change from a grey or red powder to a black one) as well as physically (by a mass increase). Negligible changes in mass were seen for all uraniferous powders at reaction temperatures of 300°C. When the reaction temperatures were increased to 450°C, the majority of the uraniferous powders changed colour to black and small mass increases were noted. However, the most significant changes occurred at 600°C, where the unconsolidated uraniferous powders became completely agglomerated within a black product and

took on the form of the quartz boat at the bottom or became colloidal at the unrestricted surface of the boat (Figures 2(a)-(b)).

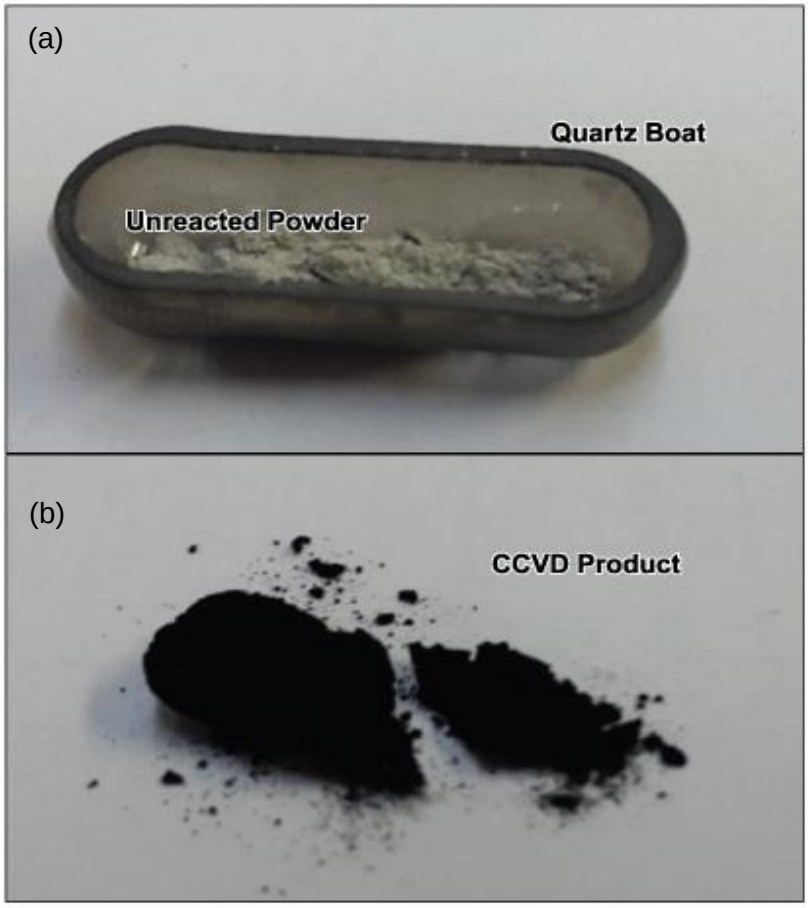

Figure 2. (a) Unreacted grey-coloured unconsolidated uraniferous powder in the quartz boat, (b) After the CCVD reaction at 600°C the uraniferous powder was black-coloured, agglomerated and the mass had increased. The product maintained the rounded form of the quartz boat and was friable.

In some cases (e.g. for the HLG 13 powder) the increase in the mass of the black product, formed under CCVD conditions, appeared to have been exponential with respect to the increase in reaction temperature (Figure 3). While reactions with the 32-75 µm uraniferous powders formed substantial masses of the black product, reactions with the <32 µm powders repeatedly resulted in significantly more products and displayed trends that were much more easily differentiated (although not for all samples). Coincidentally XRF analyses showed that this size range (i.e. <32 µm) had been enriched in uranium by the sieving process (Table 1).

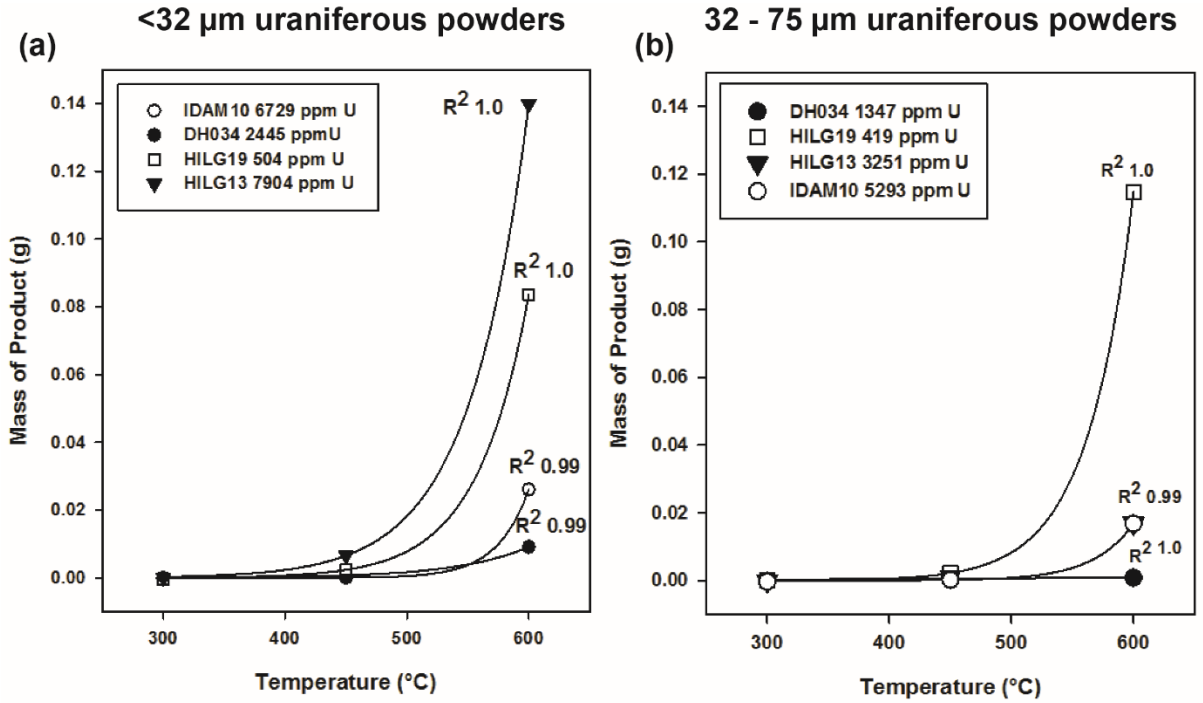

221

Figure 3. The masses of the black products formed (excluding the masses of the catalytic uraniferous powders) during CCVD growth with increasing reaction temperature for: **(a)** 32 µm uraniferous powders and **(b)** 75 µm uraniferous powders. Each point on the graph was the **average** of the three experiments used for that powder and temperature.

222

223 Significantly, data obtained for reactions run at 600°C suggested that (apart from the HLG19 powder)

224 a positive correlation existed between the concentration of uranium in these powders and the masses

225 of the black products that were formed (Figure 4).

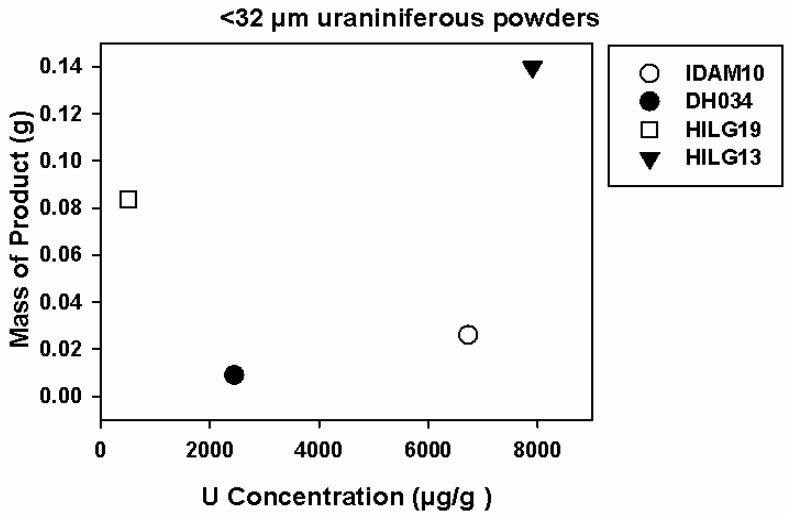

Figure 4. The mass of product formed versus uranium concentration (µg/g) for <32 µm uraniferous powders from reactions at 600°C under CCVD conditions.

226

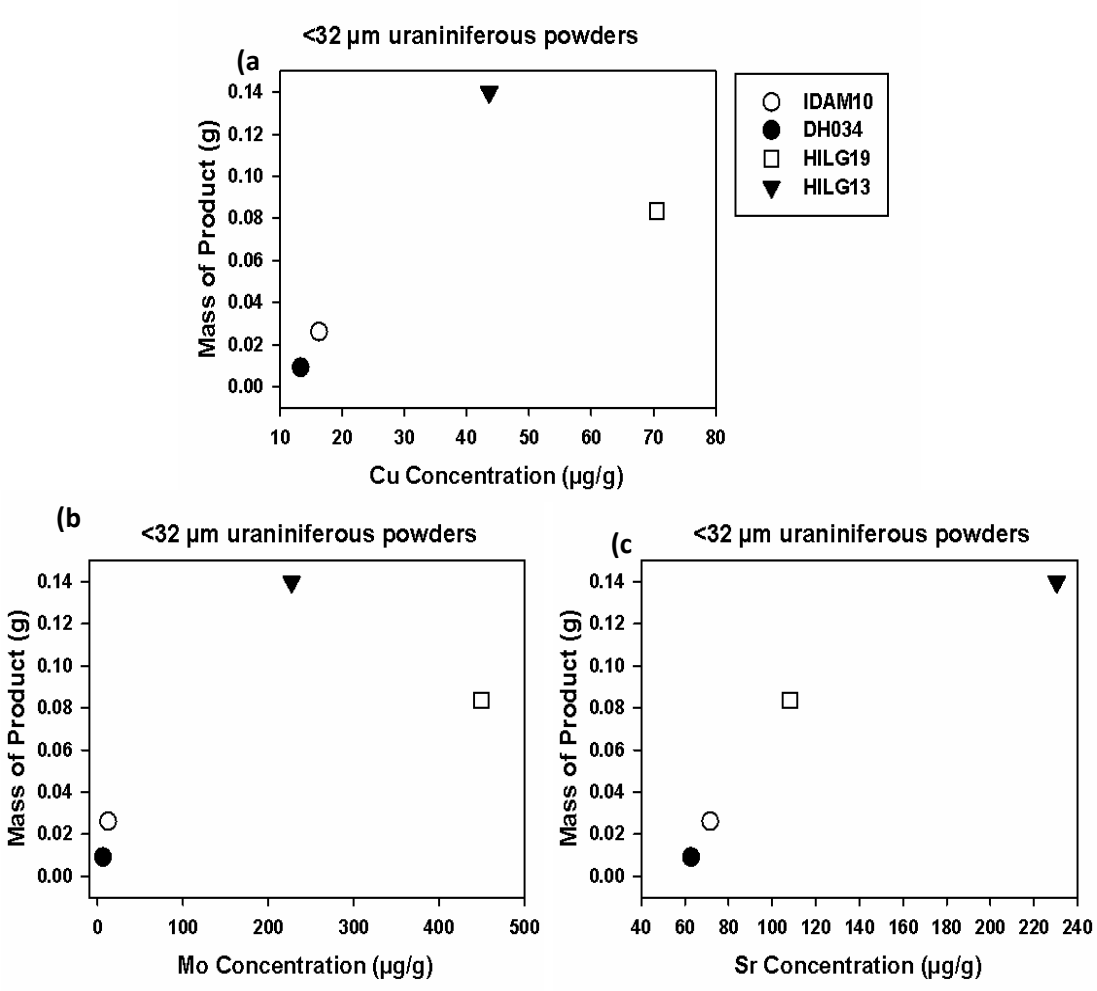

Figure 5. The mass of black-coloured product formed during the CCVD reaction with <32 µm uraniferous powders at 600°C, versus the concentration of: **(a)** Copper, **(b)** Molybdenum, and **(c)** Strontium.

227

Since the result for the HLG19 powder was an outlier, an explanation for its variance in the trend was sought. While a number of smaller variations in the elemental compositions of the starting uraniferous powders were noted, these did not show any correlation with the mass of black-coloured product which had formed. However, noticeable correlations for the concentrations of: Cu, Mo and Sr (see supplementary materials) with the masses of black-coloured product which had formed for the <32 µm powder fractions at 600°C were observed (Figure 5 (a)-(c)).

Therefore further investigation was required to establish the contribution of uranium towards the formation of the black products. Here a portion of the HILG19 <32 µm powder was exposed to conditions where uranium was leeched from it and then reacted at 600°C. The resulting powders had a similar visual appearance to that of the uranium enriched HILG19 powders. However, for the HILG19 <32 µm uranium powders that were exposed to 0.10 M sodium bicarbonate for 6 hrs, almost 50% of the U was leeched out and the mass of black product that formed was about 35% less than the original unleeched powders (Table 2). This strongly suggested that uranium played a key role in the formation of the black products, since the other elements were leeched by significantly lower quantities: Cu (0.6%), Mo (2.1%) and Sr (1.1%) (See Supplementary data).

Table 2. Product masses of standard HILG19 powders compared to those in which U had been leeched.

HILG19 <32 µm powder	
U concentration (µg/g)	**Average amount of black product formed**
Original Powder	
831	0.0836 g
After leeching	
429	0.0544 g

3.2) Laser Raman Spectrometry (LRS)

The significance of the reaction temperature and the nature of the black products formed on the uraniferous powders was investigated through LRS. Spectra from these black products (Figure 6) displayed the characteristic “D” (1350 cm^{-1}) and “G” (1580 cm^{-1}) peaks, associated with disordered and ordered/graphitic carbon respectively (Ferrari and Robertson, 2000; Reich and Thomsen, 2004). This confirmed that the black products, which had formed on these uraniferous powders, were indeed carbonaceous. These peaks were either too small to clearly differentiate or not present at all in reactions at 300°C. This observation was consistent with the negligible mass increases that were found under those conditions. Of interest was the observation that these peaks increased in intensity with reaction temperature and that at 600°C the “G” peaks in these spectra had significantly higher intensities than the “D” peaks. This suggested that the carbonaceous products that were formed under these conditions were more graphitic (and therefore more ordered) than those at lower reaction temperatures.

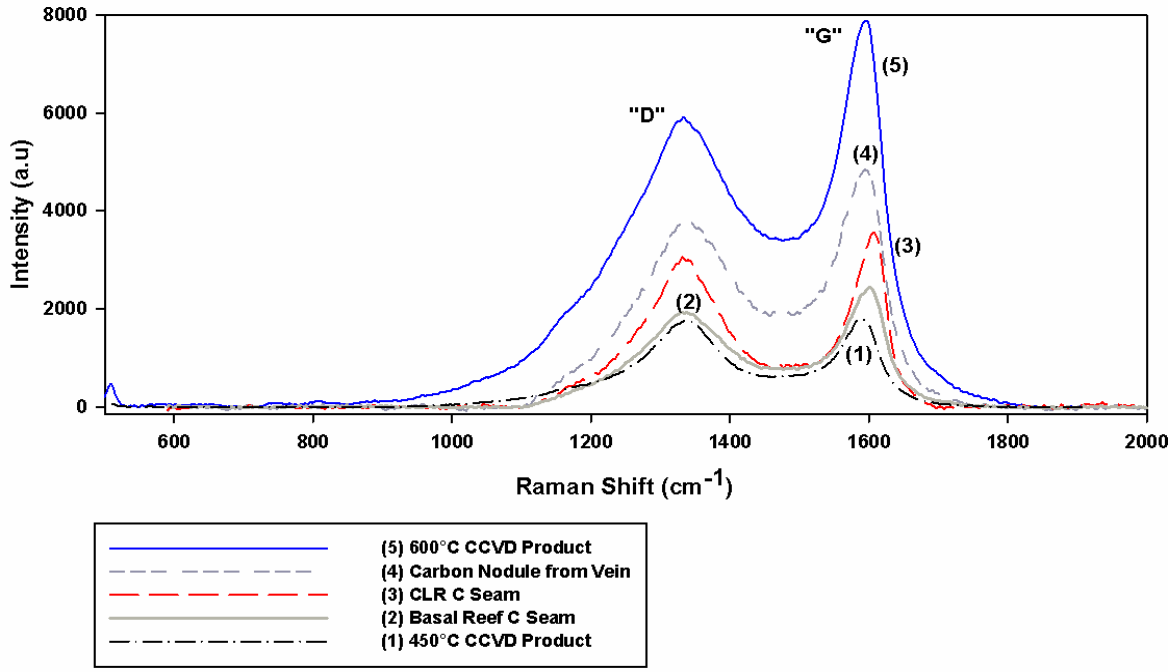

Figure 6. Laser Raman spectra of the CCVD products and Witwatersrand carbon samples. **(1)** CCVD product from HILG19 <32 µm powder reacted at 450°C; **(2)** Basal Reef carbon seam powder; **(3)** CLR carbon seam powder; **(4)** Carbon nodule from a vug in a quartz vein cross-cutting the Beisa Reef; **(5)** CCVD product from HILG19 <32 µm powder reacted at 600°C

Witwatersrand hydrocarbon from the CLR, Basal Reef and a carbon nodule from a vug in a quartz vein cross-cutting the Beisa Reef have also been examined using LRS. Spectra (Figure 6) from the CCVD products in this study were compared with those from Witwatersrand carbonaceous materials (Landais *et al*., 1990; Robb *et al*., 1994; Drennan and Robb, 2006). While the intensities were variable, it was found that the two peaks were very similar in position for the Witwatersrand hydrocarbon and the carbonaceous products formed by CCVD. The intensity ratio i.e. I_D/I_G which measured the area under the graph for the "D" and "G" peaks was then compared (Table 3). The average I_D/I_G ratio for the Witwatersrand hydrocarbon samples was 0.84 and was similar to the average I_D/I_G ratio for the CCVD products that formed at 450°C i.e. 0.80. This suggested a similarity in the types of carbonaceous materials that were present in both sources.

Table 3. TGA and laser Raman data for the carbonaceous products formed by CCVD at 450°C and 600°C as compared with laser Raman data for Witwatersrand hydrocarbons.

	450°C CCVD Products		**600°C CCVD Products**	
	TGA T°	I_D/I_G	*TGA T°*	I_D/I_G
IDAM10, 32 µm	580	0.85	640	1.04
DH034, 32 µm	N/A	0.77	620	0.90
HILG13, 32 µm	500	0.80	596	0.93
HILG19, 32 µm	504	0.78	611	1.01
IDAM10, 75 µm	N/A	0.89	620	0.96
DH034, 75 µm	N/A	0.75	598	0.87
HILG13, 75 µm	494	0.78	590	0.99
HILG19, 75 µm	514	0.78	523	0.97
Witwatersrand Hydrocarbon			I_D/I_G	
Carbon Nodule from Beisa Reef			0.81	

Carbon Seam from CLR	0.87
Carbon Seam from Basal Reef	0.82

274

275 3.3) Thermogravimetric Analyses

276 Thermogravimetric analyses were performed on the carbonaceous products from HILG19 <32 µm that
277 were formed at 450°C and 600°C to ascertain their thermal stability and hence their graphitic nature.
278 First derivatives of the TGA data for the carbonaceous products formed at 450°C and 600°C provided
279 the temperature maxima where each of these products combusted (Figure 7).

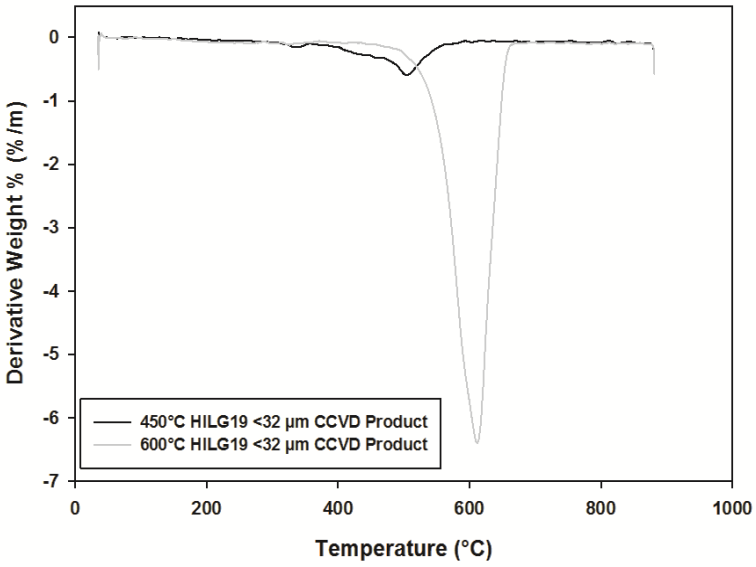

Figure 7. The first derivative curve of the TGA analyses of the CCVD products (for HILG19 powders <32 µm) from experiments at: 450°C and 600°C.

280

281 Data obtained by the TGA analyses revealed that the temperature maximum of the carbonaceous
282 products formed on the HILG19 powder at 600°C was higher than at 450°C. This suggested that the
283 thermal stability and hence the graphitic (ordered) nature of the HILG19 <32 µm products improved
284 as the reaction temperature was increased. This observation was found to be consistent with that
285 made by LRS. Likewise, when the first derivatives of the TGA data as well as the I_D/I_G ratios were
286 compared with one another this same trend was found for all of the uraniferous powders that were
287 assessed under CCVD conditions (Table 3).

3.4) Electron Microscopy of the CCVD Products

TEM was used in order to identify the nature and the quantity of carbonaceous products that were formed during the CCVD reactions as compared with the Witwatersrand hydrocarbon materials. Micrographs of the products from: 300°C CCVD reactions (Figures 8 (a)-(b)), 450°C CCVD reactions (Figures 8 (c)) and 600°C CCVD reactions (Figures 8 (d)-(e)); revealed that CNSs had formed on the crystalline particles of the uraniferous powders. The TEM micrographs revealed that very small quantities of CNSs appeared to have begun to grow from the surface or the subsurface of the uraniferous particles (U) at 300°C (Figure 8(a) & 8(b)). This observation was consistent with the negligible mass increases and poor detections of these materials by LRS under these conditions. CNSs with more discernible structures were far more apparent at 450°C (Figure 8 (c)). Fairly uniform-shaped, rough-textured carbon nanotubes/nanofibers appeared to grow from some of the uraniferous powders.

Similarly the greatest quantity of carbonaceous products were noted to have been formed at 600°C (Figure 8 (d) & (e)), which was consistent with previous observations. CNSs that were formed included: sheet-like carbonaceous materials (8 (d)-1), spiral or helical shaped carbon nanofibers (8 (d)-2), carbon nanotubes (8 (d)-3) and complex spiral-shaped carbon nanofibers within larger carbon nanostructures (Figure 8 (e)). In each case the CNSs that grew were found to be in direct association with the uraniferous particles (labelled U). The experimental products were also compared to crushed seam carbon from the Carbon Leader Reef (CLR) in the Witwatersrand Basin (Figure 8 (f)). Carbon materials that were present in the seam carbon were found to surround the solid uraninite (U) particles (100 – 200 nm), in a manner similar to which was seen in the CCVD products in this study. These carbonaceous materials had a sheet-like form. Whenever an attempt was made to more closely observe these materials in the seam carbon, by increasing the intensity of the electron beam, it was noted that they deformed into rounded globular masses. Consequently, highly nanostructured carbon

312 (e.g. carbon nanotubes/nanofibers and complex spirals) were not observed in the TEM micrographs

313 of the CLR from the Witwatersrand Basin

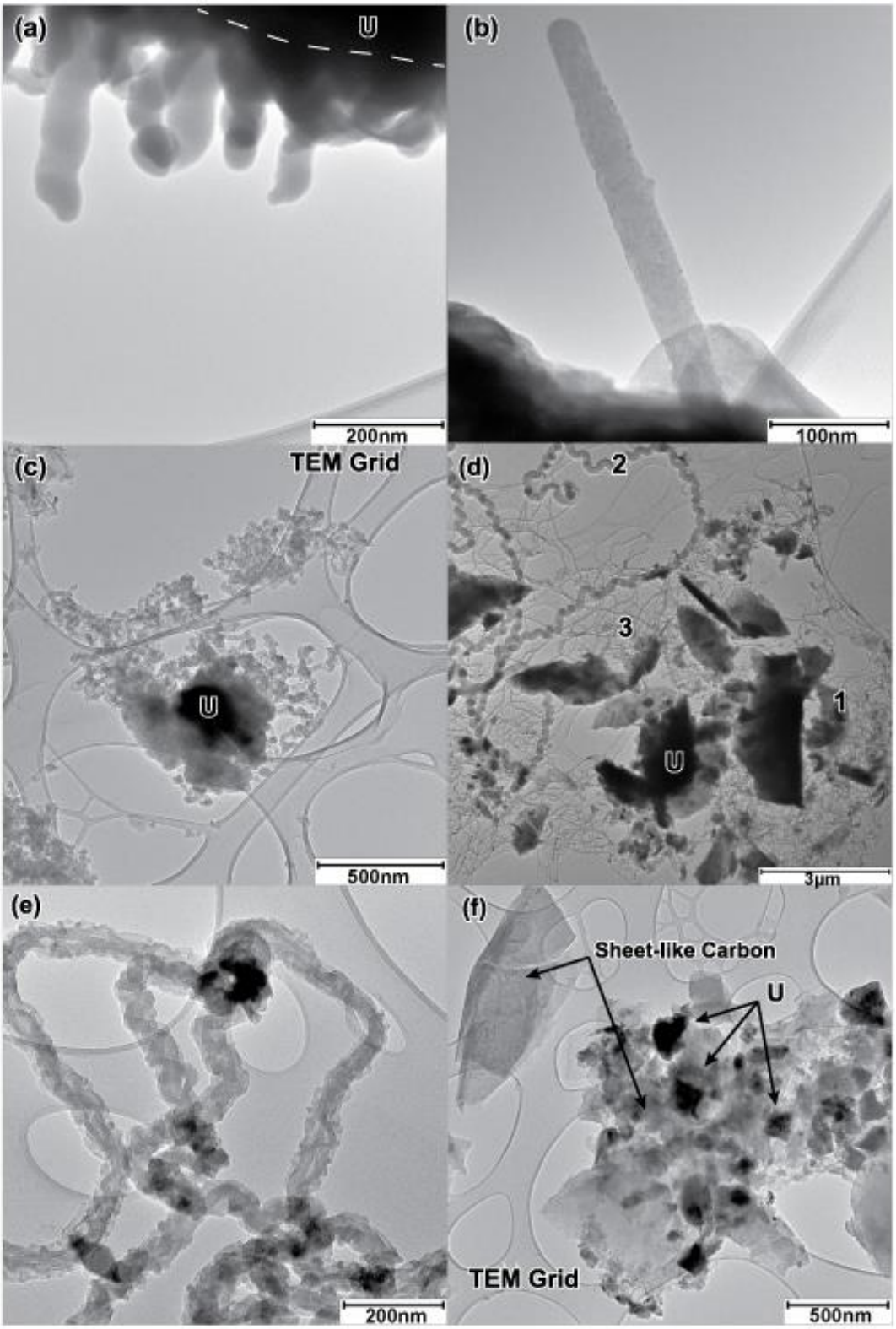

314

Figure 8. TEM micrographs of the CNSs that formed in the CCVD experiments: **(a)** IDAM10 <32 µm CCVD product reacted at 300°C showing small quantities of carbon nanofibers on the surface of uranium grains (U); **(b)** IDAM10 <32 µm CCVD product reacted at 300°C showing a carbon nanotube emerging from the surface of uranium grain; **(c)** HILG19 <32 µm CCVD product reacted at 450°C showing uniform rough textured CNSs; **(d)** HILG19 <32 µm CCVD product reacted at 600°C showing sheet-like carbonaceous materials-1, spiral-shaped carbon nanofibers-2, carbon nanotubes-3 and **(e)** HILG19 <32 µm CCVD product reacted at 600°C showing complex spiral-shaped carbon nanofibers within larger carbon nanostructures. (f) Micrograph of a crushed CLR sample showing uraninite grains (U) surrounded by sheet-like carbonaceous material. **NOTE**: In each image, the rounded forms in the background represent the lacy copper-carbon TEM grids that samples were mounted on.

However, when SEM images (Figure 9) of an ore block sample from the Beisa Reef (from the Witwatersrand Basin) and the black products formed at 600°C by CCVD were compared, a striking similarity was noticed. The Beisa Reef sample clearly showed the classic U-C association from the Witwatersrand Basin, where small uraninite grains were fragmented within a carbon seam (Figure 9 (a)). In comparison the CCVD product, which was kept in its agglomerated form and mounted in resin, also showed uraninite completely encompassed within carbon nanomaterials along with other silicate minerals (Figure 9 (b)).

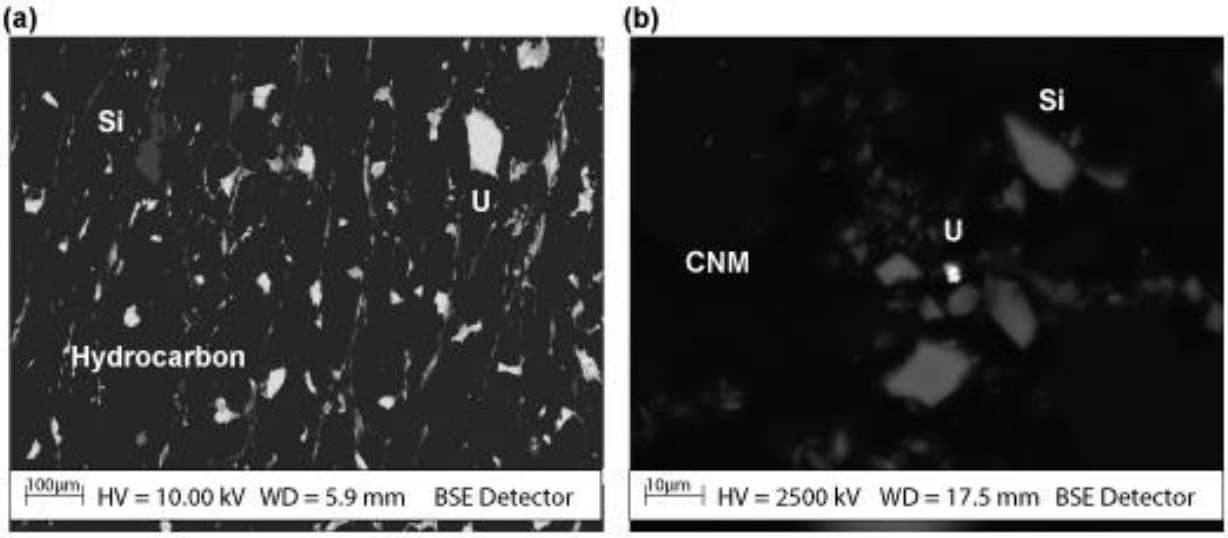

Figure 9. SEM images comparing (a) Beisa Reef carbon seam sample showing small fragmented uraninite grains (U) encompassed in hydrocarbon and, (b) CCVD product mounted in resin and polished, showing powdered uraninite (U) and silicate minerals surrounded by carbon nano materials

4) Discussion

The ability to form ordered solid carbon nanomaterials, from a liquid or gas phase, was of great interest to this work in the context of the Witwatersrand Basin. In over 100 experiments CNSs were grown onto uranium-bearing powders. This was also of interest as CNSs have been observed to grow best on metals such as: Co, Ni, Au and Cu (Moshkalyov *et al.*, 2004; Shaikjee and Coville, 2012). However, it was shown by leeching, that the U concentration was the most significant factor in the growth CNSs. Growth of CNSs in these experiments was found to be temperature dependant. At 300°C

very little CNSs grew over a period of 2 hrs; this indicated a very slow growth rate at this temperature. At 450°C very small quantities of CNSs grew and the data revealed that the carbon in these products was not very well ordered (as confirmed by TEM and LRS). At 600°C the highest growth rate of CNSs was noted. The carbon in the CNSs was more ordered and consisted of: sheet-like carbonaceous materials, spiral-shaped carbon nanofibers, carbon nanotubes and complex spiral-shaped carbon nanofibers.

A number of other elements (in trace quantities) were also associated with CNS formation i.e. Cu, Mo and Sr. While metals such as Cu, Ni, Co and Au have previously been used as catalysts in CNS formation (Thostenson *et al*., 2001; Zhou *et al*., 2006; Durbach *et al*., 2009; Li *et al*., 2009), these were usually carefully deposited in higher concentrations on nanoporous supports. Hence their preparation was vastly different to the powdered granitic/meta-sedimentary substrates that were used in this study. These natural powders demonstrated that even small concentrations of these metals (e.g. 70 µg/g of Cu), were sufficient to drastically enhance the growth of CNSs. Since the concentrations Cu, Mo and Sr were significantly lower than that of the uranium (other than in the HILG19 powders), it was clear that growth of CNSs in these natural powders was controlled by a complex interaction of uranium and these metals. This was especially apparent when the U in these samples were removed and the mass of CNSs that formed decreased by 35% for <32 µm powders of HILG19. These leeching experiments showed that even in the sample with the highest concentrations of Cu, Mo and Sr, when U was removed this reduced the quantity of CNSs that were formed.

With regards to the Witwatersrand Basin, there were at least two reasons why it was possible that the thermochemical reactions, which occurred in these CCVD experiments, could have played a role in hydrocarbon formation. Firstly, the reaction temperatures that were used to form these experimental products (i.e. 300-600°C) were plausible in the context of the Witwatersrand Basin. An indication of temperatures within the Witwatersrand Basin is provided by metamorphic minerals such as pyrophyllite, that is found in most gold mineralised areas (Phillips and Law, 1994; Drennan et al.,

1999). Metamorphic minerals are constrained between 300 and 400°C (Phillips and Law, 1994) and these phyllosilicate minerals are found within carbon seams (Phillips and Law, 1994; Fuchs et al., 2016). Witwatersrand carbonaceous materials are found in fluid inclusions in post-depositional veins. Temperatures for these carbonaceous materials are constrained as high as 500°C (Drennan et al., 1999). Therefore temperatures were consistently high enough for nanostructured growth to take place. It should also be noted that while growth rates were far lower at 300 and 450°C in these CCVD experiments, only a 2 hour reaction time was used. Whereas the Witwatersrand basin formed over hundreds of millions of years.

Secondly, it is plausible that if the correct gaseous hydrocarbon source was present, carbonaceous materials could have precipitated as nanostructured fibres, tubes and especially sheet-like carbons when in proximity to minerals containing U, Cu, Sr and/or Mo. It must be noted, however, that not all of these elements would have been specifically required for carbon to form in this way.

Laser Raman spectra of Witwatersrand seam and nodular carbon, when compared with the experimental products, revealed that their signatures were very similar to those that were synthesised by CCVD. This indicated that the ordering of the carbon in the Witwatersrand had a similar disordered-ordered carbon ratio (Ferrari and Robertson, 2000; Motchelaho *et al.*, 2011) as the experimental CCVD products that were grown. Indeed not only was the I_D/I_G ratio for LRS of the experimental products at 450°C similar to those of the Witwatersrand (Table 2), but their carbonaceous contents were also similar (Figure 8 (c) vs Figure 8 (a) and 8 (b)). Interestingly the habit and form of the CCVD products were very similar to the habit of natural Witwatersrand carbon. On a millimetre scale, the carbon grew around the contours of the boat and formed in columnar fashion perpendicular from the base of the quartz boat. At low temperatures the growth of the CNSs was quite linear and somewhat perpendicular to the surface of the powdered crystals. However, samples that grew at higher temperatures showed a variety of nanostructures, which appear to have grown in all directions off of the uraniferous powdered particles. TEM micrographs of the CLR from the Witwatersrand Basin

showed remarkable similarity to those of the CCVD products, and it was seen that the fibrous, sheet-like nature of the Witwatersrand hydrocarbon extended to the nanoscale as well.

To date the biggest unknown has been the specific role that uranium has played in the growth of carbon. The data from these experiments has shown that the growth of CNSs was correlated to the concentration of U.

5) Conclusion

CNSs have been experimentally grown onto uranium-bearing powders by CCVD experiments. In these experiments U, Cu, Mo and Sr, in unleeched uraniferous powders, were found to have been strongly correlated with carbon formation. However, when the uraniferous powder HILG19 was exposed to $NaHCO_3$, where the quantity of U removed was nearly 13 times that of Cu, Mo and Sr combined, the mass of CNSs that were grown dropped by 35%. This suggested that U played a more key role in the carbon which grew, while Cu, Mo and Sr played minor supporting roles. Significantly the growth of these carbon structures showed similarities (especially at 450°C) to the U-C associations seen in the Witwatersrand Basin. Hence this study has reported the first ever catalysed growth of CNSs on uranium-bearing powders, where their growth has been directly correlated to U

Acknowledgements

The research produced here-in would not be possible without the assistance of our collaborators, an exceptional amount of time and effort was contributed and we are grateful to each one. The paper is an output of the Witwatersrand Basin research team in the DST-NRF Centre of Excellence for Integrated Mineral and Energy Resource Analysis (CIMERA).

We are grateful to Ms M. Amwaama, Mr N. Pao and Mr A. Moya for their valuable input and ideas during the course of this study. Additionally, we are grateful to B. Chassoulas and T. Dzara for assistance with the equipment used in the experiments. Mr A. Mosai and Dr H Tutu for their assistance with leeching uranium. Finally, we are thankful to Professor A. Ziegler, Dr D. Reddy, Dr R. Erasmus and Mr J. Gerber of the Microscopy and Microanalysis at the University of the Witwatersrand for the assistance with the TEM and Raman analyses shown.

411 The DST-NRF Centre of Excellence in Strong Materials at the University of the Witwatersrand provided
412 funding, support and equipment during the course of this study. Other sources of financial assistance
413 included: the GSSA's REI funds, the Society for Economic Geologists' Hugh E. McKinstry fund, J C
414 Carstens Post Graduate Funds and the Faculty Research Committee of the University of the
415 Witwatersrand.

416

417 References

418 Coleman J. N., Khan U., Blau W. J. and Gun'ko Y. K. (2006) Small but strong: A review of the
419 mechanical properties of carbon nanotube–polymer composites. *Carbon* **44**, 1624–1652.

420 Coville N. J., Mhlanga S. D., Nxumalo E. N. and Shaikjee A. (2011) A review of shaped carbon
421 nanomaterials. *South African Journal of Science* **107**.

422 Depiné M., Frimmel H. E., Emsbo P., Koenig A. E. and Kern M. (2013) Trace element distribution in
423 uraninite from Mesoarchaean Witwatersrand conglomerates (South Africa) supports placer
424 model and magmatogenic source. *Mineralium Deposita* **48**, 423–435.

425 Drennan G. R., Boiron M. C., Cathelineau M. and Robb L. J. (1999) Characteristics of post-
426 depositional fluids in the Witwatersrand Basin. *Mineralogy and Petrology* **66**, 83–109. Available
427 at: http://link.springer.com/article/10.1007/BF01161723.

428 Drennan G. R. and Robb L. J. (2006) The nature of hydrocarbons and related fluids in the
429 Witwatersrand Basin, South Africa: Their role in metal redistribution. *Processes on the Early*
430 *Earth, Special Papers 405* **2405**, 353–386. Available at:
431 http://granite.geosociety.org/bookstore/default.asp?oID=0&catID=9&pID=SPE405.

432 Dupuis A. (2005) The catalyst in the CCVD of carbon nanotubes—a review. *Progress in Materials*
433 *Science* **50**, 929–961.

434 Durbach S. H., Krause R. W., Witcomb M. J. and Coville N. J. (2009) Synthesis of branched carbon

435 nanotubes using copper catalysts in a hydrogen-filled DC arc-discharger. *Carbon* **47**, 635–644.

436 England G. L., Rasmussen B., Krapez B. and Groves D. I. (2002) Archaean oil migration in the
437 Witwatersrand Basin of South Africa. *Journal of the Geological Society* **159**, 189–201.

438 Feather C. E. and Koen G. M. (1975) Mineralogy of the Witwatersrand Reefs. *Anglo American*
439 *Research Labs Report*.

440 Ferrari A. and Robertson J. (2000) Interpretation of Raman spectra of disordered and amorphous
441 carbon. *Physical Review B* **61**, 14095–14107.

442 Frimmel H. E. (2005) Archaean atmospheric evolution: Evidence from the Witwatersrand gold fields,
443 South Africa. *Earth-Science Reviews* **70**, 1–46.

444 Frimmel H. E. and Gartz V. H. (1997) Witwatersrand gold particle chemistry matches model of
445 metamorphosed, hydrothermally altered placer deposits. *Mineralium Deposita* **32**, 523–530.

446 Frimmel H. E. and Hennigh Q. (2015) First whiffs of atmospheric oxygen triggered onset of crustal
447 gold cycle. *Mineralium Deposita* **50**, 5–23.

448 Fuchs S., Williams-Jones A. E., Jackson S. E. and Przybylowicz W. J. (2016) Metal distribution in
449 pyrobitumen of the Carbon Leader Reef, Witwatersrand Supergroup, South Africa: Evidence for
450 liquid hydrocarbon ore fluids. *Chemical Geology* **426**, 45–59. Available at:
451 http://linkinghub.elsevier.com/retrieve/pii/S000925411630047X.

452 Gray G. J., Lawrence S. R., Kenyon K. and Cornford C. (1998) Nature and origin of “carbon” in the
453 Archaean Witwatersrand Basin, South Africa. *Journal of the Geological Society* **155**, 39–59.

454 Grové D. and Harris C. (2010) O- and H-isotope study of the Carbon Leader Reef at the Tau Tona and
455 Savuka mines (Western Deep Levels), South Africa: Implications for the origin and evolution of
456 Witwatersrand Basin fluids. *South African Journal of Geology* **113**, 73–86.

457 Hallbauer D. K. (1975) The plant origin of the Witwatersrand carbon. *Miner. Sci. Eng*. Available at:

https://scholar.google.co.za/scholar?q=hallbauer+1975+witwatersrand&btnG=&hl=en&as_sdt=0%2C5#0 [Accessed September 8, 2015].

Koglin N., Frimmel H. E., Minter W. E. L. and Brätz H. (2010) Trace-element characteristics of different pyrite types in Mesoarchaean to Palaeoproterozoic placer deposits. *Mineralium Deposita* **45**, 259–280.

Koglin N., Zeh A., Frimmel H. E. and Gerdes A. (2010) New constraints on the auriferous Witwatersrand sediment provenance from combined detrital zircon U-Pb and Lu-Hf isotope data for the Eldorado Reef (Central Rand Group, South Africa). *Precambrian Research* **183**, 817–824. Available at: http://dx.doi.org/10.1016/j.precamres.2010.09.009.

Krasheninnikov A. V. and Nordlund K. (2004) Irradiation effects in carbon nanotubes. *Nuclear Instruments and Methods in Physics Research Section B: Beam Interactions with Materials and Atoms* **216**, 355–366.

Landais P., Dubessy J., Poty B. and Robb L. J. (1990) Three examples illustrating the analysis of organic matter associated with uranium ores. *Organic Geochemistry* **16**, 601–608.

Large R., Meffre S., Burnett R., Guy B., Bull S., Gilbert S., Goemann K. and Danyushevsky L. (2013) Evidence for an intrabasinal source and multiple concentration processes in the formation of the carbon leader reef, Witwatersrand Supergroup, South Africa. *Economic Geology* **108**, 1215–1241.

Li Z., Dervishi E., Xu Y., Saini V., Mahmood M., Oshin O. D., Biris A. R. and Biris A. S. (2009) Carbon nanotube growth on calcium carbonate supported molybdenum-transition bimetal catalysts. *Catalysis Letters* **131**, 356–363.

Magrez A., Seo J. W., Mikó C., Hernádi K. and Forró L. (2005) Growth of carbon nanotubes with alkaline earth carbonate as support. *Journal of Physical Chemistry B* **109**, 10087–10091.

Mathur R., Gauert C., Ruiz J. and Linton P. (2013) Evidence for mixing of Re-Os isotopes at <2.7Ga

and support of a remobilized placer model in Witwatersrand sulfides and native Au. *Lithos* **164-167**, 65–73. Available at: http://dx.doi.org/10.1016/j.lithos.2012.11.015.

Minter W. E. L. (1976) Detrital gold, uranium, and pyrite concentrations related to sedimentology in the Precambrian Vaal Reef placer, Witwatersrand, South Africa. *Economic Geology* **71**, 157–176.

Moshkalyov S. A., Moreau A. L. D., Guttiérrez H. R., Cotta M. A. and Swart J. W. (2004) Carbon nanotubes growth by chemical vapor deposition using thin film nickel catalyst. *Materials Science and Engineering: B* **112**, 147–153.

Mossman D. J., Minter W. E. L., Dutkiewicz A., Hallbauer D. K., George S. C., Hennigh Q., Reimer T. O. and Horscroft F. D. (2008) The indigenous origin of Witwatersrand "carbon." *Precambrian Research* **164**, 173–186.

Motchelaho M. A. M., Xiong H., Moyo M., Jewell L. L. and Coville N. J. (2011) Effect of acid treatment on the surface of multiwalled carbon nanotubes prepared from Fe-Co supported on CaCO3: Correlation with Fischer-Tropsch catalyst activity. *Journal of Molecular Catalysis A: Chemical* **335**, 189–198. Available at: http://dx.doi.org/10.1016/j.molcata.2010.11.033.

Phillips G. N. (2011) Origin of Witwatersrand gold: a metamorphic devolatilisation-hydrothermal replacement model. *Applied Earth Science* **120**.

Phillips G. N. and Law J. D. M. (1994) Metamorphism of the Witwatersrand gold fields: A review. *Ore Geology Reviews* **9**, 1–31.

Phillips G. N. and Law J. D. M. (2000) Witwatersrand Gold Fields: Geology, Genesis, and Exploration. *SEG Review* **13**, 439–500.

Phillips G. N., Myers R. E. and Palmer J. A. (1987) Problems with the placer model for Witwatersrand gold. *Geology* **15**, 1027–1030.

Reich S. and Thomsen C. (2004) Raman spectroscopy of graphite. *Philosophical transactions. Series*

A, Mathematical, physical, and engineering sciences **362**, 2271–2288.

Robb L. J., Charlesworth E. G., Drennan G. R., Gibson R. L. and Tongu E. L. (1997) Tectono-metamorphic setting and paragenetic sequence of Au-U mineralisation in the Archaean Witwatersrand Basin, South Africa. *Australian Journal of Earth Sciences* **44**, 353–371.

Robb L. J., Davis D. W. and Kamo S. L. (1991) U-Pb Ages on Single Detrital Zircon Grains from the Witwatersrand Basin, South Africa: Constraints on the Age of Sedimentation and on the Evolution of Granites Adjacent to the Basin: A Reply. *The Journal of Geology* **99**, 495–496.

Robb L. J., Landais P., Meyer F. M. and Davis D. W. (1994) Nodular organic matter in granites; implications for the origin of“ kerogen” in the Witwatersrand Basin, South Africa. *Exploration and Mining Geology* **3**, 219–230.

Robb L. J. and Meyer M. F. (1995) The Witwatersrand Basin, South Africa: Geological framework and mineralization processes. *Ore Geology Reviews* **10**, 67–94.

Safonov Y. G. and Prokof'ev V. Y. (2006) Gold-bearing reefs of the Witwatersrand Basin: A model of synsedimentation hydrothermal formation. *Geology of Ore Deposits* **48**, 415–447.

Schidlowski M. (1981) Uraniferous constituents of the Witwatersrand conglomerates: ore-microscopic observations and implications for the Witwatersrand metallogeny. In *Genesis of Uranium- and Gold-Bearing Precambrian Quartz-Pebble Conglomerates. US Geological Survey Professional Paper 1161N* Golden, Colorado. pp. N1 – 29. Available at: http://inis.iaea.org/Search/search.aspx?orig_q=RN:15043646 [Accessed September 8, 2015].

Shaikjee A. and Coville N. J. (2012) The role of the hydrocarbon source on the growth of carbon materials. *Carbon* **50**, 3376–3398. Available at: http://www.sciencedirect.com/science/article/pii/S0008622312002722 [Accessed July 1, 2015].

Smieja-Król B., Duber S. and Rouzaud J. N. (2009) Multiscale organisation of organic matter

associated with gold and uranium minerals in the Witwatersrand basin, South Africa. *International Journal of Coal Geology* **78**, 77–88.

Smith N. D. and Minter W. E. L. (1980) Sedimentological controls of gold and uranium in two Witwatersrand paleoplacers. *Economic Geology* **75**, 1–14.

Spangenberg J. E. and Frimmel H. E. (2001) Basin-internal derivation of hydrocarbons in the Witwatersrand Basin, South Africa: evidence from bulk and molecular δ13C data. *Chemical Geology* **173**, 339–355.

Stanistreet I. G. and McCarthy T. S. (1991) Changing tectono-sedimentary scenarios relevant to the development of the Late Archaean Witwatersrand Basin. *Journal of African Earth Sciences (and the Middle East)* **13**, 65–81.

Thostenson E. T., Ren Z. and Chou T.-W. (2001) Advances in the science and technology of carbon nanotubes and their composites: a review. *Composites Science and Technology* **61**, 1899–1912.

Zhou W., Han Z., Wang J., Zhang Y., Jin Z., Sun X., Zhang Y., Yan C. and Li Y. (2006) Copper catalyzing growth of single-walled carbon nanotubes on substrates. *Nano Letters* **6**, 2987–2990.

Elemental Micromaps of Au-U-C associations in Carbon Seams from the Witwatersrand Basin: Evidence for Multi-Component, Multi-Fluid Remobilisation of Mineralisation

Tremain Hugh Encombe Woods

[1]School of Geosciences, Witwatersrand Basin Research Team, DST-NRF Centre of Excellence for Integrated Mineral and Energy Resource Analysis, Private Bag 3, WITS 2050, South Africa

Gillian Ruth Drennan

[1]School of Geosciences, Witwatersrand Basin Research Initiative, DST-NRF Centre of Excellence for Integrated Mineral and Energy Resource Analysis, Private Bag 3, WITS 2050, South Africa

Wojciech J. Przybylowicz

[2]Materials Research Department, iThemba LABS, National Research Foundation, P.O. Box 722, Somerset West 7129, South Africa

[3]AGH University of Science and Technology, Faculty of Physics & Applied Computer Science, Al. A. Mickiewicza 30, 30-059 Krakow, Poland

Abstract

The Witwatersrand Basin is the single largest deposit of gold ever found. Significant portions of gold and uranium minerals are associated with hydrocarbons. Although it is clear that the Au-U-C association is the result of a complex interaction between these elements, it is still contested how these associations were formed. Therefore, a study was undertaken to examine multiple carbon seams from a number of reefs in the Central Rand Group where mineralisation is most prominent. Specific focus was given to samples that had well-developed carbon seams, four samples from the selected Witwatersrand Reefs were analysed using micro-PIXE and micro-EBS elemental mapping. The result of the micromaps show that the hydrocarbons are enriched in dispersed K, Al, Cl and especially S. Au occurred with Ag, Hg and As in the spaces between the spindles. Fine-grained Si-rich phyllosilicate minerals, such as muscovite, sericite, pyrophylite and chlorite/chloritoid, also occurred in between the carbon spindles. Uraninite was also synonymous with carbon seams, the rounded grains are fragmented and displaced by hydrocarbons with small amounts of U,Pb and Th dispersed within the hydrocarbon.

The results support previous findings that the hydrocarbons were remobilised from previous fluid/oil phases. However, it is clear from this research that in addition to multiple fluid phases, there were a number of components capable of remobilising various elements. The components of the fluid included S-rich, Hydrocarbon-rich, Si-rich and CO_3-rich members, each capable of transporting a variety of elements. The hydrocarbon-rich component is capable of transporting and depositing Au, U, Cr, V, Mn, Ba, Hg, Ag and Ti, these elements are concentrated in the carbon seams and are known to be soluble in modern crude oils. The S-rich component is capable of remobilising Fe, Cu, Ni, Co and other metals. The Si-rich component would then have concentrated K, Al, Cl and other elements as phyllosilicates. Although paragenesis in carbon seams is complex, in “ideal conditions” the following would have occurred post-deposition: (I) detrital uraninite and/or metal-rich sulphides provided sites for hydrocarbons to

precipitate; (II) small amounts of secondary uranium minerals, gold and sulphides from the fluids between carbon spindles; (III) any remaining gold would be insoluble in the hydrocarbon-poor fluids and then would have precipitated locally; (IV) the left over fluids would be Si-rich and phyllosilicates would have formed.

This model of multiple components and multiple fluid phases during remobilisation is useful in explaining the variability of minerals in the Witwatersrand Basin. The lack of elements or components within the fluids would result in a departure from “ideal conditions”, and one or more of the minerals that would normally form would not. The model also incorporates and accounts for the sedimentary features, biogenic signature of hydrocarbons and intimate association between Au-U-C. The results of this study provide a mechanism that accounts for remobilisation of gold, uranium, carbon and sulphides in the Witwatersrand Basin via multi-component and multi-phase fluids.

Keywords Elemental Micromaps, Distribution, Witwatersrand, Gold, Uranium, Hydrocarbon

1) Introduction

The Witwatersrand Basin has been the focus of mining and research in South Africa for more than 100 years. As much as 40% of all gold ever extracted was mined from the Witwatersrand Basin (Fuchs *et al.*, 2016b). The Basin remains 10 times larger than the second largest goldfield discovered to date (Depiné *et al.*, 2013). There is an abundance of research covering almost every aspect of the Witwatersrand Basin, however there is still no consensus on the formation of the economic minerals. Key to understanding mineralisation processes in the basin is the relationship between gold, uranium and hydrocarbon (Au-U-C). Hydrocarbon is very often associated with the highest gold and uranium grades, however the formation of these Au-U-C associations is still contested. In this paper, elemental distributions of the Au-U-C associations found in carbon seams are investigated using petrography and micro-element mapping.

2) Geology and Stratigraphy

South Africa is host to the Witwatersrand Basin, a Mesoarchean basin spanning some 300 km across multiple provinces (Smith and Minter, 1980; Phillips and Powell, 2011). Figure 1 shows the extent of the basin and the location of the major goldfields. The Witwatersrand Basin is approximately 7 km thick and was deposited between 3074 and 2714 Ma (Robb *et al*., 1991; Koglin *et al*., 2010). The Witwatersrand Basin is composed of dominantly siliciclastic sediments: quartzite, shale and conglomerate, interlayered with minor volcanics (Young, 1917; Smith and Minter, 1980). The Witwatersrand Basin is underlain by the Kaapvaal Craton, this includes Archean granites and greenstones, and sediments of the Dominion Group.

The volcano-sedimentary sequence that comprises the Witwatersrand Basin is the erosional remnant of sediments deposited into two different tectonic environments (Stanistreet and McCarthy, 1991; Robb *et al.*, 1997) represented by the lower West Rand Group and the upper Central Rand Group (SACS, 1980).

The West Rand Group comprises the sediments deposited into an extensional basin in a shallow inland sea (Stanistreet and McCarthy, 1991), after which the Central Rand Group was deposited onto a foreland basin overlying the West Rand Group (Mellor and Banks, 1916). Sedimentation of the Witwatersrand Basin was terminated when the Ventersdorp Supergroup extruded flood basalt over the sediments (Van der Westhuizen *et al*., 1991; Hall *et al*., 1997).

Figure 2 shows the stratigraphy of the Witwatersrand Basin including the reefs and ages thereof. Highlighted in green are that reefs investigated in this study.

Following this, the Transvaal Supergroup was deposited above the Ventersdorp Supergroup to the North. The Bushveld Complex intruded the Transvaal Supergroup at approximately 2054 Ma (Eales and Cawthorn, 1996). Finally, the Vredefort impact structure was formed when a meteorite struck the basin close to the centre approximately 2020 Ma (Reimold and Gibson, 1996).

The entire Witwatersrand Basin is seen to have undergone green schist facies metamorphism to approximately 300°C and 1.5 - 3 KBar (Phillips and Powell, 2011; Phillips and Law, 1994) with peak temperatures being measured locally as high as 500°C (Drennan et al., 1999). Minerals that formed due to metamorphism include: pyrophyllite, chloritoid, chlorite, remobilised quartz and sericite (Phillips and Law, 2000; Rasmussen *et al*., 2007). Metamorphism in the Witwatersrand Basin is largely attributed to post-deposition burial, extrusion of the Ventersdorp Supergroup and emplacement of the Bushveld Complex (Rasmussen et al., 2007).

3) Mineralisation – models and multiple phases

3.1) Models of Formation

Formation of mineralisation is the key field of interest surrounding the Witwatersrand Basin currently. Most recent research focuses on the formation of the prominent minerals in the Witwatersrand Basin e.g. Frimmel and Hennigh (2015); Fuchs et al. (2016a); and Heinrich (2015). However, controversy still surrounds the genesis of many minerals present. There are 3 major models used to describe the origin or formation of the Witwatersrand mineralisation that have been reviewed and adapted through extensive research over the years.

The first model proposed by Mellor (1917) is the "placer model", that postulated that the sediments and economic minerals in the Witwatersrand Basin were deposited by rivers. Fluvial action was responsible for the distribution and concentration of gold, uranium and pyrite together with pebble lags. Evidence supported this model in many ways as the shape of the economic minerals as well as the distribution is usually correlated with sedimentary structures (Minter *et al*., 1993, 1988; Smith and Minter, 1980; Smits, 1984).

Phillips (1987) also noted that numerous economic minerals displayed evidence of hydrothermal emplacement or remobilization. As such, an alternative "hydrothermal model" was developed, which postulated that only a small amount of gold was emplaced by sedimentary processes and that the bulk of the gold was brought in by hydrothermal fluids from some unknown source outside the basin (Phillips, 1987; Phillips and Powell, 2011; Jolley *et al.*, 2004). While this model does provide some explanation for the strong hydrothermal signature of many economic minerals, it does not reconcile why the gold has such a strong sedimentary control (Frimmel *et al.*, 1999; Minter, 1999).

Researchers today favour a model that satisfies components of both the "placer" and "hydrothermal" models. The "modified placer model" (Robb et al., 1997; Drennan et al., 1999b; Stewart et al., 2004) agrees that the gold, uranium, pyrite and other minerals were washed into the basin by fluvial processes, however, they were later remobilized in hydrothermal fluids (Jolley *et al*., 2004; Hayward *et al*., 2005;

Simanovich, 2009; Horscroft *et al.*, 2011). This model favours multiple pulses of fluid movement and accounts for many of the mineralisation features, however a number of questions still persist (Mathur et al., 2013).

Researchers cite numerous factors such as anomalous concentrations of gold, source material of the gold, the unique Au-U-C structures, the lack of sizeable gold nuggets and the chemical variations of pyrite as problems with current models for mineralisation (Horscroft *et al*., 2011; Agangi *et al*., 2015). Frimmel and Hennigh (2015) and Heinrich (2015) provided an alternate model. They hypothesise that gold may have been dissolved from the land surface by highly acidic, meteoric waters and transported in solution into the basin. Once in the basin, gold from solution could have been precipitated near proposed biogenic forms in carbon seams that released free oxygen into the Witwatersrand sediments, altering the oxidation state. However, there are shortcomings with this view as the carbon seams seen in the basin are discontinuous and there is also gold in reefs with little or no carbonaceous materials.

3.2) Gold-Uranium-Hydrocarbon Associations in the Witwatersrand Basin

The key to the mineralisation appears to be the Au-U-C associations in the Witwatersrand Basin. Across the goldfields the highest gold grades are most often associated with high concentrations of hydrocarbon and uranium (Gray *et al*., 1998). As much as 60% of the gold in the reefs is contained in, or associated with, hydrocarbon (Smieja-Król *et al*., 2009). Hydrocarbon documented in the Witwatersrand Basin occurs as friable seams ranging from a few millimetres up to 30 cm in thickness, or it occurs as rounded nodules or "flyspeck carbon" along reef horizons (Gray *et al*., 1998; Mossman *et al*., 2008). Figure 3 shows the typical appearance of solid hydrocarbon in the Witwatersrand Basin.

Hydrocarbon also occurs within fluid inclusions associated with quartz veins that cross-cut the reef horizons as inclusion linings, as solid carbon nodules, and within the vapour phase. Where the carbon

145 seams are well-developed they have large spindles that taper upwards, and contain fragmented, initially
146 rounded uraninite grains (Smits, 1984; Drennan and Robb, 2006). Drennan and Robb (2006) also noted
147 that numerous generations of hydrocarbon could be seen cutting previously emplaced hydrocarbon. The
148 origin of the hydrocarbon was determined using carbon-isotope data that points to a biogenic origin of
149 the carbonaceous material from within the Witwatersrand Basin (Zumberge *et al*., 1978; Spangenberg
150 and Frimmel, 2001). Furthermore, the isotope data and rare earth element (REE) signatures indicate that
151 the hydrocarbon was sourced from the lower shale units in the Witwatersrand Basin (Spangenberg and
152 Frimmel, 2001; Fuchs *et al*., 2016b).

153 Uraninite in the Witwatersrand Basin has a bimodal occurrence, primary rounded grains and secondary
154 remobilised mineralisation (Feather and Koen, 1975; Smith and Minter, 1980). Primary uranium was
155 deposited by fluvial processes as uraninite from a granitic Archean hinterland (Minter, 1976; Pretorius,
156 1981). It is argued that this uraninite has remained largely in-situ due to the heavily immobile nature of
157 ^{235}U (Simpson and Bowles, 1977; Smits, 1984). However, uranium is also remobilised into secondary
158 coffinite, leucoxene and brannerite that occur concentrated as a fine grained mass or in veinlets within
159 the reefs (Feather and Koen, 1975; Minter *et al*., 1988).

160 *3.3) Fluids and the Transport of Hydrocarbon*

161 Fluids are essential to understanding the extent of remobilization of the Witwatersrand hydrocarbon
162 (Drennan et al., 1999; Parnell, 1999; Safonov and Prokof'ev, 2006). Fluid inclusion studies have found that
163 at least 4 fluid systems exist within the Witwatersrand Basin: H_2O-CO_2, H_2O-CH_4-CO_2, CH_4-N_2 enriched
164 fluids as well as aqueous fluids (Drennan et al., 1999). These systems are important as it was found that
165 remobilized gold occurs within the faults and veins that host the fluid inclusions as well as in the carbon
166 nodules extracted from the late-stage quartz veins (Drennan et al., 1999). The preservation of oils in fluid
167 inclusions led England *et al*. (2002) to conclude that oil migration was a strong factor in the Witwatersrand

168 Basin and had the potential to transport large concentrations of gold. The close relationship of
169 hydrocarbon to uranium provides an insight as to how the Au-U-C associations may have formed.
170 Schidlowski (1981) proposed that the radiation from detrital uraninite caused liquid hydrocarbons to
171 radiolytically polymerise and form solid hydrocarbon that encapsulated rounded uraninite grains.

172 Further evidence for the remobilisation and then precipitation of hydrocarbon was provided by Woods *et*
173 *al*. (2016). Carbon vapour deposition experiments showed that carbonaceous materials could be
174 precipitated as nanostructured carbon onto uranium-bearing granite powders (Woods *et al.*, 2016). The
175 results showed that uranium, and other metals acted as electron promoters that resulted in ordered nano
176 carbon precipitation.

177 Therefore many authors agree that there has been remobilisation of hydrocarbon, gold, pyrite and silicate
178 materials (Frimmel and Gartz, 1997; Frimmel and Minter, 2002; Koglin *et al*., 2010). However, the scale of
179 the remobilisation in the Witwatersrand Basin is contested. Gartz and Frimmel (1999) and Meier *et al.*
180 (2009) state that remobilisation occurred on a millimetre to centimetre scale and did not play a large role
181 in redistributing minerals after deposition. In contrast Jolley *et al*. (2004) and Parnell (1999) provided
182 evidence of remobilisation in the order of metres to hundreds of metres along faults and parallel to
183 bedding, that resulted in wide scale redistribution of minerals and metals in the Witwatersrand Basin.

184

185 *3.4) Elemental Transport in Oils/Brines*

186 Transport of elements in oils and brines is well documented in modern oilfields (Collins, 1975; Filby, 1994).
187 Currently there is strong focus on metal transport within oils and brines in hydrothermal systems
188 (Williams-Jones *et al*., 20094; Seward *et al*., 2013) . Numerous metals have been detected in crude oils,

these include: V, Ni, Cr, Mn, As, Au, Hg, U and Fe among others (Shah and Filby, 1970). Table 1 lists some common elements found in crude oils, only metals detected or analysed for are shown.

In addition to the metals that are found in oils, there are a number of other elements that are found in oilfield brines, these include: Ca, Mg, K and Sr amongst other (Kharaka *et al*., 1987). The temperatures for both oils and brines in modern analogues are within the ranges estimated for the Witwatersrand Basin - ~100°C in crude oils, and ~300°C in active hydrothermal systems (Seward *et al*., 2013). Gold was detected in crude oils (Shah and Filby,1970) in concentrations between 1 and 3 ppb. These concentrations do appear low, but this is to be expected as solubility for gold in crude oils was found to be 2 to 3 ppb at 100°C and as much as 50 ppb at 250°C (Zezin *et al*., 2007; Williams-Jones *et al*., 2009).

Therefore, modern fluid-metal solubility gives a suitable indication to the metals and elements that can be dissolved within oils and brines. Given that chemically these elements significantly interact with each other as ligands (oils) or complexes (brines), consideration should be given to this form of fluid transport in the context of the Witwatersrand Basin.

3.5) Previous PIXE data and research

Proton Induced X-ray Emission (PIXE) micro-mapping of elements found in-situ within their host minerals is an underutilised technique in the study of sediment-hosted mineralisation. PIXE is a non-destructive, well-understood and dependable method and should be used to determine the distribution of mobile and immobile elements as they occur in the Witwatersrand Basin. PIXE has previously been used to map elements within carbon nodules from quartz veins (Drennan and Robb, 2006) and carbonaceous material from the Carbon Leader Reef in the Witwatersrand Supergroup; and Black Reef from the Transvaal Supergroup (Fuchs *et al*., 2016a, 2016b).

211 The Witwatersrand Basin extends over a large area and variations in the Au-U-C associations are
212 significant from locality to locality. In this paper, we present numerous elemental micro-maps of well-
213 developed carbon seams from the Central Rand Group occurring in goldfields across the Basin.

214

215 **4) Sampling and Methodology**

216 *4.1) Samples and Petrology*

217 The selected samples came from the most significant reefs from across the Witwatersrand Goldfields.
218 Samples were selected based on reefs that contained seam carbon, uranium and gold. Many of the
219 samples were found in historical collections or museum collections obtained during the 1960's and 1970's.
220 These samples are unique as many modern studies cannot include them because the material has already
221 been mined out. **Table 2** Carbon bearing reef samples and their sample localityTable 2 shows the reef and
222 goldfield where samples were obtained. The samples were cut, embedded in epoxy and prepared as either
223 polished thin sections or polished ore blocks for detailed petrographic analyses. Areas of interest within
224 the samples were those that included hydrocarbon, uranium and gold in various proportions in seam
225 carbon. Thin sections and ore blocks that contained features of interest for PIXE analyses were coated
226 with a 60 nm layer of carbon.

227

228 *4.2) Instrumentation and PIXE Methodology*

229 The analyses were performed using the nuclear microprobe at the Materials Research Department of
230 iThemba LABS, Somerset West, South Africa. The facility uses a 6 MV single-ended Van de Graaff
231 accelerator and Oxford magnetic quadrupole triplet for beam focusing (Prozesky et al., 1995). A proton
232 beam of 3.0 MeV energy and ~500-800 pA current was focused to a 5 x 5 μm^2 spot and raster scanned

over selected areas of samples, using square or rectangular scan patterns of variable sizes (up to 2.5 mm x 2.5 mm scan sizes were possible) and a variable number of pixels (up to 128 x 128). PIXE spectra were registered with a Si (Li) detector (30 mm^2 active area, working distance 24 mm), positioned at a take-off angle of 135°. The effective energy resolution of the PIXE system (for the Mn Kα line) was 155-160 eV, measured for individual spectra. The X-ray energy range was set between 1 and 40 keV. Proton elastic backscattering (EBS) spectra were recorded with an annular Si surface barrier detector (100 μm thick) positioned at an average angle of 176°. Data were acquired in the event-by-event mode. The normalization of results was done using the integrated beam charge collected from the insulated specimen holder.

Each selected area was measured twice, using two different X-ray absorbers interposed between the sample and PIXE detector. Application of the thicker absorber (100 μm Al) restricted the practical X-ray energy range to above 4 keV (X-rays from the lighter elements were filtered out, and the detection of heavy elements was relatively enhanced). Additional measurements of low-energy X-rays (between 1-4 keV) were made using a 125 μm thick Be absorber. The proton current in this case was ~200-400 pA in order to reduce the number of pileups in the PIXE spectra.

Quantitative results were obtained using a standardless method employing GeoPIXE II software (Ryan, 2000). The calibration of the analytical system was tested by measurements of reference materials - pure elements, pure minerals and USGS (United States Geological Service) standards BIR-1 and BCR-2. Elemental mapping was performed using the Dynamic Analysis method (Ryan and Jamieson, 1993; Ryan et al., 1995; Ryan, 2000), which generates elemental images using series of X-ray lines (in this case K, L or M lines). The maps are (i) overlap-resolved, (ii) with subtracted background and (iii) quantitative, i.e. reported in ppm or wt. % units. Maps were constructed from the 4 analysed areas in the selected 4 samples using bitumen matrix compositions from scanned areas. The EBS maps of carbon distribution

were constructed using energy "gates" with background subtraction. In addition, PIXE and EBS spectra were extracted from smaller regions of arbitrarily selected shapes within maps. This selection was made on the basis of element distributions from PIXE maps. PIXE spectra from these regions were fitted using a full nonlinear deconvolution procedure (Ryan et al., 1990).

5) Results

5.1) "C" Reef carbon seam in contact with quartz vein

The "C" Reef sample (CREEF01) was taken from a carbon seam that was in contact with a bedding parallel quartz vein. The seam carbon in Figure 4 was cut perpendicular to the long axis of the spindles i.e. parallel to strike. Abundant hydrocarbon, seen as rounded spindles, comprises the seam. There are abundant uraninite grains that are generally rounded in shape, however internally they are highly fragmented and angular and contain carbonaceous material between them.

The sample also contains gold in between the spindles. There are abundant silicate minerals between the carbon spindles - these fine grained minerals include sericite/muscovite, chlorite, chloritoid and pyrophyllite. The PIXE micromaps Figure 5 show the distribution of elements throughout the seam carbon material. The silicate material between the spindles contains Al, Si, K, Ti, Cr and Fe in significant concentrations. Interestingly, there are small areas enriched in Ni and Y, however there is little S associated with other elements between the carbon spindles. Instead, S is strongly concentrated in the carbonaceous material, which cannot be seen in petrographic images. The RBS micromap of C shows that the occurrence of S and C are in the same regions. Gold in the sample has very strong concentration in between the spindles and is found to occur with As and Ag. Notably, S and Cl are both absent in the areas containing Au. Some carbon spindles show rims enriched in Ce. Ti also occurs in these Ce-rich regions,

however Ce does not occur in all the regions that contain Ti. The uranium minerals are strongly associated with U, Pb and Th. This is concentrated most strongly in the fractured uraninite grains. Small concentrations of U, Pb and Th in the silicate regions between spindles are associated with secondary brannerite and coffinite.

5.2) Carbon Leader Reef carbon seam cross-cut by calcite veinlets

Maps show carbon spindles trending in a top-to-bottom fashion (Figure 6) with calcite veinlets cross-cutting the spindles. The carbon spindles contain small concentrations of S, Cl and K (**Error! Reference source not found.Error! Reference source not found.**). There are also significant concentrations of Ti and V in lineaments along the spindles of the carbon (top-to--bottom trending). Between the spindles are Si concentrations associated with quartz. The most prominent feature of the sample is the calcite veinlets cross-cutting the sample.

The veinlets contain very high concentrations of Ca, and small concentrations of Mn, Fe and Sr. The sample contains small rounded concentrations of Pb associated with galena, and Y, Pb, Th and U associated with uraninite. There are a few rounded concentrations of Co, Ni, Cu, and As associated with cobaltite/gersdorffite. Small concentrations of Au are associated with Ag and Hg. Additionally, strong concentrations of Zr can be seen throughout the sample.

5.3) Basal Reef carbon spindles and multiple carbon forms

Sample LGM3 is taken parallel to the spindles of a carbon seam (Figure 8).

As with previous carbon seams PIXE micromaps (**Error! Reference source not found.**) exhibit a strong concentration of S and hydrocarbon in the seam material. Within the seam there are high concentrations of Cl between the carbon spindles, diffuse concentrations of K and small intense areas of Ca concentrations. Additionally, small amounts of Si and Al are found between the carbon spindles. The most prominent feature of this sample are the thin, intense Ti lineaments, best seen in the between 2 adjacent carbon spindles. Strongly concentrated along with the Ti in-between the spindles is V and Fe with some minor Cu. Gold in this sample is associated with As, Ag and Hg, and is aligned parallel to and between the carbon spindles.

However, the gold mineralisation does not occur in the same space between the spindles as the Ti. Additionally, Au is completely surrounded by hydrocarbon. This is in contrast to the "C" Reef sample (**Error! Reference source not found.**) where gold was strongly concentrated between the spindles. The small, rounded and intense Pb, Th and U concentrations are associated with the uraninite grains in the carbon seam. In this sample the uraninite grains occur as small crystals with relatively angular edges, which is very different from the "fragmented rounded uraninite" in the "C" Reef sample.

5.4) Vaal Reef carbon seam spindles and pyrite

Sample MGS6512 contains a carbon seam less than 1 mm thick from the Vaal Reef (Figure 10).

The area analysed using PIXE encompasses a perpendicular section through an oblong carbon spindle. The analysed area only contains a small amount of Si in between the carbon spindle (Figure 11), and the low concentrations of Si show that the larger carbon spindle is made up of a number of smaller spindles. The carbon spindles contain high concentrations of P, S, Ca and minor concentrations of dispersed Mn, Ni and

Y. There are small areas of high Cu, Zn, Ag and Au concentrations within the carbon seams. The carbon spindle has a rim enriched in Ti, V and Cr. Rare Earth Elements (REE) also occur within the Y-rich regions, however it is difficult to identify exactly which REE are present. Possible REE include: Ce, Pr, Nd, Pm, Gd, Dy and Er. Finally, the fractured irregular grains of uraninite are associated with strong concentrations of Pb, Th and U. These elements are also dispersed at low concentrations throughout the carbon seam.

6) Discussion

Due to very complex distribution of elements, PIXE mapping was verified by the results obtained from smaller regions selected within mapped areas. PIXE spectra from these areas were fitted using a full nonlinear deconvolution procedure (refer to supplementary materials). It should be noted that attention was principally given to the distribution patterns of elements rather than quantitative results as quantitative results. The quantitative values might have been affected by high variability of the matrix composition within mapped areas. The most notable feature of the carbon seam material analysed is the variability from locality to locality. Indeed, even within the same reef researchers have noted that gold grades, uranium and pyrite concentrations are variable (Feather and Koen, 1975; Smith and Minter, 1980) and carbon seams may be discontinuous over a larger area.

Uranium within the hydrocarbon is seen as (I) detrital rounded grains that are fragmented and contain hydrocarbon between the fragmented grains and as (II) secondary brannerite and coffinite contained within the silicate material and micro scale inclusions in the seam material. Gold is interpreted to be remobilised because it is concentrated between carbon spindles and is associated with concentrations of Ag, Hg and As. It is unlikely that these elements would have remained associated with the gold and would themselves have been remobilised during post- depositional processes if all mineralisation was purely detrital. The carbon seams have small concentrations of K, Cl, Ca and P, all of which are highly mobile and

capable of complexing with a variety of metals (Rollinson, 2014). However, the most significant elemental association with hydrocarbon is S. Invariably wherever the seam carbon occurs S occurs disseminated throughout the hydrocarbon but not as a sulphide mineral. This could indicate that carbon and SO_2 or H_2S acted within the fluid and transported the mobile elements. Both hydrocarbons and H_2S have been reported previously from fluid inclusion microthermometry studies (Drennan et al., 1999; Spangenberg and Frimmel, 2001). The presence of S and C in a single fluid does provide a potential mechanism for remobilisation wherein S is capable of remobilising certain elements (Fe, Cu, Ni, Co and other metals) and hydrocarbons transporting different elements (Au, U, Cr, V, Mn, Ba, Hg, Ag and Ti). These elemental associations are clearly seen in PIXE micromaps.

In addition, Si-rich material concentrated K, Al, and minor Cl. CO_3-rich fluids concentrated Ca, Mn, Fe and Sr in calcite veins cross-cutting some carbon seams. The presence of Si and S dispersed within the seam carbon also indicates that not only could multiple fluids have been present to concentrate metals, but they would also have been present at the similar times. This view of multiple fluids was proposed from fluid inclusion studies (Drennan et al., 1999; Frimmel et al., 1999) and tectonic processes associated with the Witwatersrand Basin (Stanistreet and McCarthy, 1991; Robb et al., 1997). There is an excellent correlation in the current study with the elements previously documented in the fluids from faults and veins within the Witwatersrand Basin. Additional evidence that hydrocarbon was formed from oil that transported metals is supported by the similarity of metals concentrated in the carbon seams to the abundance of metals seen in modern crude oils (Table 1).

Paragenesis of the minerals that would have formed from a system like this is extremely complex, especially one that accounts for the variability of gold, uranium, pyrite and hydrocarbon in the Witwatersrand Reefs. The proposed mechanism of multiple fluids in multiple fluid pulses would have been capable of remobilising different elements. This accounts for the distribution of elements within the

366 carbon seams in the Witwatersrand Basin. Uranium, pyrite and gold that were initially deposited and
367 reworked by sedimentary processes would have been concentrated along unconformities and lags. Post-
368 deposition, during the multiple phases of metamorphism, elements were remobilised into multiple fluids
369 comprising variable combinations of C-, Si-, and S-rich fluids. The specific areas of concentration in the
370 reefs were due to a change of system at the time of mineralisation; these changes include decrease in
371 pressure or temperature, increase in presence of metals that behaved as electron promoters/supports
372 and the presence of radioactive detrital uraninite. In the carbonaceous reefs investigated in this study,
373 paragenesis could have been as follows:

374 (I) Detrital uraninite and/or sulphide minerals provided sites for hydrocarbon to be precipitated,
375 via radiolytic polymerisation (Schidlowski, 1981) or nanostructured carbon growth (Woods et
376 al., 2016)
377 (II) During precipitation of hydrocarbon in well-developed seams, secondary uranium, gold and
378 sulphide minerals precipitated from the fluids between the carbon spindles
379 (III) Any remaining gold within the leftover fluids would no longer be soluble in a fluid deprived of
380 SO_2, CO_2 and Cl; and as such would have precipitated out between or onto the carbon spindles
381 (IV) The remaining fluids, now Si-rich would have formed muscovite, chlorite, sericite and
382 chloritoid; while the remaining S in the fluids would have formed cobaltite, chalcopyrite,
383 galena, gersdorffite, pyrite and sphalerite.

384 While this sequence is shown ideally by the well-developed seam carbon with excellent spindles and
385 fibrous structure, this does not occur consistently throughout the basin. For instance, where there is no
386 abundance of detrital uraninite, C would remain in solution until temperatures or pressures reduced
387 sufficiently for the hydrocarbon to precipitate as fairly unstructured nodules or as discontinuous

millimetre thick seams. Evidence for this can be seen in hydrothermal quartz veins cross-cutting the reefs where remobilised hydrocarbon precipitated out as rounded nodules (Drennan and Robb, 2015, 2006).

Finally, the distribution of REE in micro-xenotime crystals, seam carbon and silicates provides further motivation for complex multiphase fluids. REE are not typically mobile elements (Rollinson, 2014). The source of the REE in the hydrocarbon is therefore likely to be close by, most likely as traces within the uraninite, heavy minerals or platinoids (Cousins, 1973). PIXE data suggests, therefore, that C precipitated within the Witwatersrand Basin, originated from hydrothermal fluids. A possible source of the hydrocarbon-rich fluid may be the carbon-bearing shales in the lower Witwatersrand sediments (West Rand Group) which itself exhibits a biogenic origin (Mossman et al., 2008)

7) Conclusion

This research further enhances the value and ability of PIXE micromaps to detect metals and other elements in geological samples. Here, well-developed carbon seams from three prominent Witwatersrand Reefs were analysed. The results show that detrital uranium is synonymous with the development of spindles of carbon in the thick seams. Multiple fluids containing a combination of Si-, C- and S-rich phases could explain the variability of minerals within the Witwatersrand carbon seams.

Acknowledgements

The research produced here is the result of input from many collaborators' are grateful to each one. The paper is an output of the Witwatersrand Basin research team in the DST-NRF Centre of Excellence for Integrated Mineral and Energy Resource Analysis (CIMERA).

We are grateful to Prof. L.J. Robb and Prof. J.A. Kinnaird for their valuable input and ideas during the course of this study. Additionally, we are grateful to the Materials Sciences Division of iThemba LABS for the assistance during the long hours of data acquisition. We are thankful to Professor A. Ziegler, Mr J. Gerber of the Microscopy and Microanalysis at the University of the Witwatersrand for the assistance with carbon coating of the samples.

The research was funded by DST-NRF Centre of Excellence (CIMERA)at the University of the Witwatersrand for funding, support and equipment during the course of this study. Other sources of financial assistance included: the Geological Society of South Africa's Research Education and Investment funds, the Society for Economic Geologists' Hugh E. McKinstry fund, J C Carstens Post Graduate Funds and the Faculty Research Committee of the University of the Witwatersrand.

References

Agangi, A., Hofmann, A., Rollion-Bard, C., Marin-Carbonne, J., Cavalazzi, B., Large, R., Meffre, S., 2015. Gold accumulation in the Archaean Witwatersrand Basin, South Africa — Evidence from concentrically laminated pyrite. Earth-Science Reviews 140, 27–53. doi:10.1016/j.earscirev.2014.10.009

Collins, A., 1975. Geochemistry of oilfield waters. Elsevier.

Cousins, C.A., 1973. Platinoids in the Witwatersrand system. Journal of the South African Institute of Mining and Metallurgy 73, 184–199.

Depiné, M., Frimmel, H.E., Emsbo, P., Koenig, A.E., Kern, M., 2013. Trace element distribution in uraninite from Mesoarchaean Witwatersrand conglomerates (South Africa) supports placer model and magmatogenic source. Mineralium Deposita 48, 423–435. doi:10.1007/s00126-013-0458-3

Drennan, G.R., Boiron, M.C., Cathelineau, M., Robb, L.J., 1999. Characteristics of post-depositional fluids in the Witwatersrand Basin. Mineralogy and Petrology 66, 83–109.

Drennan, G.R., Robb, L.J., 2015. Hydrocarbons , fluids and metal redistribution in the Witwatersrand Basin , South Africa, in: SGA 13th Biennial Meeting. Nancy, France, pp. 3–6.

Drennan, G.R., Robb, L.J., 2006. The nature of hydrocarbons and related fluids in the Witwatersrand Basin, South Africa: Their role in metal redistribution. Processes on the Early Earth, Special Papers 405 2405, 353–386. doi:Doi 10.1130/2006.2405(18)

Eales, H.V., Cawthorn, R.G., 1996. Layered Intrusions, Developments in Petrology, Developments in Petrology. Elsevier. doi:10.1016/S0167-2894(96)80008-X

England, G.L., Rasmussen, B., Krapez, B., Groves, D.I., 2002. Archaean oil migration in the Witwatersrand Basin of South Africa. Journal of the Geological Society 159, 189–201. doi:10.1144/0016-764900-197

Feather, C.E., Koen, G.M., 1975. Mineralogy of the Witwatersrand Reefs. Anglo American Research Labs Report.

Filby, R.H., 1994. Origin and nature of trace element species in crude oils, bitumens and kerogens: implications for correlation and other geochemical studies. Geological Society, London, Special Publications 78, 203–219. doi:10.1144/GSL.SP.1994.078.01.15

Frimmel, H.E., Gartz, V.H., 1997. Witwatersrand gold particle chemistry matches model of metamorphosed, hydrothermally altered placer deposits. Mineralium Deposita 32, 523–530. doi:10.1007/s001260050119

Frimmel, H.E., Hallbauer, D.K., Gartz, V.H., 1999. Mineralogy and Petrology Gold mobilizing fluids in the Witwatersrand Basin : composition and possible sources. Mineralogy and Petrology 66, 55–81.

Frimmel, H.E., Hennigh, Q., 2015. First whiffs of atmospheric oxygen triggered onset of crustal gold cycle. Mineralium Deposita 50, 5–23. doi:10.1007/s00126-014-0574-8

Frimmel, H.E., Minter, W.E.L., 2002. Recent Developments Concerning the Geological History and Genesis of the Witwatersrand Gold Deposits , South Africa. Society of Economic Geologists 9, 17–45.

Fuchs, S., Williams-Jones, A.E., Jackson, S.E., Przybylowicz, W.J., 2016a. Metal distribution in pyrobitumen of the Carbon Leader Reef, Witwatersrand Supergroup, South Africa: Evidence for liquid hydrocarbon ore fluids. Chemical Geology 426, 45–59. doi:10.1016/j.chemgeo.2016.02.001

Fuchs, S., Williams-Jones, A.E., Przybylowicz, W.J., 2016b. The origin of the gold and uranium ores of the Black Reef Formation, Transvaal Supergroup, South Africa. Ore Geology Reviews 72, 149–164. doi:10.1016/j.oregeorev.2015.07.010

Gartz, V.H., Frimmel, H.E., 1999. Complex metasomatism of an Archaean placer in the Witwatersrand Basin. Economic Geology 94, 689–706. doi:10.2113/gsecongeo.94.5.689

Gray, G.J., Lawrence, S.R., Kenyon, K., Cornford, C., 1998. Nature and origin of “carbon” in the Archaean Witwatersrand Basin, South Africa. Journal of the Geological Society 155, 39–59. doi:10.1144/gsjgs.155.1.0039

Hall, R.C.B., Els, B.G., Mayer, J.J., 1997. The Ventersdorp Contact Reef: Final phase of the Witwatersrand basin, independent formation, or precursor to the ventersdorp supergroup ? South African Journal of Geology 100, 213–222.

Hayward, C.L., Reimold, W.U., Gibson, R.L., Robb, L.J., 2005. Gold mineralization within the Witwatersrand Basin, South Africa: evidence for a modified placer origin, and the role of the Vredefort impact event. Geological Society, London, Special Publications 248, 31–58. doi:10.1144/GSL.SP.2005.248.01.02

473 Heinrich, C.A., 2015. Witwatersrand gold deposits formed by volcanic rain, anoxic rivers and Archaean life.
474 Nature Geoscience 2–5. doi:10.1038/ngeo2344

475 Horscroft, F.D.M., Mossman, D.J., Reimer, T.O., Hennigh, Q., 2011. Witwatersrand Metallogenesis : the
476 Case for (Modified) Syngenesis. society for Sedimentary Geology 75–95.

477 Jolley, S.J., Freeman, S.R., Barnicoat, A.C., Phillips, G.N., Knipe, R.J., Pather, A., Fox, N.P.C., Strydom, D.,
478 Birch, M.T.G., Henderson, I.H.C., Rowland, T.W., 2004. Structural controls on Witwatersrand gold
479 mineralisation. Journal of Structural Geology 26, 1067–1086. doi:10.1016/j.jsg.2003.11.011

480 Kharaka, Y.K., Maest, A.S., Carothers, W.W., Law, L.M., Lamothe, P.J., Fries, T.L., 1987. Geochemistry of
481 metal-rich brines from central Mississippi Salt Dome basin, U.S.A. Applied Geochemistry 2, 543–561.
482 doi:10.1016/0883-2927(87)90008-4

483 Koglin, N., Zeh, A., Frimmel, H.E., Gerdes, A., 2010. New constraints on the auriferous Witwatersrand
484 sediment provenance from combined detrital zircon U-Pb and Lu-Hf isotope data for the Eldorado
485 Reef (Central Rand Group, South Africa). Precambrian Research 183, 817–824.
486 doi:10.1016/j.precamres.2010.09.009

487 Mathur, R., Gauert, C., Ruiz, J., Linton, P., 2013. Evidence for mixing of Re-Os isotopes at <2.7Ga and
488 support of a remobilized placer model in Witwatersrand sulfides and native Au. Lithos 164-167, 65–
489 73. doi:10.1016/j.lithos.2012.11.015

490 Meier, D.L., Heinrich, C. a., Watts, M. a., 2009. Mafic dikes displacing Witwatersrand gold reefs: Evidence
491 against metamorphic-hydrothermal ore formation. Geology 37, 607–610. doi:10.1130/G25657A.1

492 Mellor, E.T., Banks, E.H., 1916. Geological Map of the Witwatersrand Gold Field. Department of Mines
493 and Industries, Geological Survey.

494 Minter, W.E.L., 1999. Irrefutable detrital origin of Witwatersrand gold and evidence of Eolian signatures.
495 Economic Geology 94, 665–670. doi:10.2113/gsecongeo.94.5.665

496 Minter, W.E.L., 1976. Detrital gold, uranium, and pyrite concentrations related to sedimentology in the
497 Precambrian Vaal Reef placer, Witwatersrand, South Africa. Economic Geology 71, 157–176.
498 doi:10.2113/gsecongeo.71.1.157

499 Minter, W.E.L., Feather, C.E., Glatthaar, C.W., 1988. Sedimentological and mineralogical aspects of the
500 newly discovered Witwatersrand placer deposit that reflect Proterozoic weathering, Welkom gold
501 field, South Africa. Economic Geology 83, 481–491. doi:10.2113/gsecongeo.83.3.481

502 Minter, W.E.L., Goedhart, M., Knight, J., Frimmel, H.E., 1993. Morphology of Witwatersrand gold grains
503 from the Basal Reef: Evidence for their detrital origin. Economic Geology 88, 237–248.
504 doi:10.2113/gsecongeo.88.2.237

505 Mossman, D.J., Minter, W.E.L., Dutkiewicz, A., Hallbauer, D.K., George, S.C., Hennigh, Q., Reimer, T.O.,
506 Horscroft, F.D., 2008. The indigenous origin of Witwatersrand "carbon." Precambrian Research 164,
507 173–186. doi:10.1016/j.precamres.2008.04.008

508 Parnell, J., 1999. Petrographic evidence for emplacement of carbon into Witwatersrand conglomerates
509 under high fluid pressure. Journal of Sedimentary Research 69, 164–170. doi:10.2110/jsr.69.164

510 Phillips, G.N., 1987. Metamorphism of the Witwatersrand Gold Fields - Conditions during Peak
511 Metamorphism. Journal of Metamorphic Geology 5, 307–322 ST – Metamorphism of the
512 Witwatersrand Go.

513 Phillips, G.N., Law, J.D.M., 2000. Witwatersrand Gold Fields: Geology, Genesis, and Exploration. SEG
514 Review.

515 Phillips, G.N., Law, J.D.M., 1994. Metamorphism of the Witwatersrand gold fields: A review. Ore Geology
516 Reviews 9, 1–31. doi:10.1016/0169-1368(94)90017-5

517 Phillips, G.N., Myers, R.E., Palmer, J.A., 1987. Problems with the placer model for Witwatersrand gold.
518 Geology 15, 1027–1030. doi:10.1130/0091-7613(1987)15<1027:PWTPMF>2.0.CO;2

519 Phillips, G.N., Powell, R., 2011. Origin of Witwatersrand gold: a metamorphic devolatilisation–
520 hydrothermal replacement model. Applied Earth Science 120, 112–129.
521 doi:10.1179/1743275812Y.0000000005

522 Pretorius, D.A., 1981. Gold and Uranium in Quartz-Pebble Conglomerates. Economic Geology 75th Anniv,
523 117 – 138.

524 Prozesky, V.M., Przybylowicz, W.J., van Achterbergh, E., Churms, C.L., Pineda, C.A., Springhorn, K.A.,
525 Pilcher, J.V., Ryan, C.G., Kritzinger, J., Schmitt, H., Swart, T., 1995. The NAC nuclear microprobe
526 facility. Nuclear Inst. and Methods in Physics Research, B 104, 36–42. doi:10.1016/0168-
527 583X(95)00581-1

528 Rasmussen, B., Fletcher, I.R., Muhling, J.R., Mueller, A.G., Hall, G.C., 2007. Bushveld-aged fluid flow, peak
529 metamorphism, and gold mobilization in the Witwatersrand basin, South Africa: Constraints from in
530 situ SHRIMP U-Pb dating of monazite and xenotime. Geology 35, 931–934. doi:10.1130/G23588A.1

531 Reimold, W.U., Gibson, R.L., 1996. Geology and evolution of the Vredefort impact structure, South Africa.
532 Journal of African Earth Sciences 23, 125–162. doi:10.1016/S0899-5362(96)00059-0

533 Robb, L.J., Charlesworth, E.G., Drennan, G.R., Gibson, R.L., Tongu, E.L., 1997. Tectono-metamorphic
534 setting and paragenetic sequence of Au-U mineralisation in the Archaean Witwatersrand Basin,
535 South Africa. Australian Journal of Earth Sciences 44, 353–371. doi:10.1080/08120099708728317

Robb, L.J., Davis, D.W., Kamo, S.L., 1991. U-Pb Ages on Single Detrital Zircon Grains from the Witwatersrand Basin, South Africa: Constraints on the Age of Sedimentation and on the Evolution of Granites Adjacent to the Basin: A Reply. The Journal of Geology 99, 495–496. doi:10.1086/629510

Rollinson, H.R., 2014. Using Geochemical Data: Evaluation, Presentation, Interpretation, Longman Geochemistry. Taylor & Francis.

Ryan, C.G., 2000. Quantitative trace element imaging using PIXE and the nuclear microprobe. International Journal of Imaging Systems and Technology 11, 219–230. doi:10.1002/ima.1007

Ryan, C.G., Cousens, D.R., Sie, S.H., Griffin, W.L., Suter, G.F., Clayton, E., 1990. Quantitative pixe microanalysis of geological matemal using the CSIRO proton microprobe. Nuclear Inst. and Methods in Physics Research, B 47, 55–71. doi:10.1016/0168-583X(90)90047-X

Ryan, C.G., Jamieson, D.N., 1993. Dynamic analysis: on-line quantitative PIXE microanalysis and its use in overlap-resolved elemental mapping. Nuclear Inst. and Methods in Physics Research, B 77, 203–214. doi:10.1016/0168-583X(93)95545-G

Ryan, C.G., Jamieson, D.N., Churms, C.L., Pilcher, J. V., 1995. A new method for on-line true-elemental imaging using PIXE and the proton microprobe. Nuclear Inst. and Methods in Physics Research, B 104, 157–165. doi:10.1016/0168-583X(95)00404-1

SACS, 1980. Stratigraphy of South Africa, Part 1, in: Kent, L.E. (Ed.), Lithostratigraphy of the Republic of South Africa, South West Africa/Namibia and the Republics of Boputhatswana, Transkei and Venda: Handbook of the Geological Survey of South Africa,. p. 690.

Safonov, Y.G., Prokof'ev, V.Y., 2006. Gold-bearing reefs of the Witwatersrand Basin: A model of synsedimentation hydrothermal formation. Geology of Ore Deposits 48, 415–447. doi:10.1134/S1075701506060018

Schidlowski, M., 1981. Uraniferous constituents of the Witwatersrand conglomerates: ore-microscopic observations and implications for the Witwatersrand metallogeny, in: Genesis of Uranium- and Gold-Bearing Precambrian Quartz-Pebble Conglomerates. US Geological Survey Professional Paper 1161N. Golden, Colorado, pp. N1 – 29.

Seward, T.M., Williams-Jones, A.E., Migdisov, A.A., 2013. The Chemistry of Metal Transport and Deposition by Ore-Forming Hydrothermal Fluids, 2nd ed, Treatise on Geochemistry: Second Edition. Elsevier Ltd. doi:10.1016/B978-0-08-095975-7.01102-5

Shah, K.R., Filby, R.H., 1970. Determination of trace elements in petroleum by neutron activation analysis. Journal of Radioanalytical and Nuclear 6, 413 – 422.

Simanovich, I.M., 2009. Auriferous Precambrian conglomerates of Witwatersrand. Lithology and Mineral Resources 44, 497–509. doi:10.1134/S0024490209050071

Simpson, P.R., Bowles, J.F.W., 1977. Uranium Mineralization of the Witwatersrand and Dominion Reef Systems. Philosophical Transactions of the Royal Society A: Mathematical, Physical and Engineering Sciences 286, 527–548. doi:10.1098/rsta.1977.0130

Smieja-Król, B., Duber, S., Rouzaud, J.N., 2009. Multiscale organisation of organic matter associated with gold and uranium minerals in the Witwatersrand basin, South Africa. International Journal of Coal Geology 78, 77–88. doi:10.1016/j.coal.2008.09.007

Smith, N.D., Minter, W.E.L., 1980. Sedimentological controls of gold and uranium in two Witwatersrand paleoplacers. Economic Geology 75, 1–14. doi:10.2113/gsecongeo.75.1.1

Smits, G., 1984. in Witwatersrand 25.

Spangenberg, J.E., Frimmel, H.E., 2001. Basin-internal derivation of hydrocarbons in the Witwatersrand

579 Basin, South Africa: evidence from bulk and molecular δ13C data. Chemical Geology 173, 339–355.
580 doi:10.1016/S0009-2541(00)00283-7

581 Stanistreet, I.G., McCarthy, T.S., 1991. Changing tectono-sedimentary scenarios relevant to the
582 development of the Late Archaean Witwatersrand Basin. Journal of African Earth Sciences (and the
583 Middle East) 13, 65–81. doi:10.1016/0899-5362(91)90044-Y

584 Stewart, R. a., Reimold, W.U., Charlesworth, E.G., 2004. Tectonosedimentary model for the Central Rand
585 Goldfield, Witwatersrand Basin, South Africa. South African Journal of Geology 107, 603–618.
586 doi:10.2113/107.4.603

587 Van der Westhuizen, W.A., De Bruiyn, H., Meintjes, P.G., 1991. The Ventersdorp supergroup: an overview.
588 Journal of African Earth Sciences 13, 83–105. doi:10.1016/0899-5362(91)90045-Z

589 Williams-Jones, A.E., Bowell, R.J., Migdisov, A.A., 2009. Gold in solution. Elements 5, 281–287.
590 doi:10.2113/gselements.5.5.281

591 Woods, T.H., Drennan, G.R., Durbach, S.H., 2016. Simulating U-C Associations: An Experimental Approach
592 to Modelling the Mineralization Processes in the Witwatersrand Basin, South Africa. Geochimica et
593 Cosmochimica Acta Submitted.

594 Young, R.B., 1917. The Banket: A Study of the Auriferous Conglomerates of the Witwatersrand System
595 and the Associated Rocks. Gurney & Jackson, London.

596 Zezin, D.Y., Migdisov, A.A., Williams-Jones, A.E., 2007. The solubility of gold in hydrogen sulfide gas: An
597 experimental study. Geochimica et Cosmochimica Acta 71, 3070–3081.
598 doi:10.1016/j.gca.2007.04.005

599 Zumberge, J.E., Sigleo, A.C., Nagy, B., 1978. Molecular and Elemental Analyses of the Carbonaceous

Matter in the Gold and Uranium Bearing Vaal Reef Carbon Seams, Witwatersrand Sequence. Minerals Science and Engineering 10, 223–246.

64 REFERENCES

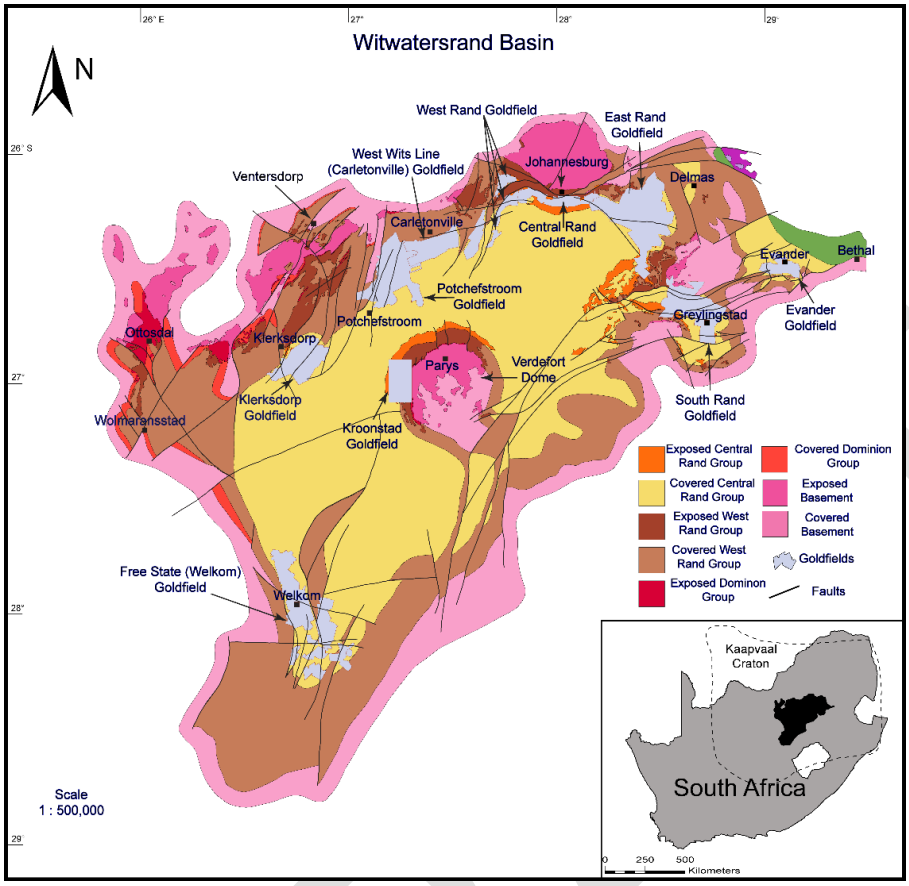

604

605 **Figure 1** Geological Map of the Witwatersrand Basin in South Africa, showing exposed and covered Central

606 and West Rand Groups. Also shown are goldfields, locality and major faults (Pretorius et al., 1986)

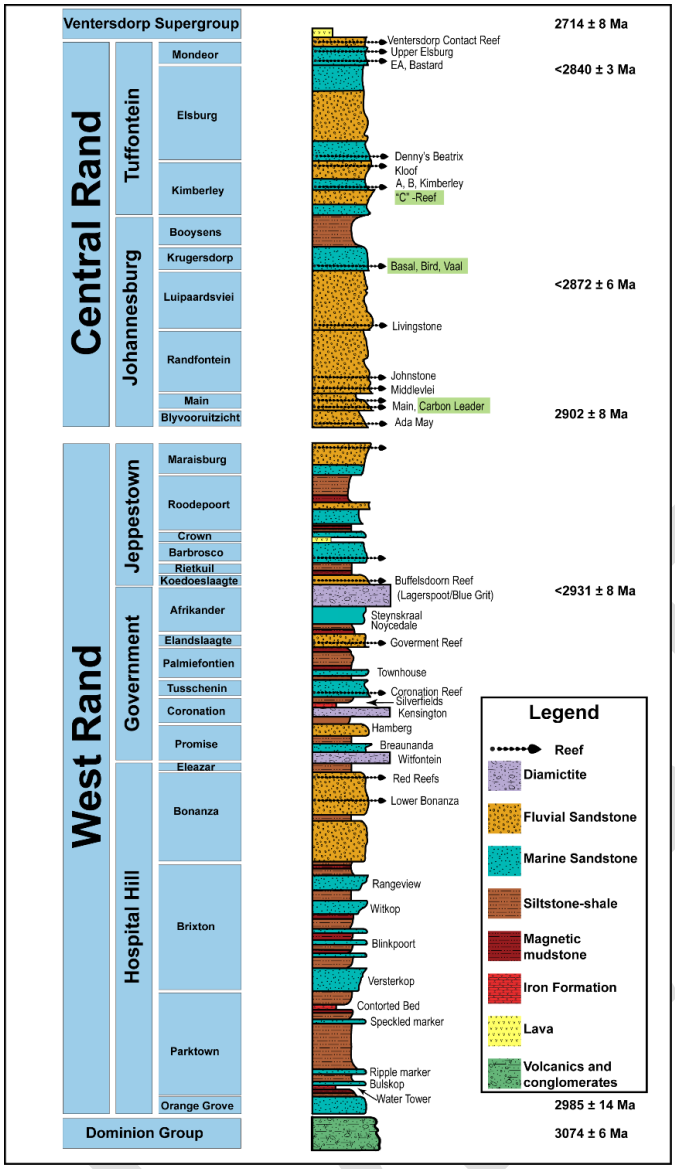

607

608 **Figure 2** Stratigraphic column of the Witwatersrand after Frimmel and Minter (2002). The reefs that

609 contained the carbon seams selected for this study are highlighted in green.

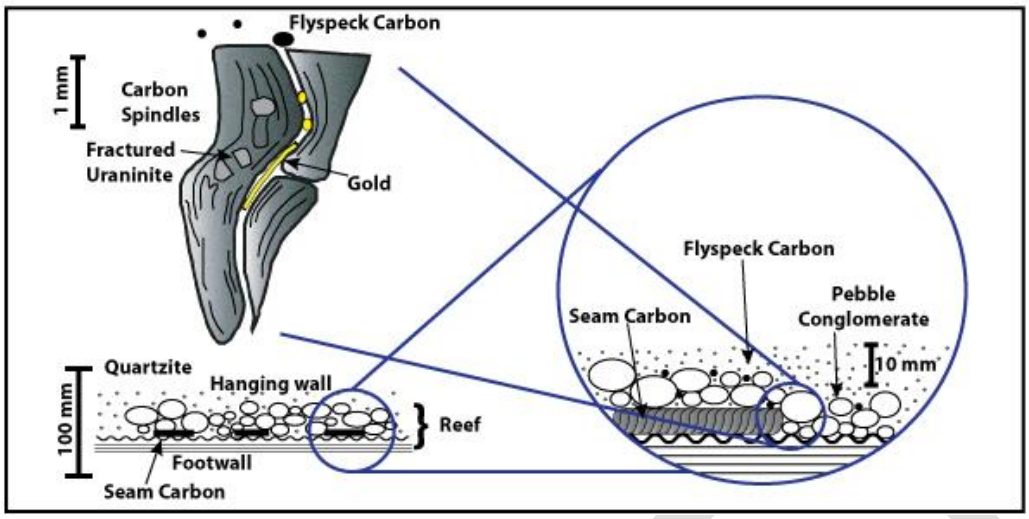

610

611 **Figure 3** Schematic diagram showing the typical distribution of carbon in gold reefs within the

612 Witwatersrand Basin. Modified after (Gray et al., 1998).

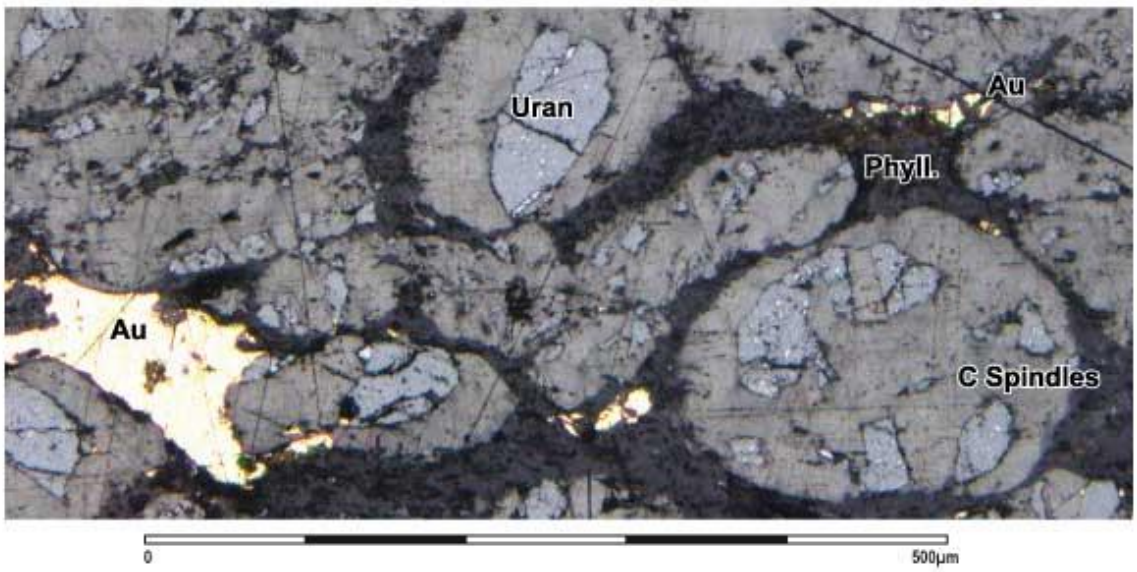

613

614 **Figure 4** Reflected light optical microscope image of CREEF01 from Blyvooruitzicht Gold Mine. The sample

615 is taken perpendicular to the elongated axis of the spindles in the carbon seam. Carbon spindles (C

616 Spindles) surround grains of uraninite (Uran) with some gold (Au) and phyllosilicate (Phyll.) between them.

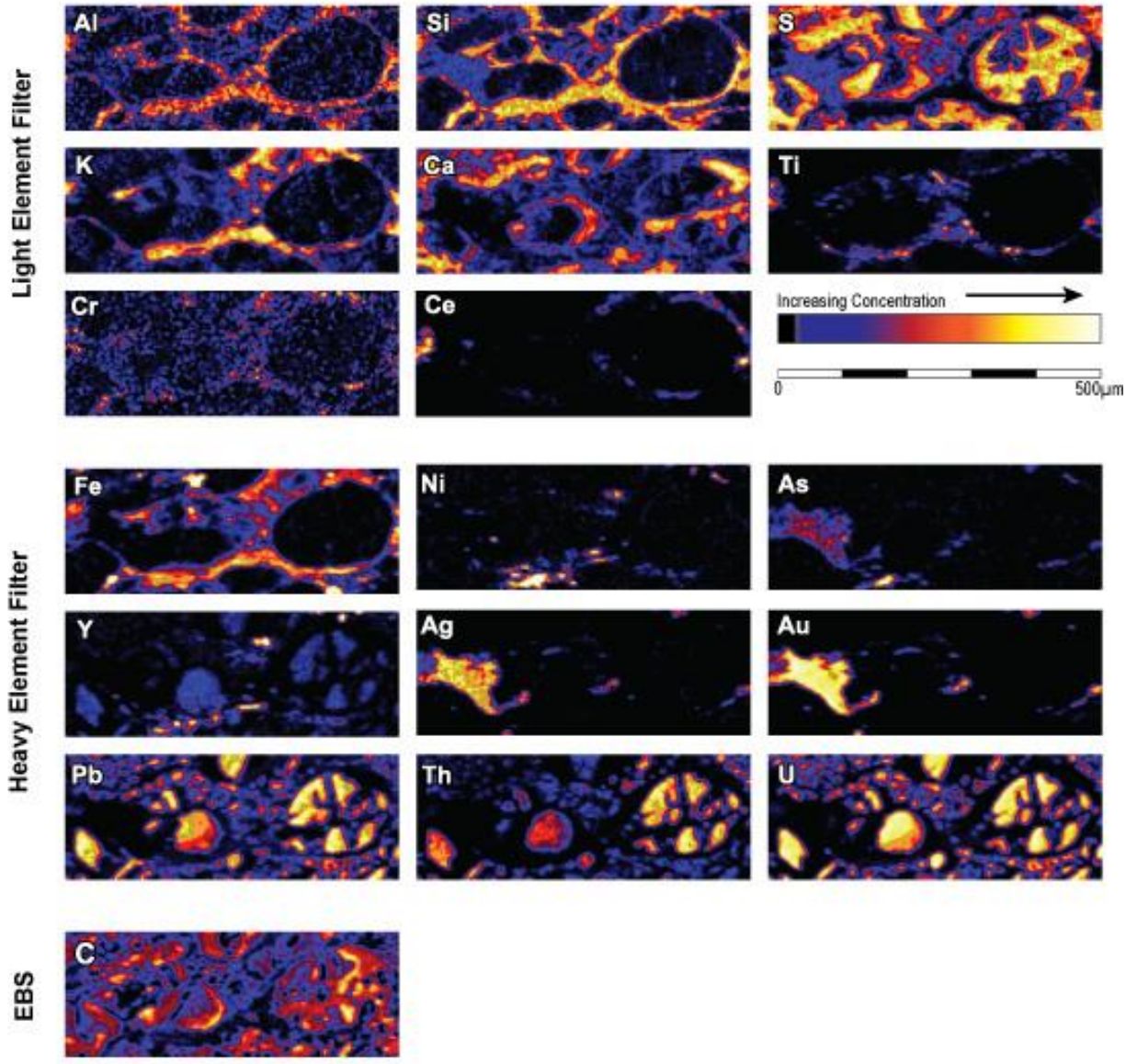

617

618 **Figure 5** PIXE micromaps of elements within CREEF01 sample, detected using GeoPIXE and the DA method.

619 Carbon map obtained using EBS method.

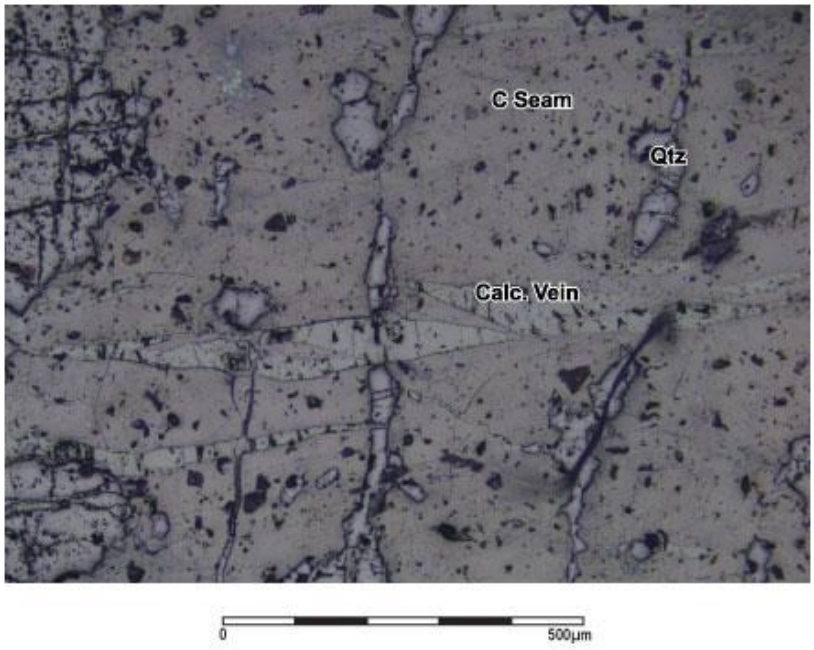

620

621 **Figure 6** Reflected light optical microscope image of the DFN10 sample from Doornfontein Gold Mine. The
622 sample is taken parallel to the elongated axis of the spindles in the carbon seam (C Seam) containing
623 quartz inclusions (Qtz) and cross-cutting calcite veins (Calc. Vein).

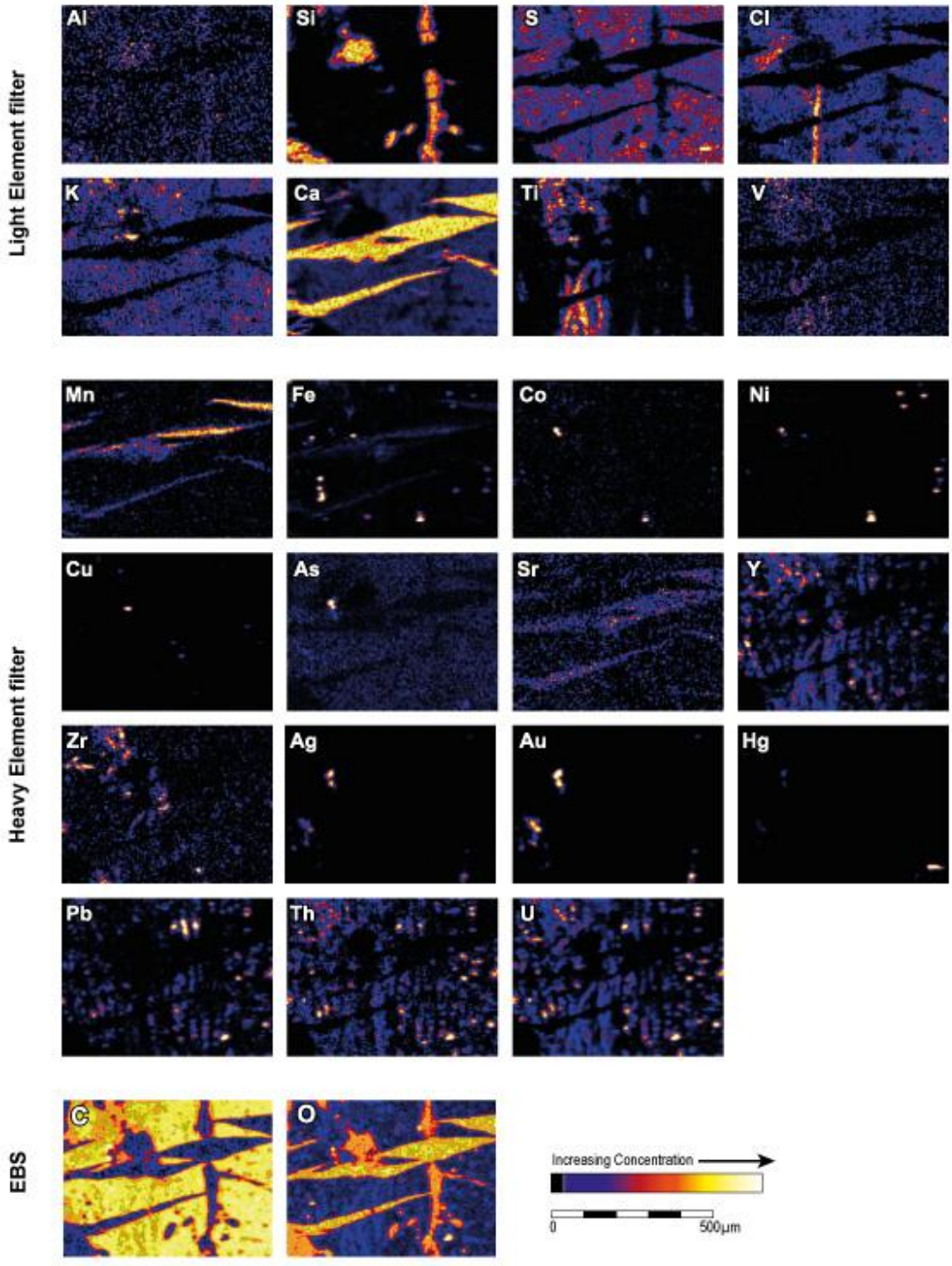

624

625 **Figure 7** PIXE micromaps of elements within the DFN10 sample, obtained using GeoPIXE and the DA

626 method. Carbon and oxygen maps obtained using EBS method.

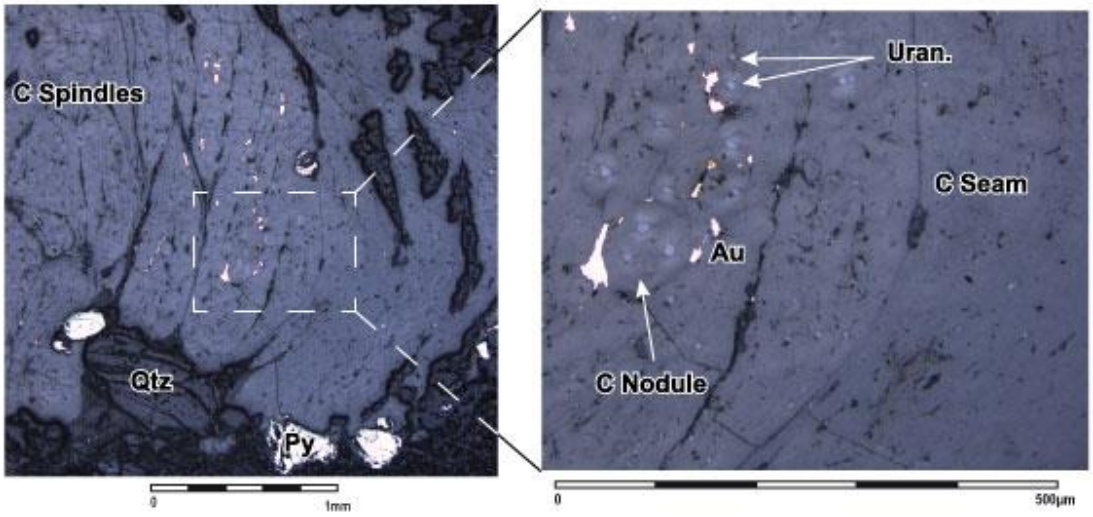

627

628 **Figure 8** Reflected light optical microscope image of the LGM3 sample from Lorraine Gold Mine. The
629 sample is taken parallel to the elongated axis of the carbon spindles (C Spindles) in the carbon seam (C
630 Seam) with quartz (Qtz) and pyrite (Py) at the base of the reef; a zoomed in view of one of the spindles
631 reveals rounded carbon nodule (C Nodule) surrounded by gold (Au) containing uraninite grains (Uran) all
632 of which are enveloped by the carbon spindle.

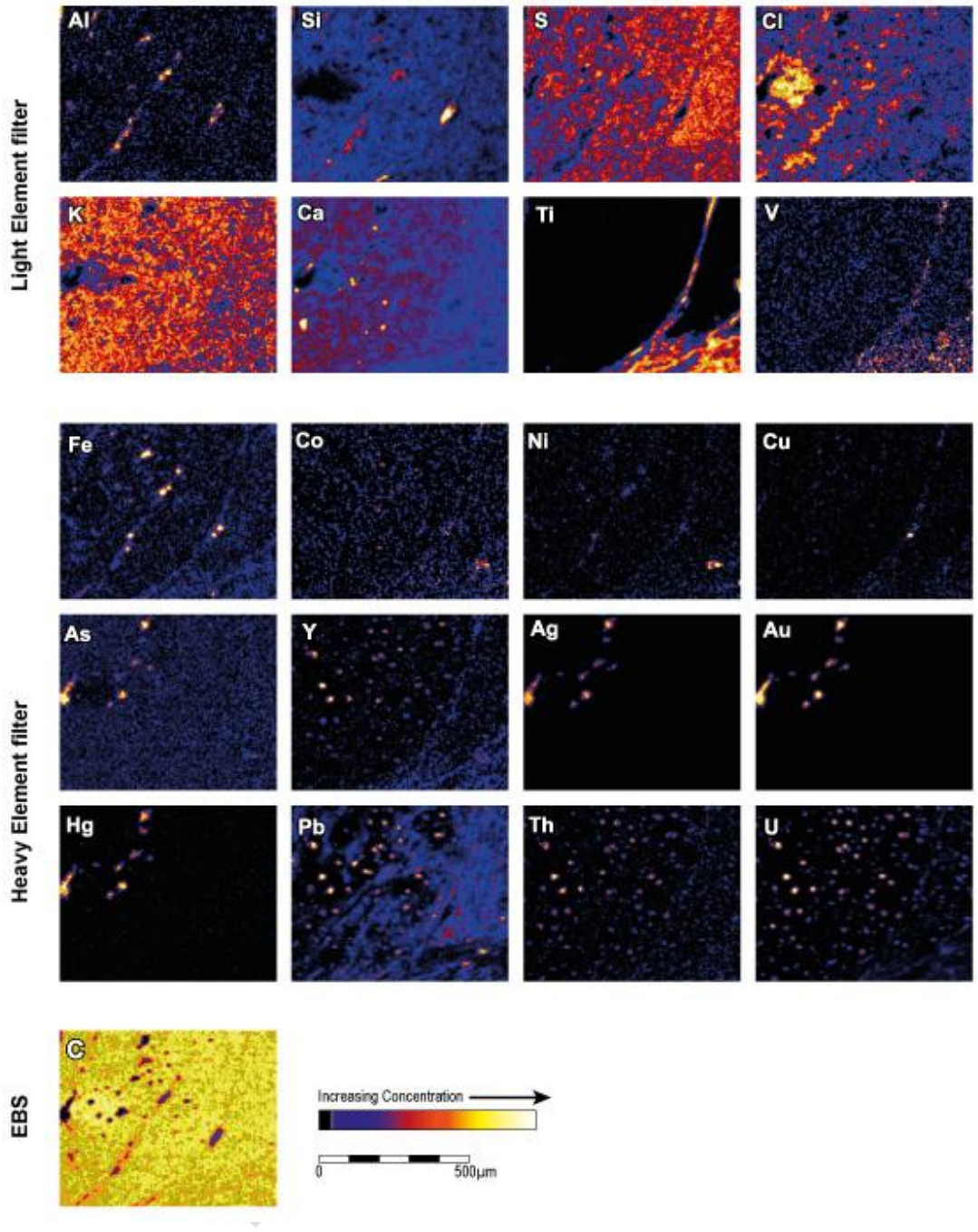

633

634 **Figure 9** PIXE micromaps of elements within the LGM3 sample obtained using GeoPIXE and the DA

635 method. Carbon map obtained using EBS method**.**

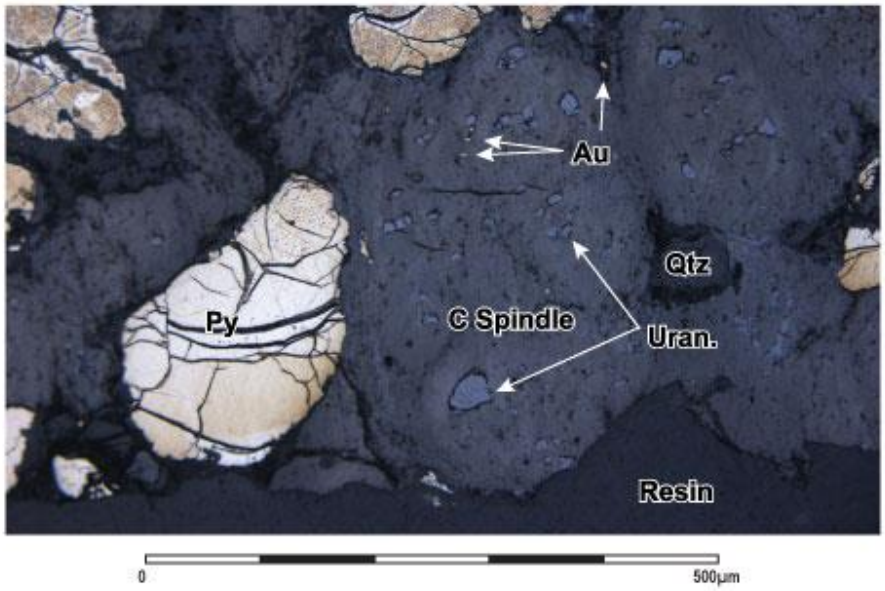

Figure 10 Reflected light optical microscope image of the MGS6512 sample from the Hartebeesfontein Gold Mine. The sample is taken perpendicular to the elongated axis of the carbon spindles (C Spindle) in the carbon seam. The bottom of the sample is encapsulated in resin from the sample preparation. The spindles contain abundant uraninite grains (Uran.), quartz inclusions (Qtz) and gold (Au). There are a number of large pyrite grains (Py) between the spindles.

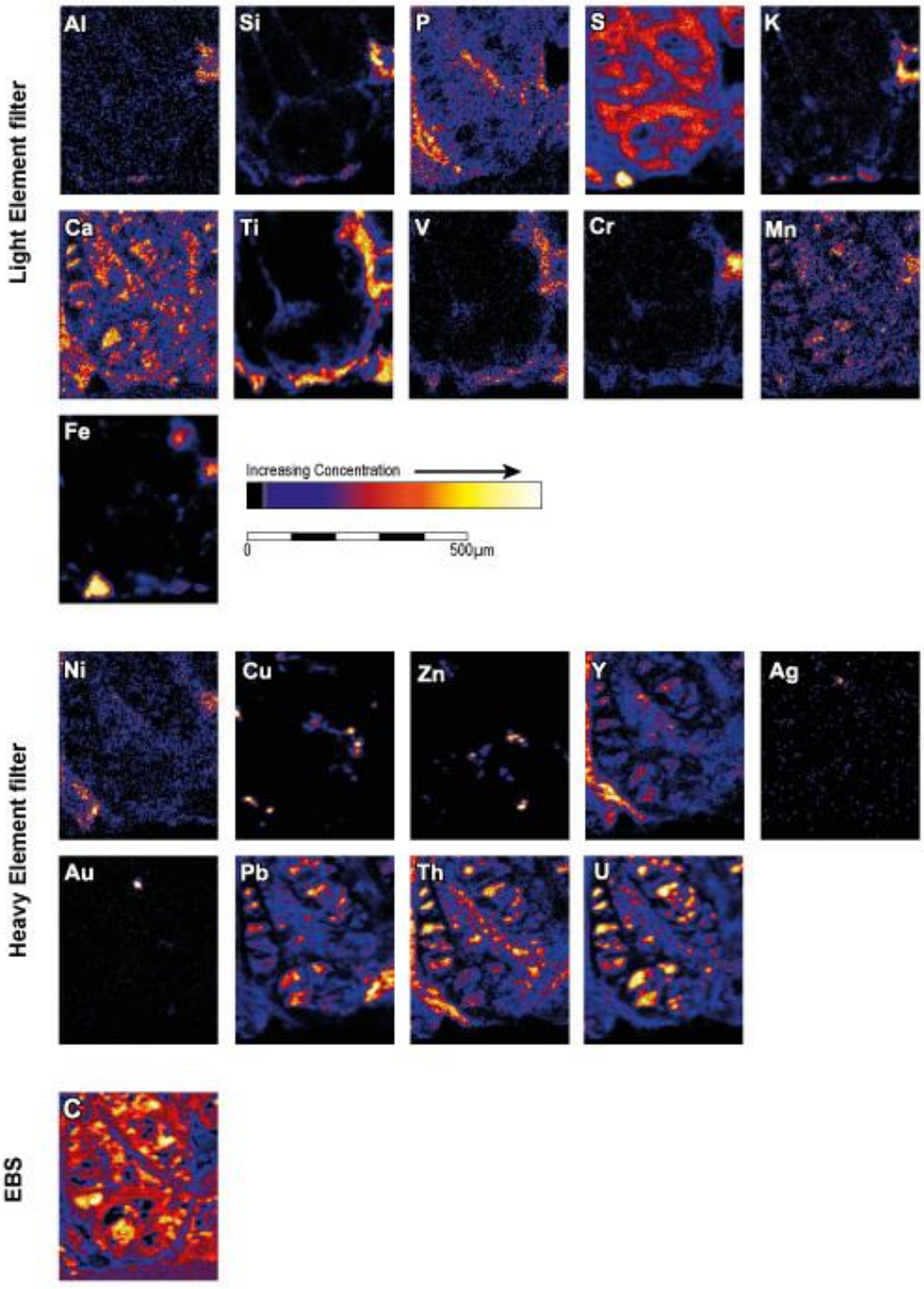
Light Element filter
Al
Si
P
S
K
Ca
Ti
V
Cr
Mn
Fe
Increasing Concentration
0
500µm
Heavy Element filter
Ni
Cu
Zn
Y
Ag
Au
Pb
Th
U
EBS
C

642

643 **Figure 11** PIXE micromaps of elements within the MGS6512 sample, obtained using GeoPIXE and the DA

644 method. Carbon map obtained using EBS method

645 **Table 1** Compositions of various hydrothermal fluids compared to modern day sea water

	Sea Water (Seward *et al.*, 2013)	Taupo Geothermal Fluid (Seward *et al.*, 2013)	Mississippi Oilfield Brines (Seward *et al.*, 2013)	Crude Oil (Shah and Filby, 1970)	Chinese Oil (Chifang *et al.*, 1991)
Temperature	2	275	107	-	-
pH	7.8	8.01	5.65	-	-
Na (ppm)	469	1154.697	76.25	-	298.4
K (ppm)	9.8	125.641	17.68	-	-
Ca (ppm)	10.2	0.227	774.34	-	-
Mg (ppm)	52.8	0.004	-	-	-
Mn (ppm)	-	-	1.16	-	6.532
Ni (ppm)	-	-	-	163.11	43.28
Fe(ppm)	-	-	6.19	44.78	64.06
Al (ppm)	-	-	-	-	8.84
Si (ppm)	0.2	19.238	0.71	-	-
Ba (ppb)	0.1	-	1056	-	9.74
Cu (ppm)	-	4.45	0.02	-	-
Cr (ppm)	-	-	-	0.0085	13.464
Co (ppm)	-	-	-	1.71	8.86
Ce (ppm)	-	-	-	-	0.114
Zn (ppm)	-	0.185	222	29.78	30.11
Pb (ppm)	-	0.023	53.2	-	-
Mo (ppm)	-	0.043	-	-	-
Sc (ppb)	-	-	-	1.67	32
V (ppm)	-	-	-	-	1.85
Sn(ppm)	-	0.84	-	-	-
Se (ppm)	-	-	-	0.53	33.24
Cd (ppm)	-	-	0.83	-	-
Ag (ppb)	-	6	-	-	-
Au (ppb)	-	16	-	1.35	-
As (ppb)	-	17	-	2625.6	14
Eu (ppb)	-	-	-	5.03	6
Hg (ppb)	-	-	-	3236.47	-
Hf (ppm)	-	-	-	-	0.038
La (ppm)	-	-	-	-	0.62
U (ppb)	-	-	-	59.57	-
Sb (ppb)	-	0.004	-	55.36	322
Th (ppm)	-	-	-	-	0.008
Cl (ppm)	551.6	613.923	5614.69	-	34
Br (ppm)	0.8	0.451	13.03	-	27.71
F (ppm)	0.1	0	0.04	-	-
B (ppm)	0.4	12.213	8.05	-	-
SO_4 (ppm)	22.4	410.375	0.19	-	-
H_2S (ppm)	-	-	-	-	-
S (ppm)	-	-	-	-	25400
HCO_3 (ppm)	2.9	48.261	-	-	-

646

647

648

649 **Table 2** Carbon bearing reef samples and their sample locality

Sample Number	Reef and Locality
DFN10	Carbon Leader Reef, from Doornfontein Mine, Carletonville
LGM3	Basal Reef, from Loraine Gold Mine, Welkom
CREEF1	"C" –Reef, from Blyvooruitzicht Mine, Carletonville
MGS6512	Vaal Reef, from Hartebeesfontein Gold Mine, Klerksdorp

650

The Anatomy of Gold: X-Ray Tomography of the Internal Structure of a Carbon Seam from the Witwatersrand Basin

Tremain H. E. Woods

School of Geosciences, Witwatersrand Basin Research Team, DST-NRF Centre of Excellence for Integrated Mineral and Energy Resource Analysis, Private Bag 3, WITS 2050, South Africa

Gillian R. Drennan

School of Geosciences, Witwatersrand Basin Research Initiative, DST-NRF Centre of Excellence for Integrated Mineral and Energy Resource Analysis, Private Bag 3, WITS 2050, South Africa

Gillian.drennan@wits.ac.za

Kristian J. Carlson

Evolutionary Studies Institute and School of Geosciences, University of the Witwatersrand, Private Bag 3, WITS 2050, South Africa

Igor Ž. Tonžetić

Indigo Research Laboratories, Unit W9, Ormonde View Estates, Nasrec Road, Johannesburg, 2190, South Africa

Abstract

TBC

Keywords: Gold, Auto-SEM-EDS, micro Computed-Tomography, Carbon

1. Introduction

The Witwatersrand Basin in South Africa is the largest, single source of gold ever found. Carbon and gold have an intimate association in seams found within the Witwatersrand Basin, but has the hypothesized origin of the carbon seams become convoluted? (Frimmel and Hennigh, 2015; Heinrich, 2015) The basin has produced many times more gold than the next largest deposit (McCarthy, 2009). Carbon may be implicated in the explanation for the wealthy endowment of gold found in the Basin because as much as 40% of the gold mined is associated with carbon (Mossman et al., 2008). Where most abundant, carbon forms seams with small particles of gold concentrated between the hydrocarbon spindles (Gray et al., 1998; Smieja-Król et al., 2009). This has led to greater focus on the carbonaceous products within the Witwatersrand gold-bearing reefs (Gray et al., 1998; Parnell, 1999; England et al., 2002). This paper examines the distribution of gold and associated minerals within a well-developed carbon seam in order to determine the processes that formed the carbon seams within the Witwatersrand Basin. The aim of this research it to determine whether carbon seam forms and gold distribution can be explained using epigenetic processes.

2. The Witwatersrand Basin – Geological Setting and the association of Carbon and Gold

The basin has a long and complex formation history and as a result of this mineralisation has been altered (Robb et al., 1997).The Witwatersrand Basin is a 7 km thick volcano-sedimentary sequence that spans 300 km by 100 km in central South Africa (Smith and Minter, 1980) and is famous for its sheer volume and wealth of gold, reaching peak production in the 1970's (Phillips, 2011). The Basin was formed between 3074 and 2714 Ma overlies the granite-greenstone belts of the Kaapvaal Craton (Robb et al., 1991; Koglin et al., 2010). Sedimentation of the Basin was terminated by the extrusion of the Ventersdorp lavas, which are in turn overlain by sediments of the Transvaal Supergroup (Van der Westhuizen et al., 1991). The entire sequence was then impacted by the Vredefort impact structure at 2020 Ma, which affected the structure and possibly mineralisation (Reimold and Gibson, 1996; Robb et

al., 1997). Therefore, Controversy still surrounds the Witwatersrand mineralisation to date, with the mechanisms that contributed to its metal endowment hotly debated. Historic and current theories pertaining to the genesis of the mineralisation can be categorised into three main models:

a. The placer model, originally guided by early field studies of Mellor and Banks (1916), viewed the mineralisation as detrital and therefore formed by fluvial processes. This was supported by evidence of rounded gold, uraninite and pyrite (all of which are high density models) that could have experienced strong sedimentary controls resulting in 'reef' mineralisation (Minter, 1976).
b. Post-sedimentation the Witwatersrand Basin underwent greenschist-facies metamorphism, some researchers propose that the mineralisation was instead due to prolific circulation of hydrothermal fluids precipitating gold and secondary pyrite (Phillips et al., 1987; Phillips and Law, 1994). This hydrothermal model is supported by evidence of the skeletal structure of gold and abundant alteration minerals occurring throughout the Basin (Phillips and Powell, 2011)
c. The model favoured currently satisfies components of the above – in essence a modified placer model (Robb et al., 1997; Robb and Robb, 1998; Drennan and Robb, 2006). In this model, gold, pyrite and uraninite were introduced by fluvial processes (accounting for the sedimentary component), and later remobilised as the Basin was metamorphosed and mineralisation, redistributing and upgrading the original mineralisation (accounting for the strong hydrothermal component).

Consequently, modern research on the Witwatersrand Basin attempts to satiate the question- why is gold mineralisation so strong in the Basin? Especially in the carbon seams where the highest gold grades occur predominantly. Much of the debate surrounding the seam carbon initially centred on their form. Carbon occurs as rounded nodular (or "fly-speck") froms less than 1 mm in diameter, and as seams up to 30 cm thick, with fibrous spindles interspersed within and gold between the spindles (Gray et al., 1998; Smieja-Król et al., 2009).The carbon seams are very uranium rich, initially rounded detrital grains are fragmented within the hydrocarbon spindles (Simpson and Bowles, 1977; Gray et al., 1998). Hallbauer (1975), found evidence documenting complex carbon structures that could be associated with primitive organisms. Hence, carbon seams were envisaged as mat-like structures of algae that trapped particulate gold in-situ (Hallbauer, 1975; Minter, 1991). However, more recent work suggested that is unlikely as

the seam structures contain complex phases of carbon and uraninite, as well as hydrothermal gold mineralisation (Spangenberg and Frimmel, 2001; Drennan and Robb, 2006).

Hydrothermal mechanisms have been investigated to explain the occurrence and form of carbon seams (England et al., 2002). The currently prevailing hydrothermal model is that fluids containing oils circulated after deposition in the Witwatersrand Basin (England et al., 2002). Where heavy minerals, such as uraninite, had been concentrated these fluids found sites to further enhance mineralisation (Schidlowski, 1981) as hydrocarbons radiolytically polymerised and/or precipitated via nanocarbon growth around originally detrital uraninite grains (Schidlowski, 1981; Woods et al., 2016a). This accounts for the high concentrations of fragmented uraninite within carbon seams (Pretorius, 1981). The fluids that remobilised the elements (Au, U, C, Fe, S) are well-constrained from fluid inclusion studies (Drennan et al., 1999; Spangenberg and Frimmel, 2001) and elemental micromaps (Fuchs et al., 2016; Woods et al., 2016b). However, the effect that remobilisation had on gold formation and distribution has not yet been assessed. Therefore, the distribution of gold associated with carbon seams in three dimensions is investigated in this study.

3. Methodology

3.1 Sample Preparation and Petrography

The sample selected for this study is an example of a well-developed carbon seam displaying clear carbon spindles from the Carbon Leader Reef (Carletonville Goldfield) which has anomalous amounts of gold between spindles. The sample comprises a 22 mm thick carbon seam, enclosed between a quartz-pebble conglomerate (footwall) and a quartzite (hanging wall) layer (Figure 1). Whilst the whole sample was utilised for non-destructive µCT analysis only a small portion of the sample (10 mm thick) was available for other analytic techniques which required preparation as a polished ore block.

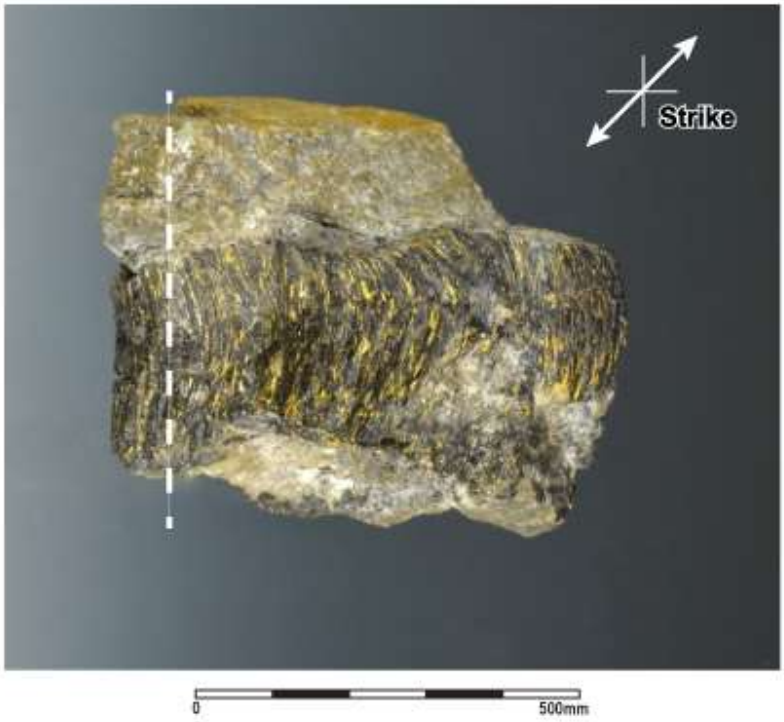

Figure 1. Photograph of CLR sample showing carbon seam bound by a conglomerate footwall and quartzite hanging wall. Photo is taken parallel to strike orthogonal to dip, the white dotted-line shows where the sample was cut

3.2 MicroCT (µCT)

High resolution µCT scans of Witwatersrand carbon seams are yet to be published. Even though µCT has successfully been applied in geological investigations of sulphide minerals in ultramafic rocks (Godel et al., 2006) and in gold grains in porphyry deposits (Kyle and Ketcham, 2003).

Computed tomography uses X-rays passing through a sample that is rotated through 360 degrees to visualize material differences. Materials within the sample attenuate X-rays to different extents such that dense materials attenuate more than less dense materials. Table 1 shows relative densities of a number of materials commonly seen in Witwatersrand Reefs. The notable difference is the specific gravity of hydrocarbons (<2) compared to gold (19.3), which creates sufficient material contrast in the image stack generated by µCT to permit digital separation of the two materials (i.e., segmentation) using VGStudio Max 2.2 (Volume Graphics GmbH).

Table 1: Relative densities of minerals commonly found in Witwatersrand carbon seams

Mineral	Relative Density Compared to Water (Cairncross, 2004)
Hydrocarbon	<2
Gold	19.3
Phyllosilicates	2.5 – 3.0
Quartz	2.66
Uraninite	7.5 – 10
Pyrite	5

A high resolution image stack (voxel size = 29 µm) of the CLR sample was generated using a Nikon Metrology XTH 225/320 LC dual source industrial µCT system. The sample was placed on a rotating pedestal, while the X-ray source is fixed. The system is located at the Paleosciences Centre of the University of the Witwatersrand. Scan parameters include: 210 kV, 100 µA, 2000 projections, and 3.6 µm of copper filtration.

Acquired image data were processed using VGStudio Max 2.2 (Volume Graphics, GmbH). Using thresholding, gold was filtered out of the image stack, which was subsequently compared to the petrographic images. A volume of interest representing the 3D distribution of the gold was orientated at various positions in order to examine the 3D form and distribution of the gold.

3.3 Auto-SEM-EDS

After non-destructive µCT analysis (outlined above) the CLR sample was then cut and mounted as a polished ore block in order to correlate the density data of the µCT scan with mineralogical data. The gold distribution from the 3D rendered µCT data was complimented using 2D mineral mapping Auto-SEM-EDS (scanning electron microscopy with energy dispersive x-ray spectroscopy) technology. For this the sample was coated in 100nm of carbon. A Carl Zeiss Mineralogic® system, comprising an Evo LS15 tungsten filament SEM platform, combined with multiple (in this instance 2) Bruker XFlash® 6|30 EDS detectors, was used throughout analysis. Scans were conducted at 25kV for maximum energy resolution of most elements (up to and including uranium) and a beam current of ~1.3 nA. X-Ray mapping was conducted at 8 µm beam stepping intervals across the polished surface. X-ray count rates were calibrated to 500,000 counts per second to a gold standard which was also used as an X-ray identification elemental standard (L-Alpha lines were used). The EDS data was combined into a false-

colour mineralogical map, that stitched together 28 fields to create the final map. The system processed and classified the data using the "Mineral Recipe" protocols of Mineralogic®. from the Mineralogic Explorer® program, following the protocols of Tonžetić (2015).

4. Results

4.1 Internal structure of the carbon seam

The polished ore block was examined for trends in gold distribution and evidence of secondary features (veinlets, micro-faulting and secondary minerals). **Error! Reference source not found.** illustrates the carbon seam between the conglomerate footwall and quartzite hanging wall. The undulating pebble surfaces form the base onto which carbonaceous material appears to have formed with smaller masses infilling spaces between the larger quartz clasts (**Error! Reference source not found.** (a)). The base of the carbon seam contains fragmented pyrite grains within micro-crystalline silicate minerals between rounded hydrocarbon masses (**Error! Reference source not found.** (a)). Gold is seen infilling fractures in pyrite grains as well as coating the base of carbon spindles in contact with the clasts. Where the spindles extend upwards from the base, gold is seen infilling the tapered spaces between adjacent spindles (**Error! Reference source not found.** (b)). In addition to the gold between the hydrocarbons there is gold within an unidentified fine-grained silicate material (**Error! Reference source not found.** (b)). Gold throughout the carbon seam in this section is most concentrated at the base of the spindles (**Error! Reference source not found.**). Closer to the quartzite hanging wall the gold occurs as filaments between the hydrocarbon spindles gold as well as smaller particulate particles (**Error! Reference source not found.** (d)). Gold throughout the sample follows the form of the surrounding hydrocarbon or pyrite phases, with little or no visible rounded detrital gold (**Error! Reference source not found.** (b) & (d)). Within the carbon seam, there is a sub rounded and fractured quartz clast (**Error! Reference source not found.** (c)). The clast has an enrichment of gold at the contact between itself and the rounded porous pyrite and the enclosing hydrocarbon. The spindles of the carbon seam are elongated in two different directions around the quartz clast (**Error! Reference source not found.** (b) standard spindles are continuous; curved spindles below clast spindles are bent towards the clast). This is in contrast to carbon spindles above, which are quite uniform and occur perpendicular to the bounding surface of the hanging wall (**Error! Reference source not found.** (d)). Carbon spindles are also seen forming between adjacent pyrite and quartz clasts. In these cases, the width of the spindle is reduced between clasts and then extending back to the same bounds on either side of the clatsts. A small quartz vein occurs ross-cutting the carbon seam (**Error! Reference source not found.** (b) & (d)). The quartz vein contains micro-

crystalline pyrite and is fractured parallel to strike. These fractures are infilled with fine grained silicate materials.

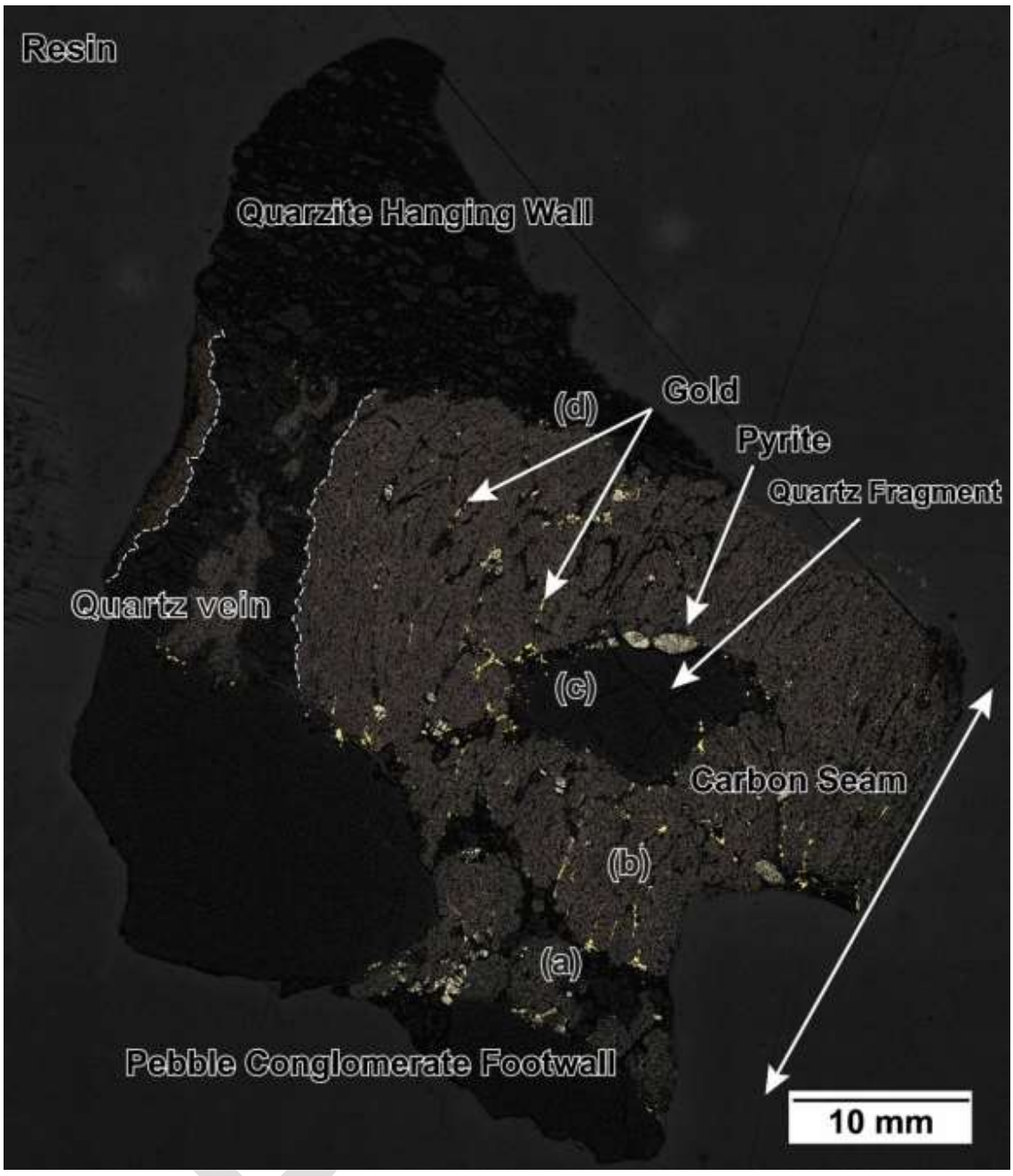

Figure 2 Stitched petrographic image of CLR ore block. The carbon seam is bounded by a quartzite hanging wall and a conglomeratic footwall. The sample is mounted in resin. The quartz vein cutting the sample is highlighted as well as the positions of the enlarged views for Figure 3 (a) – (d).

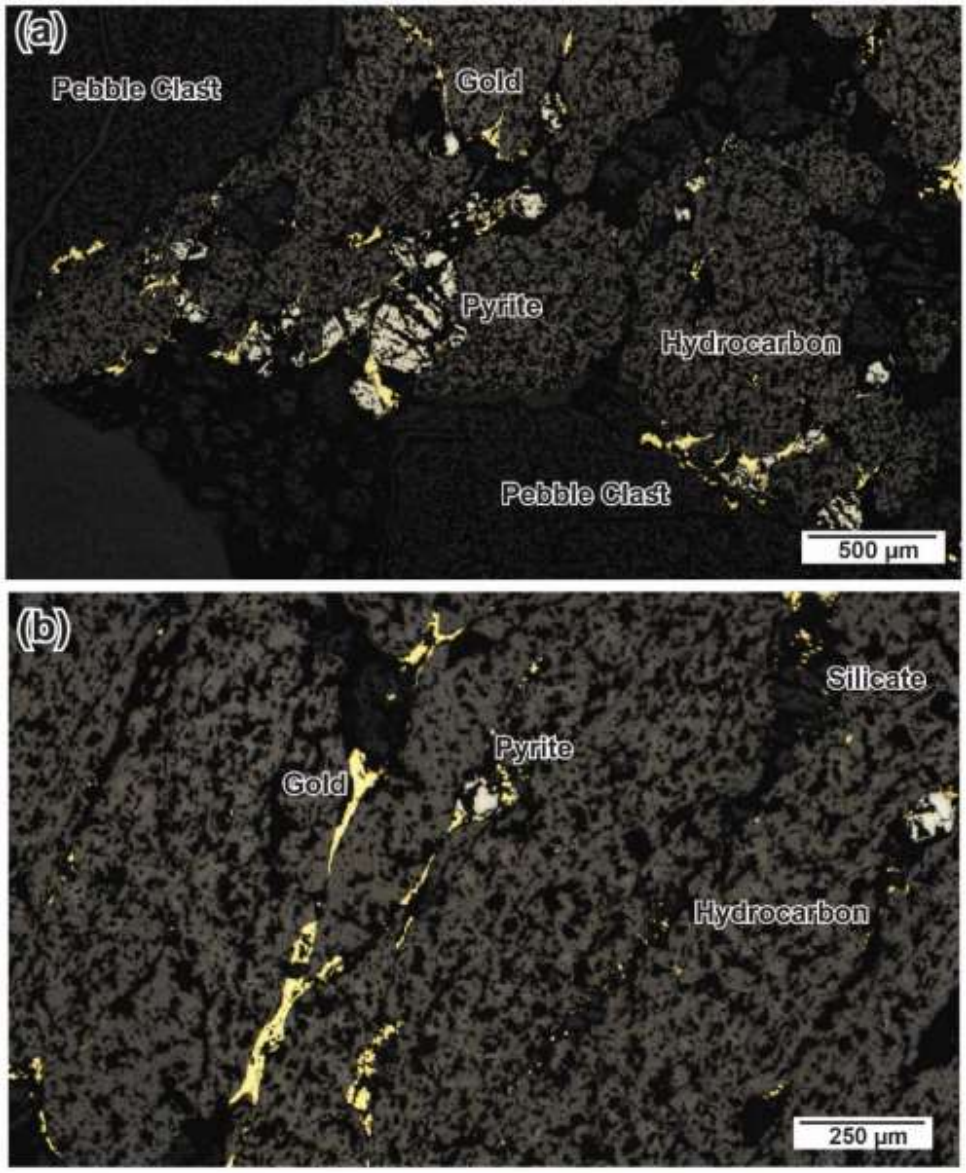

Figure 3 Enlarged reflected light images of CLR sample features (a) Base of the carbon seam spindles, showing fractured pyrite and gold at pebble conglomerate contact; (b) lower carbon seam spindles with gold and silicate materials between spindles;

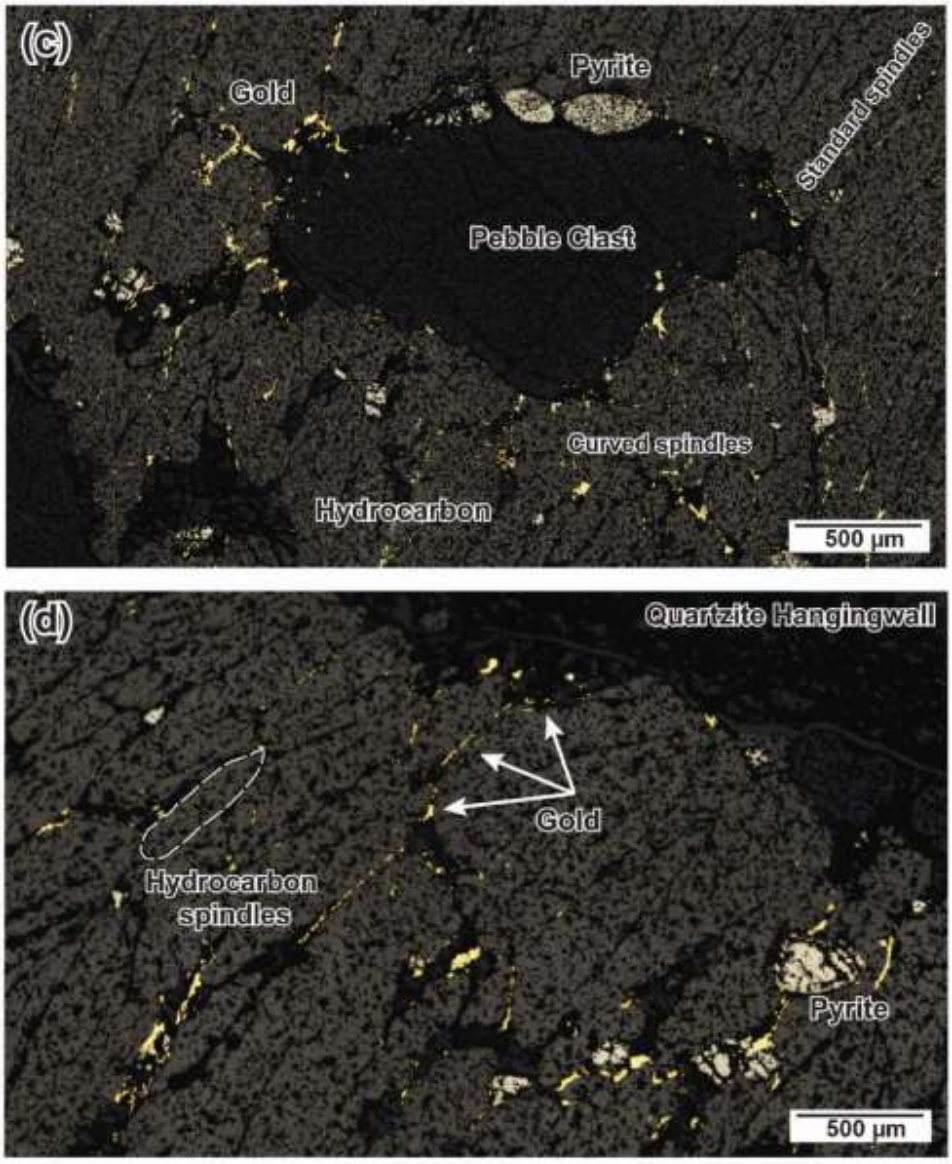

Figure 4 continued Enlarged reflected light images of CLR sample features (c) quartz pebble clast in the middle of the carbon seam and (d) upper carbon seam, with a single spindle highlighted and lesser gold at contact with the hanging wall.

A quartz vein cross-cuts the carbon seam, displacing hydrocarbon masses on either side (**Error! Reference source not found.**). The sample contains a number of very small (30-50µm) uraninite grains (Figure 6.3 (b)). Some of the larger grains of uraninite (50 -120 µm) appear fragmented into a mosaic of smaller grains separated by hydrocarbon. In summary, most of the gold, silicates and pyrite within the sample occur between spindles of the carbon seam whereas uraninite is seen contained within the spindles.

4.2 Minerals associated with gold in between the carbon spindles

BSE images of the various mapped portions of the CLR sample (**Error! Reference source not found.**) reveal features that are not clear in petrographic images. The carbon seam has abundant, and fairly evenly distributed, uraninite within the spindles (**Error! Reference source not found.**).

Figure 5 SEM BSE image overlaid over stitched optical microphotograph showing areas mapped by EDS. The BSE overlays highlight materials between the spindles and enhance visibility of uraninite grains, gold and silicate materials, (a) &(b) indicate the positions of Figure 6 (a) & (b) respectively.

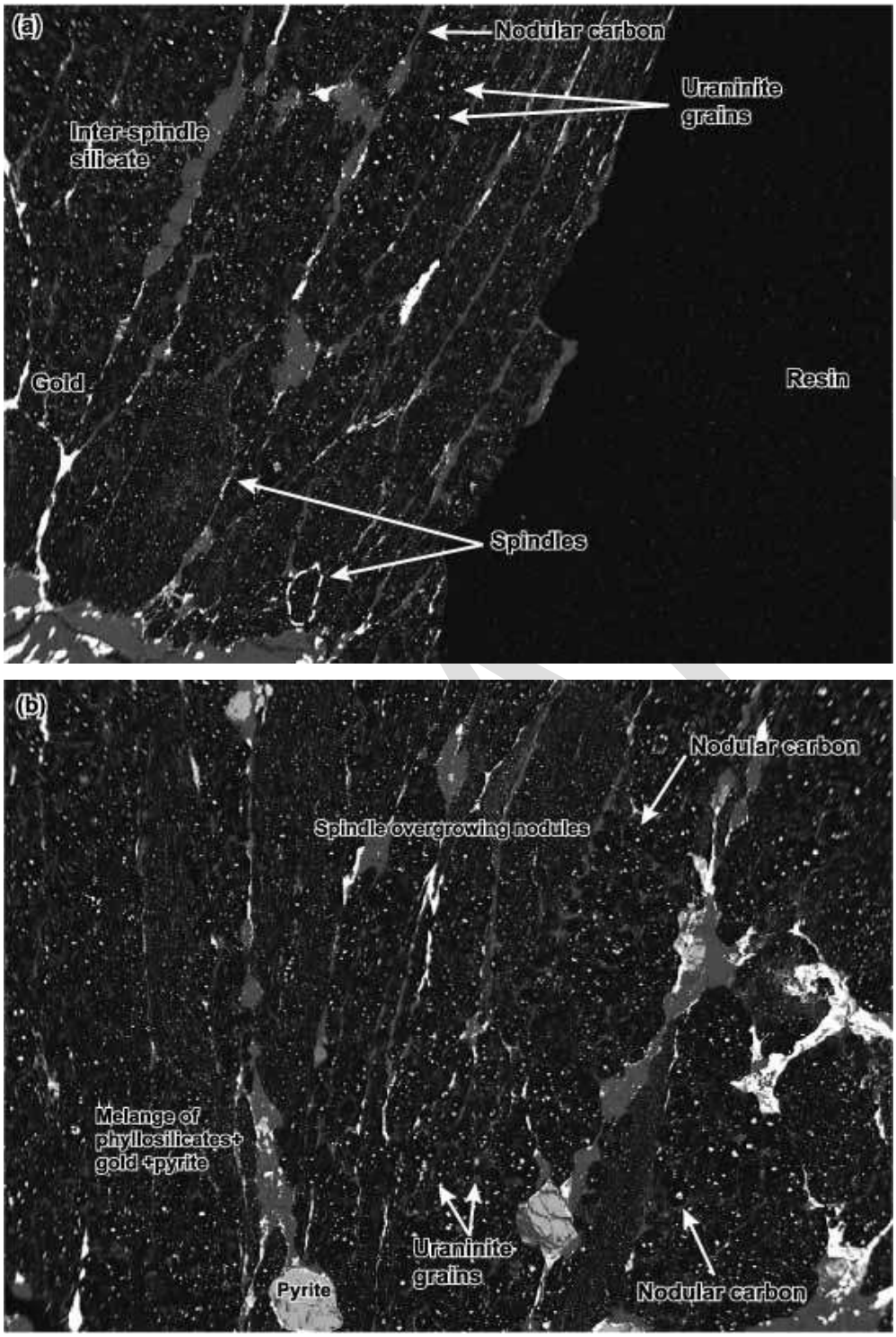

Figure 6 BSE image of seam portion of CLR sample Images show the uraninite grains that are more easily distinguishable than optical petrography. ***(a)*** *The dark material is the hydrocarbon which forms spindles, outlined by the gold and silicate materials between them. One of the spindles is outlined to demonstrate this. (b) Small rounded carbon nodules overgrown by a larger spindle, also highlighted is the melange of phyllosilicates, gold and pyrite between the spindles.*

The shape of the spindles is easier to distinguish in the BSE images (**Error! Reference source not found.**). At the base of the carbon seam, the spindles are more bulbous having rounded bases that taper upwards through the seam. In the middle of the carbon seam, spindles are more uniform in width, tapering towards the ends which are also rounded. The top of the carbon seam also contains bulbous, tapered spindles, although these are inverted with respect to those at the base of the seam (wide rounded top, pointed tapered base).

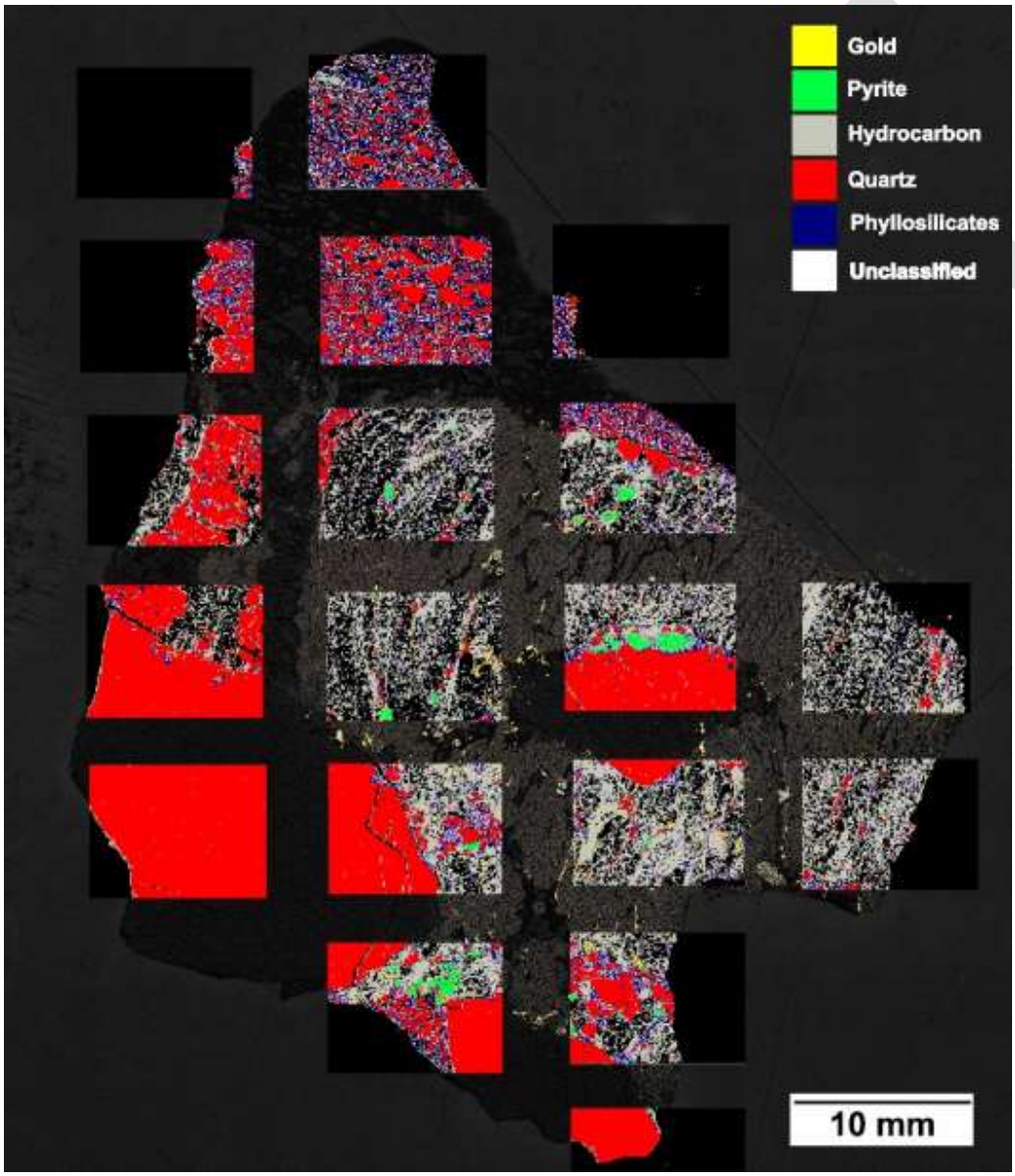

Figure 7 Mineral classification of CLR sample as per Auto-SEM-EDS. Image shows false colour composite map of minerals as identified by Auto-SEM-EDS. The abundance of phyllosilicates and pyrite is outlined especially well by these images.

The images also reveal the presence of numerous smaller, rounded nodular carbons within the carbon spindles (**Error! Reference source not found.** (b)). Multiple nodules are seen overgrown by a larger spindle (**Error! Reference source not found.** (b)). It is clear from the BSE images that the minerals between the spindles occur as separate phases with distinct boundaries (**Error! Reference source not found.** (a) & (b)).

The EDS mineral maps show that the inter-spindle fine-grained minerals are comprised of varying amounts of phyllosilicates, quartz, gold and pyrite (**Error! Reference source not found.**). Phyllosilicates predominantly include kaolinite, pyrophyllite, muscovite, illite, chlorite, chloritoid, and talc (see EDS quantified mineralogy in supplementary materials, APPENDIX H) ranging from ~65 to 150 µm. Pyrite grains (particularly rounded porous pyrite) contain small amounts of gold. Hydrocarbons are also detected in the hanging wall as small rounded nodules (**Error! Reference source not found.**). The hanging wall contains the largest concentrations of phyllosilicate materials within a fine-grained matrix between the rounded quartzite grains.

4.3 Gold distribution in Three Dimensions

A threshold was applied to the µCT 3D rendered data to display only the gold (based on a density contrast) in any selected area within the sample (**Error! Reference source not found.**). The render was able to differentiate between gold and other materials, but the other materials could not be further differentiated from each other (e.g. pyrite from phyllosilicates). This region of interest was compared against the background of hydrocarbon and silicate materials in order to visualize and assess organizational characteristics in three-dimensional distributions (**Error! Reference source not found.**).

The 3D rendered µCT data (**Error! Reference source not found.**) highlights a greater abundance of gold than first detected by traditional 2D petrographic methods. This is likely due to the limited 'slice' view that such 2D methods allow which may not highlight the full extent of mineralisation in all directions (e.g. parallel or perpendicular to the plane of view during SEM investigations). The 3D rendered µCT data (**Error! Reference source not found.**) reveals that gold present in the pyrite grains was underestimated and this was taken into account when determining the rendered gold values of the sample (so as not to overestimate the volume of gold in the hydrocarbon). In both optical petrography and the BSE images gold was seen as inclusions in fractures in the pyrite grains.

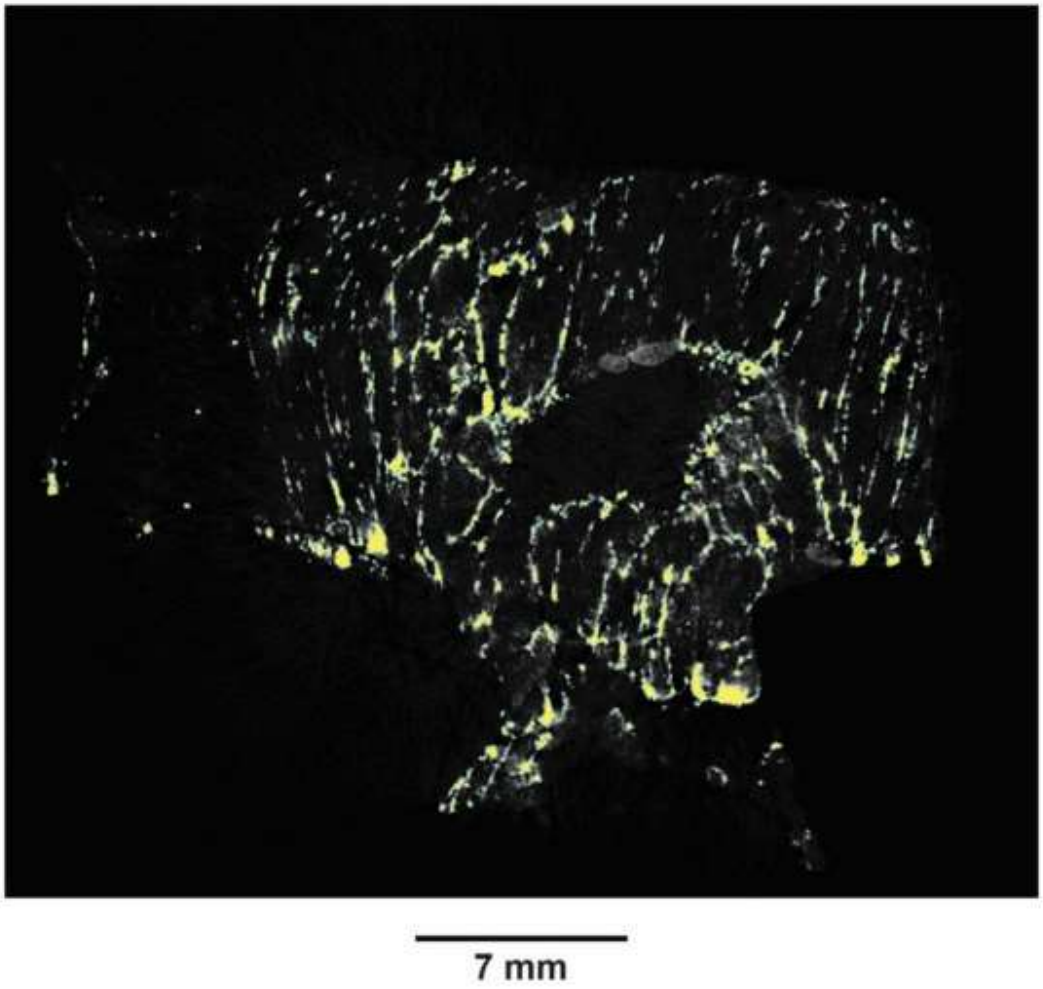

Figure 8 Gold regions of interest from µCT data threshold. The yellow areas with blue outlines (representing boundaries) encompass the gold. This image was compared to petrography to determine the accuracy of the fit.

Slices of µCT scan data (rendered perpendicular to strike of the carbon seam) accentuate changes in the lateral distribution of gold between the lower and upper portions of the seam from the footwall to the hanging wall (Figure 4.9. (a) – (f)). The base of the carbon seam has the highest concentrations of gold, occurring as grains and coatings to the spindles. The grains are concentrated in the interstices at the base of the carbon spindles. Slices through the centre of the carbon seam (Figure 4.9 (e) & (f)) reveal

that gold concentrates as filimants only in the space between spindles (as was seen in the vertical slices, see supplementary materials) and not as particulate gold.

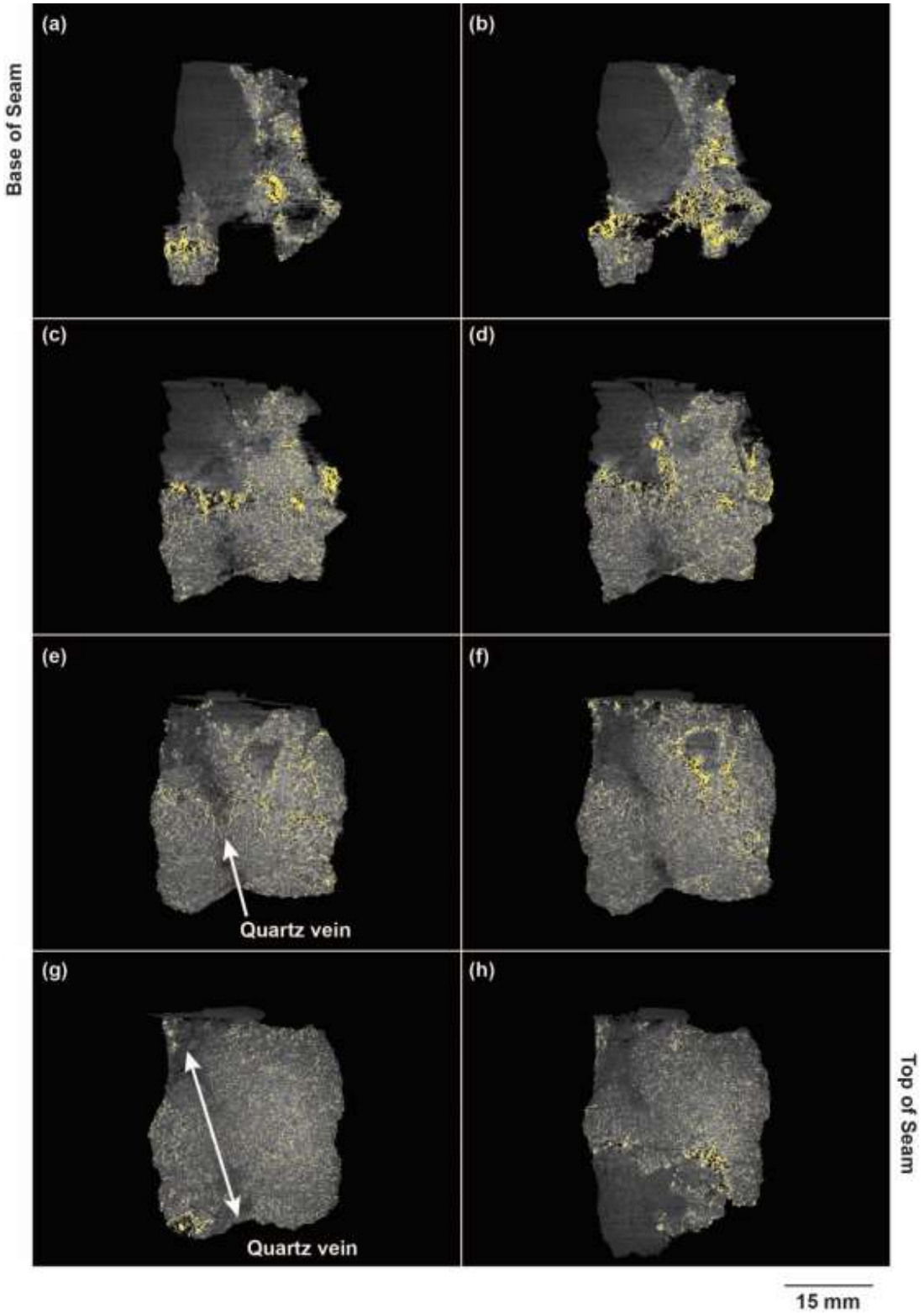

Figure 4.9. µCT render through CLR sample. The slices are taken from the base of the seam (a) moving up towards the quartzite hanging wall (h).

Beneath the displaced quartz clast, gold is also strongly concentrated in the spaces between the carbon spindles (**Error! Reference source not found.** & Figure 4.9 (f)). Gold occurs at the top of the carbon seam (hanging wall contact) but is less concentrated than at the footwall contact (i.e., fewer gold globules are noted in the μCT data (Figure 4.9 (b) vs. Figure 4.9 (h)). The views in Figure 6.8 also show the extent of the cross-cutting quartz vein (Figure 4.9 (e), (f) & (g)). The vein cuts through the seam displacing masses of carbon and gold. Highest gold concentrations are seen at the base of the carbon seam within the carbonaceous material (Figure 4.9 (a) & (b)).

5. Discussion

5.1 Spindles and Mineralisation

The abundant fragmented uraninite grains throughout the carbon spindles are thought to be a substrate onto which the hydrocarbons precipitate (Woods, Drennan & Durbach 2016; England et al. 2002; Schidlowski 1981). The precipitation of hydrocarbon onto uranium has been shown to be the result of catalytic precipitation possibly with a component of radiolytic polymerisation (Woods, Drennan & Durbach 2016). Thus, we suggest that the uraninite present in carbonaceous seam is of a detrital origin, but crucial to the formation of carbon seams and the enhancing of gold values.

The consistent occurrence of gold and phyllosilicates in the spaces between carbon spindles indicates an association between these minerals (**Error! Reference source not found.**). Phyllosilicate minerals elsewhere in the Witwatersrand Basin have been described as secondary mineral phases (Phillips & Law 1994; Phillips 1987). Within the CLR sample, phyllosilicates occur as microcrystalline masses which include kaolinite, pyrophyllite, muscovite, illite, chlorite, chloritoid, and talc. Consequently the occurrences of phyllosilicates in the CLR sample are consistent with the minerals characterised as metamorphic minerals by Phillips (1987). Small inclusions of phyllosilicates and gold occur within the carbon spindles themselves (as shown by **Error! Reference source not found.** & **Error! Reference source not found.**) but are predominantly found between spindles.

This supports the hypothesis of a multiple fluid component model recorded in the carbon seams and proposed by Woods *et al*. (2016b). Similar findings were reported by Drennan & Robb (2006) for the Beisa Reef and for carbon nodules found in quartz veins within the basin. This also suggests that the co-existing inter-spindle phyllosilicate and gold occurrences precipitated from the liquid remaining after the initial precipitation of spindles. This would explain the occurrence of finely disseminated gold and

phyllosilicates within the spindles as well as microcrystalline gold and phyllosilicates between the spindles.

Additional evidence for a multiple fluid component mineralisation mechanism can be seen from the BSE images of the phyllosilicate minerals between the spindles i.e., the phyllosilicates, gold and other micro-crystalline minerals form a “melange” between spindles. The rounded pyrite grains and some quartz inclusions within the carbon seams that cause spindles to contort around them, provide evidence that these grains were present before the formation of the carbon seam

The contortion of the seam carbon, along with literary evidence for detrital mineralisation and remobilising fluid processes, led to the following hypothesis for carbon seam formation. It is suggested that initially gold, uranium and pyrite were deposited by fluvial processes followed by remobilisation of mineralisation by multiple fluids (including hydrocarbon-rich fluids), which later precipitated in the presence of concentrations of uraninite. This precipitation resulted in mineralised spindle growth. Precipitation of the mineralised hydrocarbon spindles caused supergene enrichment the remaining fluid with silicates, phylosilicates, and whatever gold still remained in solution being enriched relative to the fluid that precipitated the hydrocarbon. This accounts for the presence of micro-crystalline quartz, phyllosilicates and gold in the inter-spindle interstices.

5.2 3D Gold Distribution

This investigation presents the first published µCT scans of a carbon seam from the Witwatersrand Basin and allows the authors effectively display the 3D distribution of gold throughout this exceptional CLR sample. The most striking evidence supporting the epigenetic formation of hydrocarbons in the carbon seams is provided by the µCT render (**Error! Reference source not found.** & Figure 4.9). The presence of the quartz clast displaced within the CLR sample shows evidence of hydrocarbon precipitation after deposition. The clast appears to represent a fragment of a larger rounded pebble from the conglomerate below. This could be due to the greater porosity of the underlying conglomerate that allowed for fluid movement within the conglomerate. Evidence for fluid movement has been previously provided by Parnell (1999) and Jolley *et al*. (2004) where fluids appear to have moved parallel to bedding, as well as in thrust faults and in veins. Hydrocarbon precipitation along a pre-existing fracture in the quartz clast resulted in the displacement of the clast fragment. The accumulation of recrystallized

gold in the hydrocarbon surrounding the fragment provides evidence of fluid migration along the pebble layer.

The µCT render shows that gold is most concentrated at the base of the carbon seam along pebble conglomerate contact of the footwall. From footwall to hanging wall, the gold concentration decreases as the spindles develop before being concentrated again at the hanging wall contact (although the concentration of gold in the hanging wall contact is still markedly less than that of the footwall contact; Figure 4.9).

The spindles in the carbon seam are bulbous at the hanging wall and footwall contacts, and taper towards the centre of the carbon seam. The forms of the carbon spindles, with maximum growth perpendicular to the bounding surfaces, are similar to crystals growth in quartz veins and pegmatites. Crystallisation in quartz veins and pegmatites is perpendicular to σ^1, the principle stress direction (Davis et al. 2012). In quartz veins crystals grow inwards from the bounding surfaces towards the centre. This provides a potential mechanism for the growth of the carbon spindles. Growth of the spindles commenced with globular masses of carbon and maximum gold precipitation adjacent to the bounding surfaces, becoming more elongated with lesser gold towards the centre of the carbon seam. The evidence presented in this research satisfies many of the issues concerning carbon seam formation in the Witwatersrand Basin and the distribution of gold within the seams.

However, here it is also apparent from the gold distribution that fluids moved from both the hanging wall and footwall in towards the reef contacts. This would explain the inverted spindle structures at the top of the seam. Additionally, it explains the tapering spindles, since with fewer fluids being available under pressure, slimmer spindles are precipitated.

6. Conclusion

Tomographic images and EDS mineral maps of an exceptional carbon seam sample from the Witwatersrand Basin revealed the distribution of gold mineralisation. Gold occurs with secondary phyllosilicate materials in the spaces between the spindles. Results indicate that gold concentration decreased towards the centre of the seam. This was likely due to the decrease in available gold-rich fluids as solid hydrocarbon was precipitated. Gold highlights the spindle shapes, and the 3D form of the spindles indicates growth from two directions, likely due to lower pressure in the reef portion. The

shape of the spindles indicates that growth of carbon spindles must have occurred simultaneously from the hanging wall downwards and from the foot wall upwards.

Acknowledgements

Carl Zeiss (Randburg) for use of the Mineralogic® Auto-SEM-EDS system.

References

Agangi, A., Hofmann, A., and Wohlgemuth-Ueberwasser, C.C., 2013, Pyrite zoning as a record of mineralization in the ventersdorp contact reef, Witwatersrand Basin, South Africa: Economic Geology, v. 108, no. 6, p. 1243–1272, doi: 10.2113/econgeo.108.6.1243.

Cairncross, B., 2004, Field Guide to Rocks & Minerals of Southern Africa: International Pub Marketing.

Drennan, G.R., Boiron, M.C., Cathelineau, M., and Robb, L.J., 1999, Mineralogy and Petrology Characteristics of post-depositional fluids in the Witwatersrand Basin: , p. 83–109.

Drennan, G.R., and Robb, L.J., 2006, The nature of hydrocarbons and related fluids in the Witwatersrand Basin, South Africa: Their role in metal redistribution: Processes on the Early Earth, Special Papers 405, v. 2405, no. 18, p. 353–386, doi: Doi 10.1130/2006.2405(18).

England, G.L., Rasmussen, B., Krapez, B., and Groves, D.I., 2002, Archaean oil migration in the Witwatersrand Basin of South Africa: Journal of the Geological Society, v. 159, no. 2, p. 189–201, doi: 10.1144/0016-764900-197.

Frimmel, H.E., and Hennigh, Q., 2015, First whiffs of atmospheric oxygen triggered onset of crustal gold cycle: Mineralium Deposita, v. 50, no. 1, p. 5–23, doi: 10.1007/s00126-014-0574-8.

Fuchs, S., Williams-Jones, A.E., Jackson, S.E., and Przybylowicz, W.J., 2016, Metal distribution in pyrobitumen of the Carbon Leader Reef, Witwatersrand Supergroup, South Africa: Evidence for liquid hydrocarbon ore fluids: Chemical Geology, v. 426, p. 45–59, doi: 10.1016/j.chemgeo.2016.02.001.

Gray, G.J., Lawrence, S.R., Kenyon, K., and Cornford, C., 1998, Nature and origin of “carbon” in the Archaean Witwatersrand Basin, South Africa: Journal of the Geological Society, v. 155, no. 1, p. 39–

59, doi: 10.1144/gsjgs.155.1.0039.

Hallbauer, D.K., 1975, The plant origin of the Witwatersrand carbon: Miner. Sci. Eng,.

Jolley, S.J., Freeman, S.R., Barnicoat, A.C., Phillips, G.N., Knipe, R.J., Pather, A., Fox, N.P.C., Strydom, D., Birch, M.T.G., Henderson, I.H.C., and Rowland, T.W., 2004, Structural controls on Witwatersrand gold mineralisation: Journal of Structural Geology, v. 26, no. 6-7, p. 1067–1086, doi: 10.1016/j.jsg.2003.11.011.

Koglin, N., Zeh, A., Frimmel, H.E., and Gerdes, A., 2010, New constraints on the auriferous Witwatersrand sediment provenance from combined detrital zircon U-Pb and Lu-Hf isotope data for the Eldorado Reef (Central Rand Group, South Africa): Precambrian Research, v. 183, no. 4, p. 817–824, doi: 10.1016/j.precamres.2010.09.009.

McCarthy, T.S., 2009, The Witwatersrand Supergroup, *in* Johnson, M.R., Anhaeusser, C.R., and Thomas, R.J. eds., The Geology of South Africa, The Geological Society of South Africa, Johannesburg, South Africa, p. 619.

Mellor, E.T., and Banks, E.H., 1916, Geological Map of the Witwatersrand Gold Field: Department of Mines and Industries, Geological Survey.

Minter, W.E.L., 1991, A review of the spatial arrangement of carbon in ancient placer sediments and its relationship to associated heavy minerals, *in* Carbon in Witwatersrand Reefs Symposium, Geol. Soc. South Africa, p. 37–38.

Minter, W.E.L., 1976, Detrital gold, uranium, and pyrite concentrations related to sedimentology in the Precambrian Vaal Reef placer, Witwatersrand, South Africa: Economic Geology, v. 71, no. 1, p. 157–176, doi: 10.2113/gsecongeo.71.1.157.

Mossman, D.J., Minter, W.E.L., Dutkiewicz, A., Hallbauer, D.K., George, S.C., Hennigh, Q., Reimer, T.O., and Horscroft, F.D., 2008, The indigenous origin of Witwatersrand “carbon”: Precambrian Research, v. 164, no. 3-4, p. 173–186, doi: 10.1016/j.precamres.2008.04.008.

Parnell, J., 1999, Petrographic evidence for emplacement of carbon into Witwatersrand conglomerates under high fluid pressure: Journal of Sedimentary Research, v. 69, no. 1, p. 164–170, doi: 10.2110/jsr.69.164.

Phillips, G.N., 2011, Gold exploration success: Applied Earth Science : IMM Transactions section B, v.

120, no. 1, p. 7–20, doi: 10.1179/1743275811Y.0000000019.

Phillips, G.N., 1987, Metamorphism of the Witwatersrand Gold Fields - Conditions during Peak Metamorphism: Journal of Metamorphic Geology, v. 5, no. 1980, p. 307–322 ST – Metamorphism of the Witwatersrand Go.

Phillips, G.N., and Law, J.D.M., 1994, Metamorphism of the Witwatersrand gold fields: A review: Ore Geology Reviews, v. 9, no. 1, p. 1–31, doi: 10.1016/0169-1368(94)90017-5.

Phillips, G.N., Myers, R.E., and Palmer, J.A., 1987, Problems with the placer model for Witwatersrand gold.: Geology, v. 15, no. 11, p. 1027–1030, doi: 10.1130/0091-7613(1987)15<1027:PWTPMF>2.0.CO;2.

Phillips, G.N., and Powell, R., 2011, Origin of Witwatersrand gold: a metamorphic devolatilisation–hydrothermal replacement model: Applied Earth Science, v. 120, no. 3, p. 112–129, doi: 10.1179/1743275812Y.0000000005.

Pretorius, D.A., 1981, Gold and Uranium in Quartz-Pebble Conglomerates: Economic Geology, v. 75th Anniv, p. 117 – 138.

Robb, L.J., Charlesworth, E.G., Drennan, G.R., Gibson, R.L., and Tongu, E.L., 1997, Tectono-metamorphic setting and paragenetic sequence of Au-U mineralisation in the Archaean Witwatersrand Basin, South Africa: Australian Journal of Earth Sciences, v. 44, no. 3, p. 353–371, doi: 10.1080/08120099708728317.

Robb, L.J., Davis, D.W., and Kamo, S.L., 1991, U-Pb Ages on Single Detrital Zircon Grains from the Witwatersrand Basin, South Africa: Constraints on the Age of Sedimentation and on the Evolution of Granites Adjacent to the Basin: A Reply: The Journal of Geology, v. 99, no. 3, p. 495–496, doi: 10.1086/629510.

Robb, L.J., and Robb, V.M., 1998, Gold in the Witwatersrand basin: Mineral Resources of South Africa, p. 294–349.

Schidlowski, M., 1981, Uraniferous constituents of the Witwatersrand conglomerates: ore-microscopic observations and implications for the Witwatersrand metallogeny, *in* Genesis of Uranium- and Gold-Bearing Precambrian Quartz-Pebble Conglomerates. US Geological Survey Professional Paper 1161N, Golden, Colorado, p. N1 – 29.

Smieja-Król, B., Duber, S., and Rouzaud, J.N., 2009, Multiscale organisation of organic matter associated with gold and uranium minerals in the Witwatersrand basin, South Africa: International Journal of Coal Geology, v. 78, no. 1, p. 77–88, doi: 10.1016/j.coal.2008.09.007.

Smith, N.D., and Minter, W.E.L., 1980, Sedimentological controls of gold and uranium in two Witwatersrand paleoplacers: Economic Geology, v. 75, no. 1, p. 1–14, doi: 10.2113/gsecongeo.75.1.1.

Spangenberg, J.E., and Frimmel, H.E., 2001, Basin-internal derivation of hydrocarbons in the Witwatersrand Basin, South Africa: evidence from bulk and molecular δ13C data: Chemical Geology, v. 173, no. 4, p. 339–355, doi: 10.1016/S0009-2541(00)00283-7.

Tonžetić, I.Ž., 2015, Quantitative analysis of iron ore using SEM-based technologies: Iron Ore: Mineralogy, Processing and Environmental Sustainability, p. 161.

Van der Westhuizen, W.A., De Bruiyn, H., and Meintjes, P.G., 1991, The Ventersdorp supergroup: an overview: Journal of African Earth Sciences, v. 13, no. 1, p. 83–105, doi: 10.1016/0899-5362(91)90045-Z.

Woods, T.H., Drennan, G.R., and Durbach, S.H., 2016a, Simulating U-C Associations: An Experimental Approach to Modelling the Mineralization Processes in the Witwatersrand Basin, South Africa: Geochimica et Cosmochimica Acta, v. Submitted.

Woods, T.H., Drennan, G.R., and Przybylowicz, W.J., 2016b, Elemental Micromaps of Au-U-C associations in Carbon Seams from the Witwatersrand Basin: Evidence for Multi-Component, Multi-Fluid Remobilisation of Mineralisation: Ore Geology Reviews, v. Submitted.

Appendix B: Sample List for this study

Reef	Sample	Description	Locality	Source
Basal Reef	PS10	President Steyn Gold Mine	President Steyn Gold Mine	Gill Old Samples
	LGM 16	Very pale quartzite reef with a thin carbon seam	Loraine Gold Mine	SH Basement
	LGM 5	25 cm thick Carbon Seam	Loraine Gold Mine	SH Basement
	LGM 5	Thick Carbon Seam with quartzite and pebble conglomerate either side	Loraine Gold Mine	SH Basement
	LGM1	Thick sulphide vein along base of pebble conglomerate	Loraine Gold Mine	SH Basement
	LGM 6	Carbon nodules around quartz pebbles	Loraine Gold Mine	SH Basement
	LGM2	Multiple Pyrite bands in along base of pebble conglomerate	Loraine Gold Mine	SH Basement
	LGM3	Very pale quartzite reef with a thin carbon seam	Loraine Gold Mine	SH Basement
Beisa Reef	Bei 1B	Pebble conglomerate with rounded pyrite and nodular carbon	President Steyn Gold Mine	Gill Old Samples
	Bei 3B	Pebble conglomerate with large interlocking pyrite and no apparent carbon	President Steyn Gold Mine	Gill Old Samples
	Bei 1A	Pebble conglomerate with rounded pyrite and small isolated carbon seam	President Steyn Gold Mine	Gill Old Samples
	Bei 3A	Pebble conglomerate with rounded pyrite and no apparent carbon	President Steyn Gold Mine	Gill Old Samples
	Bei1	2 cm thick discontinuous carbon seams	President Steyn Gold Mine	Gill Old Samples
	Breef	Quartzite with thin discontinuous carbon seam at base	Free State Geduld Mine	SH Basement

Reef	Sample	Description	Locality	Source
"C" Reef	CREEF01 EM1	Carbon seam in a quartzite cut by a quartz vein	Blyvooruitzicht Gold Mine	Blyvooruitzicht Gold Mine
	CREEF01 EM2	Small pebble conglomerate, almost no rounded pyrite, minor nodular carbon	Blyvooruitzicht Gold Mine	Blyvooruitzicht Gold Mine
	CREEF01 EM3	Small pebble conglomerate, large amounts of rounded pyrite, no apparent carbon	Blyvooruitzicht Gold Mine	Blyvooruitzicht Gold Mine
	CREEF01 EM4	Small pebble conglomerate, large amounts of rounded pyrite, no apparent carbon	Blyvooruitzicht Gold Mine	Blyvooruitzicht Gold Mine
	CREEF01 EM5	Small pebble conglomerate, almost no rounded pyrite, no apparent carbon	Blyvooruitzicht Gold Mine	Blyvooruitzicht Gold Mine
	CREEF01 EM6	Quartzite, large amounts of rounded pyrite, minor nodular carbon	Blyvooruitzicht Gold Mine	Blyvooruitzicht Gold Mine
	CREEF07	Small pebble conglomerate, almost no rounded pyrite, centimetre thick carbon seam	Blyvooruitzicht Gold Mine	Gill Old Samples
	VRS1A	Pebble conglomerate with discontinuous seam carbon that is very distorted	Blyvooruitzicht Gold Mine	Gill Old Samples
Carbon Leader Reef	WD20	Quartzite with 2 carbon seams, one thicker than the other	West Driefontein	SH Basement
	BVU 1	Green bar shale with bands of sulphide minerals	Blyvooruitzicht Gold Mine	SH Basement
	BVU 5	Quartzite with thin carbon seam at base	Blyvooruitzicht Gold Mine	SH Basement
	DFN 10	Thick carbon seam in a reef sample displacing a quartz pebble	Doornfontein Gold Mine	SH Basement
	CLRSS1	Centimetre thick carbon seam with visible gold in between carbon spindles	CLR, carbon seam with visible gold	Richard Viljoen
	CLRRV1	2 Centimetre thick carbon seam only, small amounts of gold between spindles	West Driefontein Mine, 5 West area, 1980	Richard Viljoen
	CLRRV2	Large pebble conglomerate with high concentrations of small rounded pyrite in matrix	West Driefontein Mine, 5 West area, 1980	Richard Viljoen
	CLRRV3	Quartzite with large pebbles in HW, 5 mm thick carbon seam undulates along FW contact	West Driefontein Mine, 5 West area, 1980	Richard Viljoen
	CLRRV4	Quartzite with large pebbles in HW, 5 mm thick carbon seam undulates along FW contact	West Driefontein Mine, 5 West area, 1980	Richard Viljoen
	CLRRV5	5 mm thick carbon seam with visible gold in between carbon spindles	Western Ultradeeps	Richard Viljoen

Reef	Sample	Description	Locality	Source
Dominion Reef	BDN	Dark quartzite chip, small rounded pyrite and no apparent carbon	Buffelsdoorn South Gold Mine	SH Basement
	BDN2	Quartzite with rounded pyrite grains	Buffelsdoorn South Gold Mine	SH Basement
Elsburg Reef	VRW3	Large pebble conglomerate with small rounded pyrite surrounding pebbles and ß-uranophane staining	Vaal Reef Gold Mine	Gill Old Samples
Kimberley Reef	MVA	Small pebble conglomerate along scoured surface, no apparent pyrite or carbon	Marie Vale, Kimberley Reef	SH Basement
Main Reef Leader	MGS4061	Main Reef Leader, replaced by pyrites from Modder East Gold Mine	Modder East Gold Mine	CGS
	MGS4076	C seam in main reef leader FW, hi grade, from New Moddderfontein Gold Mine	New Modderfontein Gold Mine	CGS
	MGS4063	Main reef leader, with carbon seam and shale below, from Modder East Gold Mine	Modder East Gold Mine	CGS
	MGS4071	Main reef leader, with carbon seam and shale below, from Modder East Gold Mine	Modder East Gold Mine	CGS
	MGS4072	Main Reef Leader, partially replaced by pyrites from Modder East Gold Mine	Modder East Gold Mine	CGS
	RDEEP 12	Main Reef Leader, "south reef"	Rose Deep Gold Mine	SH Basement
May Reef	MGS4355	May Reef, in Kimberly Reef Group, Rich in C, from East Daggafontein Mine	East Daggafontein Mine	CGS
Middevlei	LibGM 17	Large pebble conglomerate, no apparent carbon or pyrite	Libanon Gold Mine	SH Basement
	LibGM 14/15	Large pebble conglomerate, no apparent carbon or pyrite, but ß-uranophane staining	Libabnon Gold Mine	SH Basement
Rose Reef	RDEEP 11	Rose Reef (Bastard) with visible gold	Rose Deep Gold Mine	SH Basement
	RDEEP 10	Rose Reef (Bastard) dark quartzite matrix with white pebbles, small rounded pyrite and no apparent carbon	Rose Deep Gold Mine	SH Basement
South Reef	EG37	Large pebble conglomerate with small rounded pyrite in matrix, no apparent carbon	East Geduld Gold Mine	SH Basement

Reef	Sample	Description	Locality	Source
Steyn Reef	PSGM	Thin discontinuous carbon seam at base	President Steyn Gold Mine	SH Basement
Vaal Reef	MGS6513	Gold ore, Vaal Reef, from Hartebeesfontein Gold Mine, Stilfontein	Hartebeesfontein Gold Mine	CGS
	MGS6514	Gold ore, Vaal Reef, from Hartebeesfontein Gold Mine, Stilfontein	Hartebeesfontein Gold Mine	CGS
	MGS6512	Vaal reef, from Buffelsfotein Gold Mine	Buffelsfotein Gold Mine	CGS
	MGS6510	Vaal reef, visible au in c, very radioactive, from main bird series in Hartebeesfontein Gold Mine	Hartebeesfontein Gold Mine	CGS
	VR4	Quartzite and pebble conglomerate with small rounded pyrite and no apparent gold	Vaal Reef Gold Mine	Gill Old Samples
	VRW1A	Quartz vein with nodular carbon material that cuts Vaal Reef	Vaal Reef Gold Mine	Gill Old Samples
	VR6	Thin carbon seam in quartzite	Vaal Reef Gold Mine	Gill Old Samples
	VRS423	Flyspeck carbon at base of "C" reef	Vaal Reef Gold Mine	Gill Old Samples
	VR4C	Vaal Reef West, carbon in reef	Vaal Reef Gold Mine	Gill Old Samples
	VRSS1A	Carbon , quartz vein and Vaal Reef	Vaal Reef Gold Mine	Gill Old Samples
VCR	VCR1	Large pebble conglomerate with no apparent carbon	Western Deeps Gold Mine	SH Basement
	VCR3	Large pebble conglomerate with no apparent carbon	Western Deeps Gold Mine	SH Basement
	VCR4	VCR chips with pyrite, bornite and other sulphides	Western Deeps Gold Mine	SH Basement

Appendix C: Microscope Petrography Summary Tables

C1: Sample descriptions

Reef	Sample	Mineralogy	Textures and Features	Alteration	Carbon-Uranium-Gold-Pyrite
Basal Reef	PS10	Small pebble conglomerate (1 - 12 mm), with a quartz (0.5-2 mm), sulphide (0.5 -1 mm) and phyllosilicate (<0.2 mm) matrix. Sample has a 1 mm thick carbon seam (2 mm in length) with a number of carbon nodules. There are a number of fractured grains within the carbon seam, the fractures are parallel to bedding. Quartz: 60%; Sulphides: 30%; Phyllosilicates: 5%; Carbon: 5%.	Sample appears dominantly sedimentary in nature, rounded clasts deformed and interlocking. Alignment of minerals along bedding plane	Alteration mineral occur in small proportions in the fine matrix with no discernible separate phases - pyrophyllite: 15%; sericite: 45%; secondary quartz: 25%; muscovite: 5% and chlorite/chloritoid: 10%.	Abundant rounded pyrite, some minor euhedral and spongy pyrite and secondary pyrite in a large quartz grain. There is little to no visible U/Au or C in this sample
	LGM 16	Pebble conglomerate (10 - 30 mm) with a matrix of smaller quartz grains, nodular carbon and rounded pyrites (0.5 - 3 mm) and very fine grained phyllosilicates between them. Quartz: 60%; Sulphides: 30%; Phyllosilicates: 5%; Carbon: 5%.	Section is taken parallel to bedding to sample the most carbon and sulphides. Sample appears dominantly sedimentary in nature	Alteration mineral occur in small proportions in the fine matrix with no discernible separate phases - pyrophyllite: 20%; sericite: 15%; secondary quartz: 35%; muscovite: 10% and chlorite/chloritoid: 20%.	This sample contains very small amounts of carbon as nodular carbon, there is no U associated with it. There is however, a few small rounded uraninite nodules (<0.5mm), and there is not much secondary U in the sample. The pyrite in this sample is very fractured and the spaces are filled in by alteration minerals, the small amount of Au in the sample is found within pyrite grains and along the fractured altered features
	LGM 5	20 mm Carbon seam dominates sample, with large pebble conglomerate at the base (5 - 15 mm). Seam contains phyllosilicates (<0.2 mm) and quartz material (1 - 4 mm). There is little or no sulphides in the sample. Quartz: 30%; Sulphides: <1%; Phyllosilicates: 5%; Carbon: 64%	Sample has a number of bedding parallel veinlets infilled by alteration minerals, especially at the base of the carbon seam	Alteration mineral occur in small proportions in the fine matrix with no discernible separate phases - pyrophyllite: 20%; sericite: 40%; secondary quartz: 25%; muscovite: 5% and chlorite/chloritoid: 10%.	The sample has a thick carbon seam with only a few visible grains of pyrite. The spindles are not particularly well developed, and there is not much Au. The seam does have abundant uraninite grains (<0.05 mm) with minor brannerite/coffinite in the matrix. Within the seam there are smaller rounded forms of hydrocarbon (surrounding U) within the seam .The base of the conglomerate also has hydrocarbon filling the interstices between the quartz clasts.
	LGM1	Quartzite reef (0.5 - 3 mm). Alignment of pyrite grains and carbon nodules parallel to bedding. There is an abundance of fine grained sericite and phlogopite (<0.1 mm) between the quartz grains, with no visible carbon. Finally, at the base of the reef there is layer of anhedral or interstitial coffinite/brannerite at base of section. Quartz: 89%; Sulphides: <1%; Phyllosilicates: 10%	Sample appears dominantly sedimentary in nature, rounded clasts deformed and interlocking. Alignment of minerals along bedding plane	Alteration mineral occur in small proportions in the fine matrix with no discernible separate phases - pyrophyllite: 20%; sericite: 40%; secondary quartz: 25%; muscovite: 5% and chlorite/chloritoid: 10%.	The carbon seams are comprised of rounded nodules aligned with bedding, sulphides occur in close abundance. Gold occurs near or around the sulphides and carbon. There is abundant visible gold in this sample. U occurs as interstitial brannerite/coffinite within the sample, however there is very little visible uraninite within the carbon
	LGM 6	Quartzite reef (0.5 - 3 mm) with some larger pebble grains (6 - 15 mm). Randomly dispersed pyrite grains and carbon nodules parallel to bedding. There is an abundance of fine grained sericite and phlogopite (<0.1 mm) between the quartz grains. Quartz: 80%; Sulphides: 10%; Phyllosilicates: 5%; Carbon: 5%	Sample appears dominantly sedimentary in nature	Alteration mineral occur in small proportions in the fine matrix with no discernible separate phases - pyrophyllite: 20%; sericite: 40%; secondary quartz: 25%; muscovite: 5% and chlorite/chloritoid: 10%.	This sample contains some nodular carbon and rounded pyrite. Here the carbon follows the interstitial shape of the quartz/sulphide grains it is found between, There is very little U in the sample, barely any is seen in the carbon. Interestingly, the Au is small (<0.02 mm) and occurs within the phyllosilicate matrix and not within carbon or sulphides
	LGM3	Pebble conglomerate (20 - 40 mm) at base, with 3 mm thick seam and quartzite hanging wall (1 - 4 mm). Fine grained phyllosilicate matrix (<0.2 mm) and minor sulphide minerals within pebble conglomerate. Quartz: 70%; Sulphides: 5%; Phyllosilicates: 8%; Carbon: 15%; Uraninite: 2%	Sample appears dominantly sedimentary in nature	Alteration mineral occur in small proportions in the fine matrix with no discernible separate phases - pyrophyllite: 15%; sericite: 45%; secondary quartz: 25%; muscovite: 5% and chlorite/chloritoid: 10%.	Discontinuous carbon seam with quartz, chlorite and pyrite perpendicular to elongated spindles. At the thickest part of the seam spindles are well-developed with gold between the filaments. Abundant uraninite grains (<0.05mm) with some rounded pyrite included in the seam material.
Beisa Reef	Bei 1B	Small pebble conglomerate (1 - 12 mm), with a quartz (0.5-2 mm), sulphide (0.5 -1 mm) and phyllosilicate (<0.2 mm) matrix. Sample has a 1 mm thick carbon seam (2 mm in length) with a number of carbon nodules. There are a number of fractured grains within the carbon seam, the fractures are parallel to bedding. Quartz: 60%; Sulphides: 30%; Phyllosilicates: 5%; Carbon: 5%.	Sample appears dominantly sedimentary in nature, with a carbon seam. Sample is severely fractured parallel to bedding, these fractures are infilled by sulphides, carbon and other secondary phases	Unidentifiable, sample prepared as ore block	Mostly rounded pyrite throughout sample, but highest concentration occurs near the reef portion along with the carbon seam. There are also a number of rims and overgrowths on quartz grains. There are a number rounded uraninite grains just below the seam and some secondary brannerite/coffinite between the quartz grains. The seam carbon is mostly a mass that includes some pyrite, quartz and plenty of small uraninite grains. The seam occurs interstitially to the quartz, pyrite and uraninite. There is only a small amount of Au concentrated near the seam but not within it.
	Bei 3B	Small pebble conglomerate (1 - 8 mm), with a quartz (0.5-2 mm) and phyllosilicate (<0.2 mm) matrix. The sample has masses of rounded and euhedral sulphides within secondary sulphide matrix as well as in the conglomerate portion. There are a number of fractured grains within the carbon seam, the fractures are parallel to bedding. Quartz: 49%; Sulphides: 45%; Phyllosilicates: 5%; Carbon: 1%.	Sample appears dominantly sedimentary in nature, with a carbon seam. Sample is severely fractured parallel to bedding, these fractures are infilled by sulphides, carbon and other secondary phases. There is also a large quartz veinlet through the sample	Unidentifiable, sample prepared as ore block	Mostly rounded pyrite throughout sample, within secondary anhedral sulphide matrix. There are also a number of rims and overgrowths on quartz grains. There are a number larger rounded uraninite grains (0.5 mm) within the seam and some secondary brannerite/coffinite between the quartz grains. The carbon occurs as nodules interstitially to the quartz, pyrite and uraninite. There is no visible Au
	Bei 1A	Small pebble conglomerate (1 - 12 mm), with a quartz (0.5-2 mm), sulphide (0.5 -1 mm) and phyllosilicate (<0.2 mm) matrix. Sample has a 1 mm thick carbon seam with a number of carbon nodules. There are a number of fractured grains within the carbon seam, the fractures are parallel to bedding. Quartz: 70%; Sulphides: 15%; Phyllosilicates: 5%; Carbon: 10%.	Sample appears dominantly sedimentary in nature, with a carbon seam	Unidentifiable, sample prepared as ore block	Mostly rounded pyrite throughout sample, but highest concentration occurs near the reef portion along with the carbon seam. There are also a number of rims and overgrowths on quartz grains. There are a number rounded uraninite grains just below the seam and some secondary brannerite/coffinite between the quartz grains. The seam carbon has some spindles but is mostly a mass that includes some pyrite, quartz and plenty of small uraninite grains. There is only a small amount of Au concentrated near the seam but not within it.
	Bei 3A	Small pebble conglomerate (1 - 12 mm), with a quartz (0.5-2 mm), sulphide (0.5 -1 mm) and phyllosilicate (<0.2 mm) matrix. Sample has a discontinuous 1 mm thick carbon seam with a number of carbon nodules. There are a number of fractured grains within the carbon seam, the fractures are parallel to bedding. Quartz: 60%; Sulphides: 30%; Phyllosilicates: 5%; Carbon: 5%.	Sample appears dominantly sedimentary in nature, with a carbon seam. Sample is severely fractured parallel to bedding, these fractures are infilled by sulphides, carbon and other secondary phases	Unidentifiable, sample prepared as ore block	Mostly rounded pyrite throughout sample, but highest concentration occurs near the reef portion along with the carbon seam. There are also a number of rims and overgrowths on quartz grains. There are a number larger rounded uraninite grains (0.5 mm) within the seam and some secondary brannerite/coffinite between the quartz grains. The seam carbon is mostly a mass that includes some pyrite, quartz and plenty of small uraninite grains. The seam occurs interstitially to the quartz, pyrite and uraninite. There is only a small amount of Au concentrated near the seam but not within it.
	Bei1	Small pebble conglomerate (1 - 12 mm), with a quartz (0.5-2 mm), sulphide (0.5 -1 mm) and phyllosilicate (<0.2 mm) matrix. Sample has multiple discontinuous 8 mm thick carbon seam with a number of carbon nodules in the pebble matrix. There are a number of fractured grains within the carbon seam, the fractures are parallel to bedding. Quartz: 40%; Sulphides: 25%; Phyllosilicates: 5%; Carbon: 30%.	Sample appears dominantly sedimentary in nature, with a carbon seam. Sample is severely fractured parallel to bedding, these fractures are infilled by sulphides, carbon and other secondary phases	Unidentifiable, sample prepared as ore block	Mostly rounded pyrite throughout sample, but highest concentration occurs near the reef portion along with the carbon seam. There are also a number of rims and overgrowths on quartz grains. There are a number larger rounded uraninite grains (0.5 mm) within the seam and some secondary brannerite/coffinite between the quartz grains. The seam carbon is mostly a mass that includes some pyrite, quartz and plenty of small uraninite grains. The seam occurs interstitially to the quartz, pyrite and uraninite. There is only a small amount of Au concentrated near the seam but not within it.

Reef	Sample	Mineralogy	Textures and Features	Alteration	Carbon-Uranium-Gold-Pyrite
"C" Reef	CREEF EM1 OB	Quartzite sample (1 - 3 mm) with fine grained phyllosilicate matrix. Numerous rounded sulphide grains aligned parallel to bedding. Quartz: 83%; Sulphides: 7%; Phyllosilicates: 10%.	Sample appears dominantly sedimentary in nature, but it is severely fractured with alteration minerals developed within the fractures	Unidentifiable, sample prepared as ore block	There are minor small rounded pyrite grains and some small inclusions of pyrite in secondary phyllosilicate phases. There are a couple of uraninite grains within the quartzite, but no secondary U. There is no visible C or Au
	CREEF EM2 OB	Quartzite sample (1 - 3 mm) with fine grained phyllosilicate matrix. Numerous rounded sulphide grains aligned parallel to bedding. Quartz: 74%; Sulphides: 15%; Phyllosilicates: 10%; Carbon: <1%.	Sample appears dominantly sedimentary in nature, but it is severely fractured with alteration minerals developed within the fractures	Unidentifiable, sample prepared as ore block	There are abundant small rounded pyrite grains and some small inclusions of pyrite in secondary phyllosilicate phases. There plenty of uraninite grains within the quartzite, as well as a number of secondary brannerite/coffinite mineralisation. There are some rounded grains of Au within the larger clasts, as well as a small interstitial portion of Au associated with GREY MINERAL. There is abundant C nodules within the sample, they are interstitial to quartz, and pyrite.
	CREEF EM3 OB	Small pebble conglomerate (1 - 12 mm), with a quartz (0.5-2 mm) with fine grained phyllosilicate matrix. Abundant rounded sulphide grains aligned parallel to bedding, small discontinuous carbon seam (0.5 mm thick). Quartz: 89%; Sulphides: <1%; Phyllosilicates: 10%.	Sample appears dominantly sedimentary in nature, but it is severely fractured with alteration minerals developed within the fractures	Unidentifiable, sample prepared as ore block	Mostly rounded pyrite throughout sample, but highest concentration occurs near the reef portion along with the carbon seam. There are also a number of rims and overgrowths on quartz grains. There are a number rounded uraninite grains just below the seam and some secondary brannerite/coffinite between the quartz grains. The seam carbon has no spindles but is mostly a mass that includes some pyrite, quartz and plenty of small uraninite grains. There is only a small amount of Au concentrated near the seam but not within it.
	CREEF EM4 OB	Small pebble conglomerate (1 - 12 mm), with a quartz (0.5-2 mm) with fine grained phyllosilicate matrix. Few rounded sulphide grains aligned parallel to bedding. Quartz: 89%; Sulphides: <25%; Phyllosilicates: 10%.	Sample appears dominantly sedimentary in nature, but it is severely fractured with alteration minerals developed within the fractures	Unidentifiable, sample prepared as ore block	There are minor small rounded pyrite grains and some small inclusions of pyrite in secondary phyllosilicate phases. There are a couple secondary brannerite/coffinite interstitial occurrences. There is no visible C or Au
	CREEF EM1	Quartz vein cross-cutting a carbon seam from a conglomerate. Sample taken only from carbon seam and vein portion. Carbon: 30% ; Quartz vein: 45%; Sulphides: <1%; Phyllosilicates: 24%.	Numerous fractures and veinlets containing sulphides and altered minerals	Alteration mineral occur in small proportions in the quartz vein and between carbon filaments with no discernible separate phases - pyrophyllite: 20%; sericite: 30%; secondary quartz: 25%; muscovite: 5% and chlorite/chloritoid: 20%.	Carbon seam has well developed filaments and was cut perpendicular to the long axis of the filaments (parallel to bedding). Between filaments pyrite is found as well as abundant Au. Fractured uraninite grains are abundant within the centres of the filaments with very minor secondary brannerite/coffinite between the filaments
	CREEF EM2	Large pebble conglomerate (2 - 15 mm), with a quartz (1-2 mm), sulphide (0.5 - 2 mm) and phyllosilicate (<0.2 mm) matrix. Quartz: 70%; Sulphides: 15%; Phyllosilicates: 15%. Additionally, there are 2 large regions of secondary mineralisation of quartz, sericite and pyrophyllite within the sample	Sample appears dominantly sedimentary in nature	Alteration mineral occur in small proportions in the fine matrix with no discernible separate phases - pyrophyllite: 20%; sericite: 40%; secondary quartz: 25%; muscovite: 5% and chlorite/chloritoid: 10%.	Sample is dominated by rounded pyrites, with some euhedral grains. Between the pyrite grains are a few c nodules, peculiarly these nodules are not rounded and are found around the pyrite grains. There is some minor secondary brannerite/coffinite which also occurs in the interstices between pyrite and quartz. Finally there are small occurrences of gold in the phyllosilicate matrix, as well as in the quartz grains.
	CREEF EM3	Quartzite sample (1 - 3 mm) with fine grained phyllosilicate matrix. Numerous rounded sulphide grains aligned parallel to bedding. Quartz: 79%; Sulphides: 1%; Phyllosilicates: 20%.	Sample appears dominantly sedimentary in nature, a number of fractures running through the sample with phyllosilicate and sulphide mineralisation	Alteration mineral occur in small proportions in the fine matrix with no discernible separate phases - pyrophyllite: 20%; sericite: 40%; secondary quartz: 25%; muscovite: 5% and chlorite/chloritoid: 10%.	There are minor small rounded pyrite grains and some small inclusions of pyrite in secondary phyllosilicate phases, especially along fractures. There are a few secondary brannerite/coffinite interstitial occurrences. There is no visible C or Au
	CREEF EM4	Large pebble conglomerate (5- 15 mm), with a quartz (1-4 mm), sulphide (0.5 - 2 mm) and phyllosilicate (<0.2 mm) matrix. Quartz: 70%; Sulphides: 20%; Phyllosilicates: 15%. Additionally there are a number of larger pyophyllite and sericite mineralised areas and an alignment of minerals with bedding	Sample appears dominantly sedimentary in nature	Alteration mineral occur in small proportions in the fine matrix with no discernible separate phases - pyrophyllite: 40%; phlogopite: 10%; sericite: 20%; secondary quartz: 20%; muscovite: 5%; and chlorite/chloritoid: 5%.	Sample is dominated by rounded pyrites, with some euhedral grains, these are aligned with bedding. Between the pyrite grains are few nodules. There are abundant secondary brannerite/coffinite which also occurs in the interstices between pyrite and quartz. There is no visible Au in this sample
	CREEF EM5	Quartzite sample (1 - 3 mm) with fine grained phyllosilicate matrix. Numerous rounded sulphide grains aligned parallel to bedding. Quartz: 79%; Sulphides: 1%; Phyllosilicates: 20%.	Sample appears dominantly sedimentary in nature, a number of fractures running through the sample with phyllosilicate and sulphide mineralisation	Alteration mineral occur in small proportions in the fine matrix with no discernible separate phases - pyrophyllite: 20%; sericite: 40%; secondary quartz: 25%; muscovite: 5% and chlorite/chloritoid: 10%.	There are minor small rounded pyrite grains and some small inclusions of pyrite in secondary phyllosilicate phases, especially along fractures. There are a few secondary brannerite/coffinite interstitial occurrences. There is no visible C or Au
	CREEF EM6	Large pebble conglomerate (5- 12 mm), with a quartz (1-4 mm), sulphide (0.5 - 2 mm) and phyllosilicate (<0.2 mm) matrix. Quartz: 70%; Sulphides: 20%; Phyllosilicates: 15%. Additionally there are a number of larger pyophyllite and sericite mineralised areas, particularly a large replaced clast in the centre of the reef portion. Finally, there is an alignment of minerals with bedding	Sample appears dominantly sedimentary in nature, although there are abundant fractures and veinlets	Alteration mineral occur in small proportions in the fine matrix with no discernible separate phases - pyrophyllite: 30%; phlogopite: 10%; sericite: 30%; secondary quartz: 20%; muscovite: 5%; and chlorite/chloritoid: 5%.	Sample is dominated by rounded pyrites, with some euhedral grains, these are aligned with bedding. Between the pyrite grains are few c nodules, peculiarly these nodules are not rounded and are found around the pyrite grains. There are abundant secondary brannerite/coffinite which also occurs in the interstices between pyrite and quartz. There is a number of rounded and skeletal grains within the large pebble replaced with sericite, secondary quartz and pyrophyllite.
	CREEF07	Pebble conglomerate (10 - 40 mm) with a matrix of smaller quartz grains, nodular carbon and pyrites (0.5 - 3 mm) and very fine grained phyllosilicates between them. Quartz: 55%; Sulphides: 15%; Phyllosilicates: 20%; Hydrocarbons: 10%.	Sample appears dominantly sedimentary in nature, but it is severely fractured with alteration minerals developed within the fractures	Alteration mineral occur in small proportions in the fine matrix with no discernible separate phases - pyrophyllite: 30%; phlogopite: 10%; sericite: 30%; secondary quartz: 20%; muscovite: 5%; and chlorite/chloritoid: 5%.	The sulphides are mostly rounded and occur sporadically, the sulphide surfaces are partially overgrown by the carbon and in the largest chunk of carbon there is a small amount of Au. Besides minor U as coffinite/brannerite in the matrix there is no visible uraninite within the carbon

Reef	Sample	Mineralogy	Textures and Features	Alteration	Carbon-Uranium-Gold-Pyrite
Carbon Leader Reef	WD20	Large pebble conglomerate (2 - 20 mm), with a quartz (0.5-2 mm), sulphide (0.5 -1 mm) and phyllosilicate (<0.2 mm) matrix. That sample has numerous irregular carbon nodules that clump to form discontinuous seams. Quartz: 50%; Sulphides: 5%; Phyllosilicates: 20%; Hydrocarbons: 25%	Sample appears to have had the original sedimentary nature overprinted by fractures, veinlets and large chlorite laths and other secondary minerals that are parallel to bedding	Alteration minerals occur in very small proportions in the fine matrix with some discernible separate phases, additionally a large portion are found in veinlets connecting the hydrocarbons - pyrophyllite : 15%; phlogopite: 10%; sericite: 45%; secondary quartz: 10%; muscovite: 10% and chlorite/chloritoid: 10%.	Sample contains a concentrically laminated pyrite at the base of the carbon, but pyrite occurs mostly as rounded and anhedral forms distributed evenly throughout the samples. There is some spindle development in the thicker hydrocarbon forms. Very small carbon nodules also occur in the bedding parallel veinlets. There is abundant small uraninite grains in the carbon materials. Secondary brannerite/coffinite occurs in the phyllosilicate materials. There is abundant small scale gold within the carbon seam and nodule material as well as in close proximity within the phyllosilicate materials
	BVU 1	Fine grained green bar shale, abundant alteration minerals (<0.2 mm) with wide scale mineralisation. Quartz has fine grained (<0.1mm) texture with sericite and muscovite mineralisation within. The sulphides present are pyrite, pyrrhotite and chalcopyrite (plus minor galena). Quartz: 29%; Sulphides: 50%; Phyllosilicates: 20%; Hydrocarbons: <1%	Sample shows abundant euhedral sulphides with anhedral silicate material in the spaces between the sulphides	Alteration mineral occur in very small proportions in the fine matrix. Pyrophyllite : 15%; phlogopite: 10%; sericite: 45%; secondary quartz: 10%; muscovite: 10% and chlorite/chloritoid: 10%.	Although there is abundant sulphide, there is no Au or C in the green bar shale. There is minor U associated with galena, between sulphide grains
	BVU 5	Pebble conglomerate (5 - 20 mm) with quartzite matrix (1 - 3 mm) and minor phyllosilicates. 2 small discontinuous carbon seams. One large quartzite clast has large amounts of euhedral to subhedral pyrite and chalcopyrite (<1 mm) within them. Quartz: 75%; Sulphides: 10%; Phyllosilicates: 10%; Hydrocarbons: 5%	Sample appears dominantly sedimentary in nature with no secondary features	Alteration minerals are uncommon, however highest proportions are found surrounding the 2 carbon seams. Alteration minerals in the fine matrix: pyrophyllite : 15%; phlogopite: 10%; sericite: 45%; secondary quartz: 10%; muscovite: 10% and chlorite/chloritoid: 10%.	The carbon seams are less than 1 mm in thickness and are discontinuous with no spindles developed, these seams contain little gold as inclusions within the carbon and very little U as uraninite grains
	DFN 10	Quartzite sample (1 - 4 mm), with abundant sulphides (0.5 -1 mm) and phyllosilicate (<0.2 mm) matrix. Sample contains a discontinuous carbon seam 10 mm to 15 mm thick, additionally the seam is cut by bedding parallel calcite veins. Quartz: 55%; Sulphides: 5%; Phyllosilicates: 15% and Hydrocarbon: 25%.	Sample appears to have had the original sedimentary nature overprinted by fractures, veinlets and calcite veinlets parallel to bedding. There is also a 4 mm portion of secondary phyllosilicates not directly associated with the carbon seam. There are some dislocations of the sample from the preparation	Alteration mineral occur in very small proportions in the fine matrix with some discernible separate phases, additionally a large portion are found in veinlets connecting the hydrocarbons - pyrophyllite : 25%; phlogopite: 5%; sericite: 30%; secondary quartz: 10%; muscovite: 5%; calcite : 15% and chlorite/chloritoid: 10%.	Sample contains abundant rounded and subhedral pyrite and sphalerite. Grains within the phyllosilicate vein portion of the sample. There is small portion of Au in these veins. The seam is discontinuous and has some spindles in the thicker portion, the thicker seam also has far more Au and uraninite mineralisation. The thinner seam portion is cut by numerous calcite veinlets that cut the silicate material as well. The seam also contains highly fractured quartz material between that is filled with phyllosilicate minerals. There is abundant small scale brannerite/coffinite mineralisation.
	CLRSS1	Features discussed in-depth in Chapter 6			
Dominion Reef	BDN2	Quartzite reef matrix (2 mm aver) with some larger pebble clasts (<1 cm). Alignment of pyrite grains parallel to bedding and fine layer of anhedral coffinite/brannerite at base of section. Additionally, there are abundant subhedral zircon grains throughout the sample. Quartz: 55%; Sulphides: 15%; Phyllosilicates: 15%, Uranium minerals: 10% and Hydrocarbon: 5%.	Sample is cut by pyrite veinlets perpendicular to reef horizon, and skeletal textures around silicate grains	Alteration mineral occur in very small proportions in the fine matrix with no discernible separate phases - pyrophyllite : 15%; phlogopite: 10%; sericite: 45%; secondary quartz: 10%; muscovite: 10% and chlorite/chloritoid: 10%. Additional secondary brannerite/coffinite comprises a mineralised horizon.	U remobilised at base of sample, rounded grains uraninite also has skeletal texture. Pyrite veinlet doesn't contain Au within, but at veinlet ends there is strong gold mineralisation. There no clear C in the sample
Kimberley Reef	MVA	Quartzite sample (1 - 4 mm), with abundant sulphides (0.5 -1 mm) and phyllosilicate (<0.2 mm) matrix. Quartz: 85%; Sulphides: 1%; Phyllosilicates: 10%.	Sample appears dominantly sedimentary in nature	Alteration mineral occur in very small proportions in the fine matrix with no discernible separate phases - pyrophyllite : 15%; phlogopite: 10%; sericite: 45%; secondary quartz: 10%; muscovite: 10% and chlorite/chloritoid: 10%.	Very small amounts of mainly euhedral pyrite, and no visible C, U or Au
Main Reef Leader	MGS4061	Sample is comprised of dominantly euhedral to subhedral sulphides (1 - 7mm), with very small amounts of quartz grains (1 - 3 mm). These are completely surrounded by fine grained alteration minerals (< 0.2 mm). This sample is vastly different from typical quartzite/pebble conglomerate dominated reef samples. Quartz: 24%; Sulphides: 60%; Phyllosilicates: 15% and Hydrocarbon: <1%.	Sample has quartz and pyrite grains, with a matrix of phyllosilicate alteration minerals surrounding the grains	Alteration mineral occur in very small proportions in the fine matrix with no discernible separate phases - pyrophyllite : 15%; sericite: 45%; secondary quartz: 20%; muscovite: 10% and chlorite/chloritoid: 10%.	The abundant pyrite grains also contain inclusions of Au, the edges of the grains are partially fractured and have a skeletal texture. There is little to no U and only minor flyspeck carbon in this sample.
	MGS4076	Sample is comprised of a quartzite, a small pebble conglomerate horizon of 5 mm and a large pyrite grain (4 cm). Sample has one large fractured pyrite grain (~2 cm). The reef horizon has numerous small rounded pyrite grains (<0.5 mm). Quartz: 50%; Sulphides: 35% and Phyllosilicates: 15%	Sample appears dominantly sedimentary in nature with one large pyrite grain	Alteration mineral occur in very small proportions in the fine matrix with no discernible separate phases - pyrophyllite : 25%; sericite: 45%; secondary quartz: 10%; muscovite: 5% and chlorite/chloritoid: 15%.	The sample contains no visible C, and very few uraninite grains (<0.5 mm). There is no apparent gold and the sample has abundant rounded pyrite .
	MGS4063	Large pebble conglomerate footwall (2 cm), with a 3 mm reef section containing rounded quartz clasts (1 - 3 mm) and angular pyrites (0.05 mm - 1 mm) within a phyllosilicate matrix (<0.02 mm). Quartz: 75%; Sulphides: 5%; Phyllosilicates: 15% and Uranium minerals: 5%.	Sample shows abundant euhedral sulphides with anhedral silicate material in the spaces between the sulphides	Alteration mineral occur in very small proportions in the fine matrix with no discernible separate phases - pyrophyllite : 15%; phlogopite: 10%; sericite: 45%; secondary quartz: 10%; muscovite: 10% and chlorite/chloritoid: 10%.	The reef section contains abundant pyrite with skeletal or subhedral form. The pyrite grains also contain abundant Au, there is also smaller amounts of gold within the alteration mineral matrix. There is no visible carbon in the sample. There are relict uraninite grain rims with alteration minerals in the centre.
	MGS4071	Pebble conglomerate (10 - 40 mm) with a matrix of smaller quartz grains, and very fine grained phyllosilicates (<0.2 mm) between them. This sample has little to no sulphides and no visible carbon or uranium. However, there is an abundance of gold. Quartz: 81%; Sulphides: <1%; Phyllosilicates: 15% and Gold: 3%.	Sample appears dominantly sedimentary in nature, the sample is very fractured parallel to bedding and there are a number of quartz veinlets	Alteration mineral occur in very small proportions in the fine matrix with no discernible separate phases - pyrophyllite : 15%; phlogopite: 10%; sericite: 45%; secondary quartz: 10%; muscovite: 10% and chlorite/chloritoid: 10%. 2 large grains are replaced almost completely by alteration minerals	The sample contains no visible U or C. There are only 2 small areas with a few fine grained pyrites (<0.2 mm). The sample is unique in that gold is abundant between grains and in fractures, only a few grains are rounded and the remainder have a skeletal appearance
	MGS4072	Quartzite reef (0.5 - 3 mm) with abundant alteration minerals and rounded sulphides. The sulphides are moderately aligned parallel to bedding Sample has a green colour due to high content of chlorite/chloritoid. Quartz: 58%; Sulphides: 25%; Phyllosilicates: 15% and Uranium minerals: 2%.	Sample is extremely rich in alteration minerals. There are a number of quartz veinlets cutting through the sample parallel to bedding	Alteration mineral occur in very small proportions in the fine matrix with no discernible separate phases - pyrophyllite : 15%; phlogopite: 10%; sericite: 45%; secondary quartz: 10%; muscovite: 10% and chlorite/chloritoid: 10%.	The sample is dominated by rounded, euhedral and subhedral pyrite grains. Some grains are extremely fractured and cut by the quartz veinlets. Au occurs both in the phyllosilicate matrix, and most of the Au is within or associated with pyrite. There are a number of relict uraninite grains and interstitial brannerite/coffinite. No visible C is seen

Reef	Sample	Mineralogy	Textures and Features	Alteration	Carbon-Uranium-Gold-Pyrite
May Reef	MGS4355	Large pebble conglomerate (2 - 15 mm), with a quartz (1-2 mm), sulphide (0.5 - 2 mm) and phyllosilicate (<0.2 mm) matrix. Quartz: 75%; Sulphides: 10%; Phyllosilicates: 15%.	Sample appears dominantly sedimentary in nature	Alteration mineral occur in very small proportions in the fine matrix with no discernible separate phases - pyrophyllite : 20%; phlogopite: 5%; sericite: 20%; secondary quartz: 25%; muscovite: 5% and laths of chlorite/chloritoid: 25%.	Large portions of rounded and euhedral pyrite, dispersed throughout the sample, there are also a couple veinlets and fractures with smaller pyrite within. There is a larger portion of secondary brannerite/coffinite within the sample. There are a few C nodules that are rounded and occur between the interstices of the quartz and pyrite. Finally, there are a number of grains of Au, one rounded within a large pebble and one more angular within the matrix.
South Reef	EG37	Pebble conglomerate (20 - 50 mm) with a matrix of smaller quartz grains, pyrites (0.5 - 3 mm) and very fine grained phyllosilicates (<0.4mm) between them. Large clast of iron stone within the sample. Quartz: 69%; Sulphides: 15%; Phyllosilicates: 10%, Uranium minerals: <1% and Hydrocarbon: 5%.	Sample appears dominantly sedimentary in nature, but it is severely fractured	Alteration mineral occur in very small proportions in the fine matrix with no discernible separate phases - pyrophyllite : 20%; phlogopite: 5%; sericite: 20%; secondary quartz: 25%; muscovite: 5% and laths of chlorite/chloritoid: 25%. Alteration minerals generally surround hydrocarbons and sulphides	Large amount of rounded sulphide grains within the matrix. Little carbon present only as nodular carbon. Additionally there is a small number of uraninite grains although there is not much carbon associated with it. No visible gold is seen
Steyn Reef	OFS	Quartzite sample (1-4 mm), grains are sub-angular to angular and the sample contains abundant sulphides. There is a large concentration of phyllosilicate minerals between quartz grains. Quartz: 78%; Sulphides: 2%; Phyllosilicates: 20%.	Sample appears dominantly sedimentary in nature, but it is severely fractured with a number of inter connected quartz-sericite veinlets (up to 2 mm thick) cutting the sample	Alteration mineral occur in very small proportions in the fine matrix with no discernible separate phases - pyrophyllite : 25%: sericite: 30%; secondary quartz: 25%; muscovite: 10% and chlorite/chloritoid: 10%.	Sulphides occur as rounded pyrite and sphalerite, euhedral grains, interstitial masses of pyrite and a number of veinlets containing mainly pyrite. There is some minor brannerite/coffinite secondary mineralisation. There is no visible C or Au.
	PSGM	Large pebble conglomerate (2 - 15 mm), with a quartz (1-2 mm), sulphide (0.5 - 2 mm) and phyllosilicate (<0.2 mm) matrix. Numerous 1 -2 mm carbon nodules and discontinuous seams. Quartz: 65%; Sulphides: 15%; Phyllosilicates: 15% and Carbon: 5%.	Sample appears dominantly sedimentary in nature, but it is severely fractured with a number of inter connected quartz-sericite veinlets (up to 0.5 mm thick) cutting the sample	Alteration mineral occur in very small proportions in the fine matrix with no discernible separate phases - pyrophyllite : 35%: sericite: 35%; secondary quartz: 25%; and chlorite/chloritoid: 5%.	Numerous rounded and spongy pyrite grains, with few to no euhedral grains. Abundant uraninite within the carbon, and minor secondary brannerite/coffinite mainly concentrated near pyrite and carbon. The carbons form follows that of the surrounding silicates, and there aren't any well-developed spindles present. Gold is present in high concentrations within carbon materials, as well as in the phyllosilicate matrix close to the carbon and pyrite as well as in smaller concentrations further away.
Vaal Reef	MGS6513	Quartzite sample (1-4 mm), grains are sub-angular to angular and the sample contains abundant sulphides. There is a very small concentration of phyllosilicate minerals between quartz grains. Quartz: 65%; Sulphides: 25%; Phyllosilicates: 10%. And Carbon: 5%.	Sample appears dominantly sedimentary in nature, but it is severely fractured with sulphides concentrated in the fractures and a number of sulphide veinlets	Alteration mineral occur in very small proportions in the fine matrix with no discernible separate phases - pyrophyllite : 15%; phlogopite: 10%; sericite: 30%; secondary quartz: 25%; muscovite: 10% and chlorite/chloritoid: 10%.	Sulphides occur as rounded pyrite (with chalcopyrite. Inclusions) and sphalerite, euhedral grains, interstitial masses of pyrite and a number of veinlets containing mainly pyrite. There is some minor brannerite/coffinite secondary mineralisation. There is a very small carbon seam that is cut perpendicular to the long axis of the carbon spindles, very small Au particles within the carbon spindles as well as in the inter spindle spaces
	MGS6511	Quartzite sample (1 - 3 mm) with fine grained phyllosilicate matrix. Numerous layers of sulphide grains aligned parallel to bedding. Quartz: 75%; Sulphides: 15%; Phyllosilicates: 10%.	Sample appears dominantly sedimentary in nature	Alteration mineral occur in small proportions in the fine matrix with no discernible separate phases - pyrophyllite: 15%; sericite: 40%; secondary quartz: 25%; muscovite: 10%; and chlorite/chloritoid: 10%.	Numerous rounded sulphide grains, mostly pyrite aligned with bedding, a few uraninite grains and some minor secondary brannerite/coffinite. No visible C and no visible U
	MGS6512	Large pebble conglomerate (2 - 15 mm), with a quartz (1-2 mm), sulphide (0.5 - 2 mm) and phyllosilicate (<0.2 mm) matrix. Quartz: 70%; Sulphides: 15%; Phyllosilicates: 15%. Additionally, there are 2 large regions of secondary mineralisation of quartz, sericite and pyrophyllite within the sample	Sample appears dominantly sedimentary in nature	Alteration mineral occur in small proportions in the fine matrix with no discernible separate phases - pyrophyllite: 20%; sericite: 40%; secondary quartz: 25%; muscovite: 5% and chlorite/chloritoid: 10%.	Rounded and euhedral pyrite, pyrite overgrowths on quartz grains and uraninite grains. Very few uraninite grains (<0.5 mm) and minor brannerite/coffinite. No visible C, but minor Au in the phyllosilicate matrix.
	MGS6510	Quartzite sample (1 - 6 mm) with fine grained silicate matrix. Little to no sulphides or other minerals. Quartz: 84%; Sulphides: 1% and Phyllosilicates: 15%.	Sample appears dominantly sedimentary in nature	Alteration mineral occur in small proportions in the fine matrix with no discernible separate phases - pyrophyllite: 15%; sericite: 40%; secondary quartz: 25%; muscovite: 10%; and chlorite/chloritoid: 10%.	No visible C, U or Au in the sample. Small number of rounded and euhedral pyrite grains
	MGS6514	Large pebble conglomerate (2 - 15 mm), with a quartz (1-2 mm), sulphide (0.5 - 2 mm) and phyllosilicate (<0.2 mm) matrix. Quartz: 50%; Sulphides: 40%; Phyllosilicates: 10%. Additionally, there is an alignment of minerals with bedding	Sample appears dominantly sedimentary in nature	Alteration mineral occur in small proportions in the fine matrix with no discernible separate phases - pyrophyllite: 40%; sericite: 30%; secondary quartz: 10%; muscovite: 10%; and chlorite/chloritoid: 10%.	Sample is dominated by rounded pyrites, with some euhedral grains. The pyrite takes up all the matrix space between the pebble clasts. Between the pyrite grains are numerous c nodules, peculiarly these nodules are not rounded and are found around the pyrite grains. There is some minor secondary brannerite/coffinite which also occurs in the interstices between pyrite and quartz. Finally there are small occurrences of gold in the spaces between the pyrite, as well as in the pyrite grains.
	VR4G	Large pebble conglomerate (2 - 15 mm), with a quartz (1-2 mm), sulphide (0.5 - 2 mm) and phyllosilicate (<0.2 mm) matrix. Quartz: 75%; Sulphides: 10%; Phyllosilicates: 15%. Additionally, there is a large (12 mm) grain of pyrophyllite within the sample	Sample appears dominantly sedimentary in nature	Alteration mineral occur in very small proportions in the fine matrix with no discernible separate phases - pyrophyllite : 25%; phlogopite: 5%; sericite: 30%; secondary quartz: 25%; muscovite: 5% and chlorite/chloritoid: 10%.	Large portions of rounded and euhedral pyrite, dispersed throughout the sample, there are also a couple veinlets and fractures with smaller pyrite within. There is a larger portion of secondary brannerite/coffinite within the sample. There are C nodules that are not rounded and occur between the interstices of the quartz and pyrite. Finally, there are a number of grains of Au, one rounded within a large pebble and one more angular within the matrix.
	VRW1A	Large pebble conglomerate (2 - 20 mm), with a quartz (1-2 mm), sulphide (0.5 - 3 mm) and phyllosilicate (<0.2 mm) matrix. Quartz: 85%; Sulphides: 5%; Phyllosilicates: 10%. The sample is matrix supported, where as other conglomerate samples tend to be clast supported	Sample appears dominantly sedimentary in nature, although there are a number of sulphide veinlets and the pebble clasts are very fractured.	Alteration mineral occur in very small proportions in the fine matrix with no discernible separate phases - pyrophyllite : 15%; phlogopite: 5%; sericite: 40%; secondary quartz: 30%; muscovite: 5% and chlorite/chloritoid: 5%.	No visible C, U or Au in the sample. Small number of rounded and euhedral pyrite grains. Pyrite also occurs filling in veinlets and fractures

Reef	Sample	Mineralogy	Textures and Features	Alteration	Carbon-Uranium-Gold-Pyrite
Vaal Reef	VR6	Large pebble conglomerate (2 - 15 mm), with a quartz (1-2 mm), sulphide (0.5 - 2 mm) and phyllosilicate (<0.2 mm) matrix. Quartz: 50%; Sulphides: 40%; Phyllosilicates: 10%. Additionally, there is an alignment of minerals with bedding	Sample appears dominantly sedimentary in nature, although there are a number of sulphide veinlets and the pebble clasts are very fractured.	Unidentifiable, sample prepared as ore block	Sample is dominated by rounded pyrites, with some euhedral grains. The pyrite takes up all the matrix space between the pebble clasts. Between the pyrite grains are numerous c nodules, these rounded and are found around the pyrite grains. There is a 2 mm thick carbon seam at the base with well-developed spindles and gold between the spindles. There is some minor secondary brannerite/coffinite which also occurs in the interstices between pyrite and quartz. Finally there are small occurrences of gold in the spaces between the pyrite.
	MGS6512 OB	Quartzite sample (1-4 mm), grains are sub-angular to angular and the sample contains abundant sulphides. There is a very small concentration of phyllosilicate minerals between quartz grains. Additionally, there is a 0.5 mm thick carbon seam that is 2 mm long in the sample. Quartz: 65%; Sulphides: 25%; Phyllosilicates: 9%; Hydrocarbon: 1%.	Sample appears dominantly sedimentary in nature, but it is severely fractured with sulphides concentrated in the fractures and a number of sulphide veinlets	`	Sulphides occur as rounded pyrite (with chalcopyrite. Inclusions) and sphalerite, euhedral grains, interstitial masses of pyrite and a number of veinlets containing mainly pyrite. There is some minor brannerite/coffinite secondary mineralisation. There is a small carbon seam with uraninite grains within, the seam includes some rounded pyrite and grows around others. There are a few grains of gold near the carbon seam within the phyllosilicate matrix
	VR4C OB	Quartzite sample (1-4 mm), grains are sub-angular to angular and the sample contains abundant sulphides. There is a very small concentration of phyllosilicate minerals between quartz grains. Quartz: 65%; Sulphides: 1%; Phyllosilicates: 10%.	Sample appears dominantly sedimentary in nature	Unidentifiable, sample prepared as ore block	There are very few rounded and euhedral pyrites distributed throughout the sample, they occur between the quartz clasts. There is some minor secondary brannerite/coffinite but no visible primary uraninite grains. There is no visible Au or C.
	MGS6513 OB	Quartzite sample (1-4 mm), grains are sub-angular to angular and the sample contains abundant sulphides. There is a very small concentration of phyllosilicate minerals between quartz grains. Quartz: 65%; Sulphides: 25%; Phyllosilicates: 10%.	Sample appears dominantly sedimentary in nature, but it is severely fractured with sulphides concentrated in the fractures and a number of sulphide veinlets	Unidentifiable, sample prepared as ore block	Sulphides occur as rounded pyrite (with chalcopyrite and pentlandite inclusions) and sphalerite, euhedral grains, interstitial masses of pyrite and a number of veinlets containing mainly pyrite. There is some minor brannerite/coffinite secondary mineralisation. There is no visible C or Au.
VCR	VCR1	Large pebble conglomerate (2 - 15 mm), with a quartz (1-2 mm), sulphide (0.5 - 2 mm) and phyllosilicate (<0.2 mm) matrix. Quartz: 75%; Sulphides: 10%; Phyllosilicates: 15%.	Sample appears dominantly sedimentary in nature	Alteration mineral occur in very small proportions in the fine matrix with no discernible separate phases - pyrophyllite : 25%; phlogopite: 5%; sericite: 30%; secondary quartz: 25%; muscovite: 5% and chlorite/chloritoid: 10%.	There are a few rounded and euhedral pyrites distributed throughout the sample, they occur between the quartz clasts. In addition there are a number of anhedral pyrrhotite grains that are interstitial to the quartz and pyrite. Within a large pebble there is a singular grain of Au, which is not rounded and not associated with any mineral besides quartz. There is no visible U or C.
	VCR3	Large pebble conglomerate (2 - 15 mm), with a quartz (1-2 mm), sulphide (0.5 - 2 mm) and phyllosilicate (<0.2 mm) matrix. Quartz: 83%; Sulphides: 2%; Phyllosilicates: 10%.	Sample appears dominantly sedimentary in nature	Alteration mineral occur in very small proportions in the fine matrix with no discernible separate phases - pyrophyllite : 25%; phlogopite: 5%; sericite: 30%; secondary quartz: 25%; muscovite: 5% and chlorite/chloritoid: 10%.	There are very few rounded and euhedral pyrites distributed throughout the sample, they occur between the quartz clasts. In addition there are a number of anhedral pyrrhotite grains that are interstitial to the quartz and pyrite. Within a large pebble there is a singular grain of Au, which is not rounded and not associated with any mineral besides quartz. There is no visible U or C.

Samples on which PIXE was performed are highlighted in blue; Sample used for µCT in Chapter 6 is highlighted in red

C2: Additional Petrography Images

Images in this section show notable features described in Appendix C1

Basal Reef

LGM1 Pyrite-chalcopyrite solid-solution formed interstitial to silicate grains

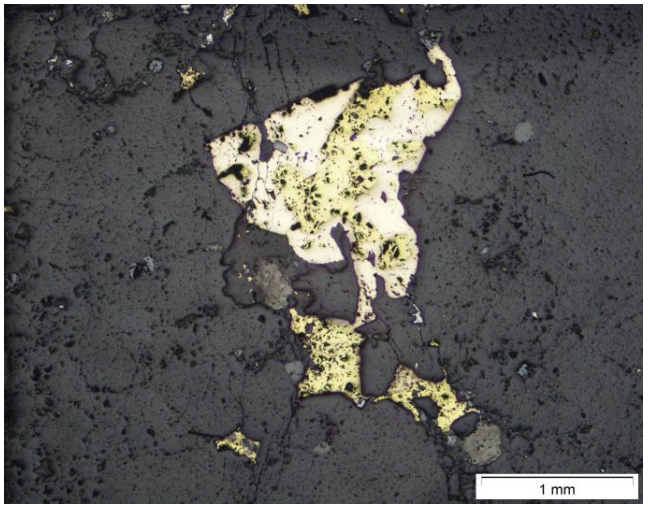

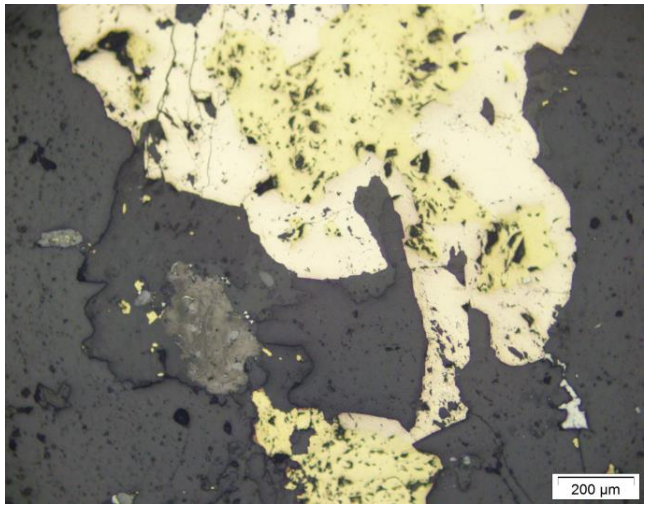

LGM3 Pyrite inclusion in discontinuous carbon seam cut by phyllosilicate matrix with pyrite micrograins

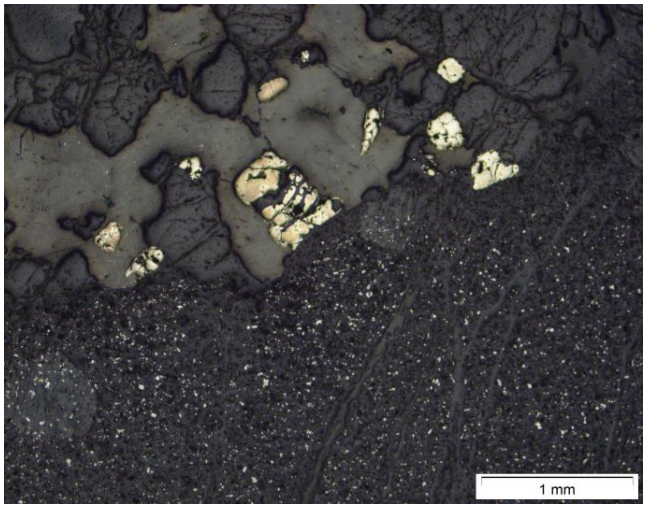

“C” – Reef

CREEF EM2 Fractured pyrite grains with gold surrounding in phyllosilicate matrix

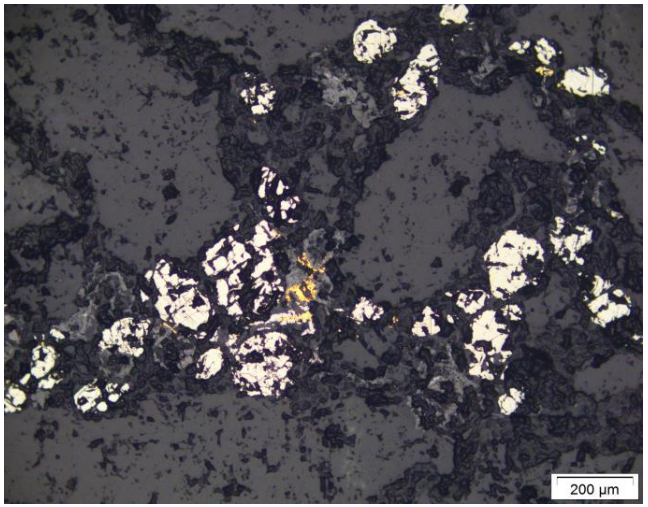

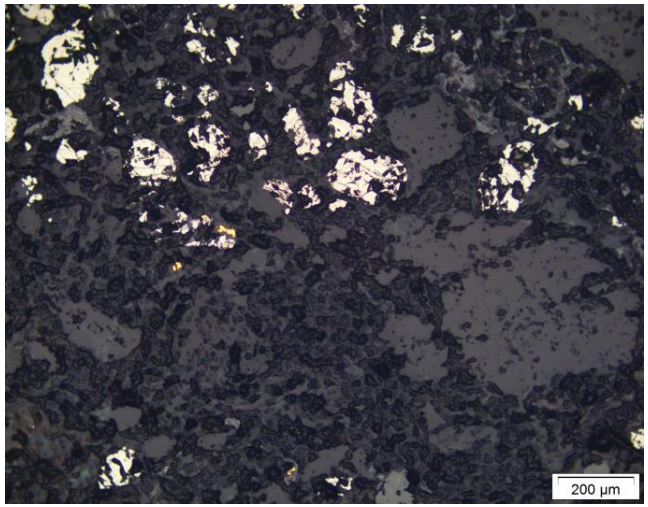

CREEF EM1 section through carbon spindles containing uraninite grains and fragments with abundant inter spindle gold

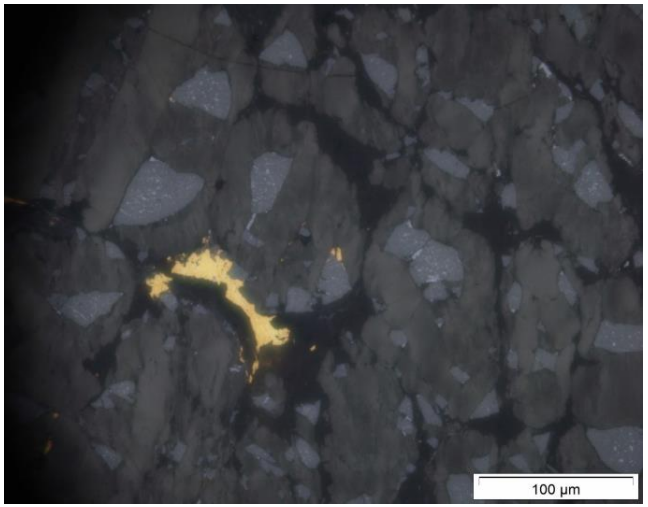

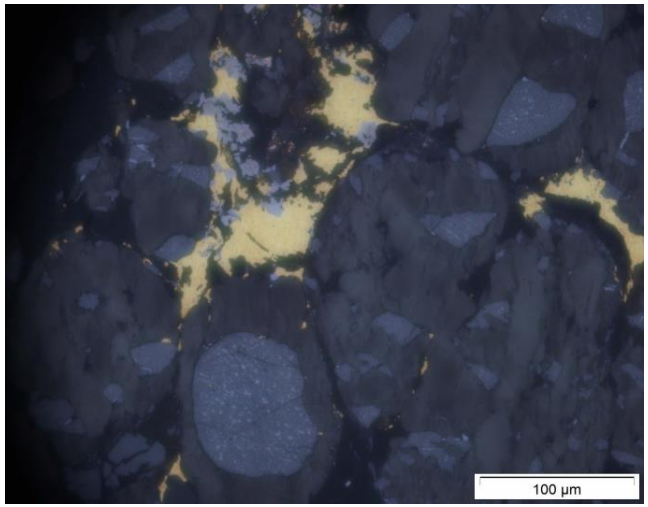

CLR

BVU1 Solid solutions of pyrite and chalcopyrite

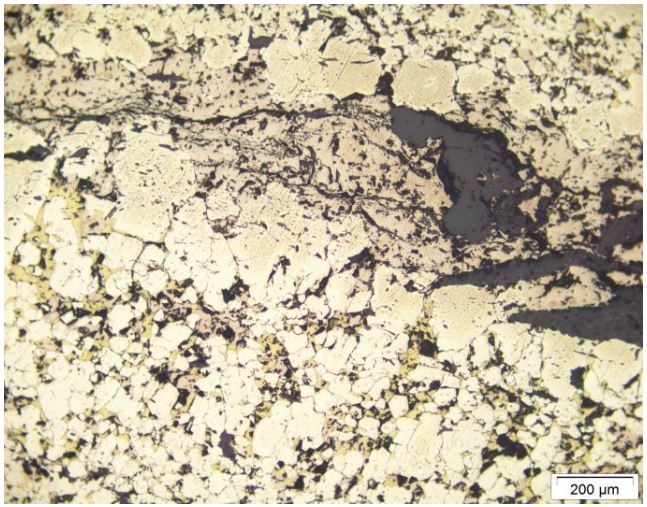

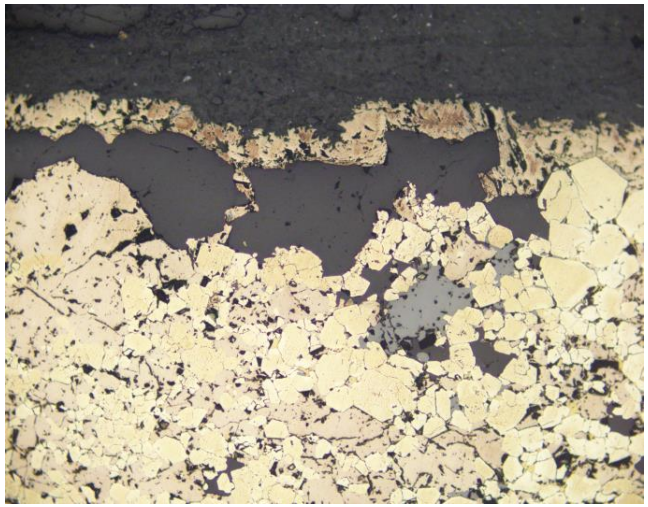

BVU5 Typical rounded pyite, nodular carbon in reef sample, with minor gold in phyllosilicates

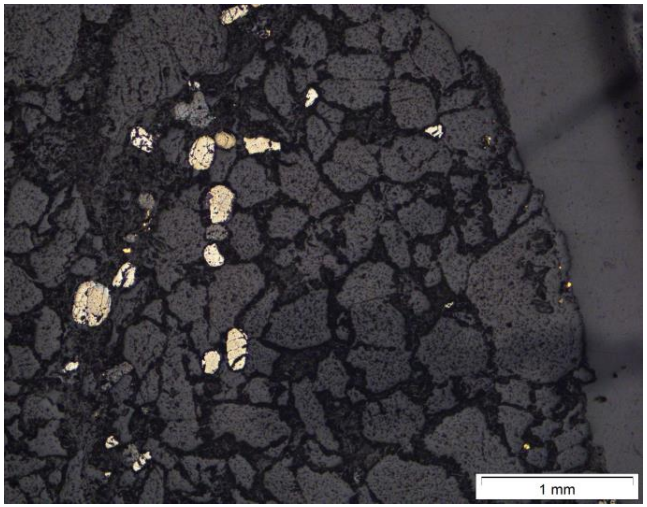

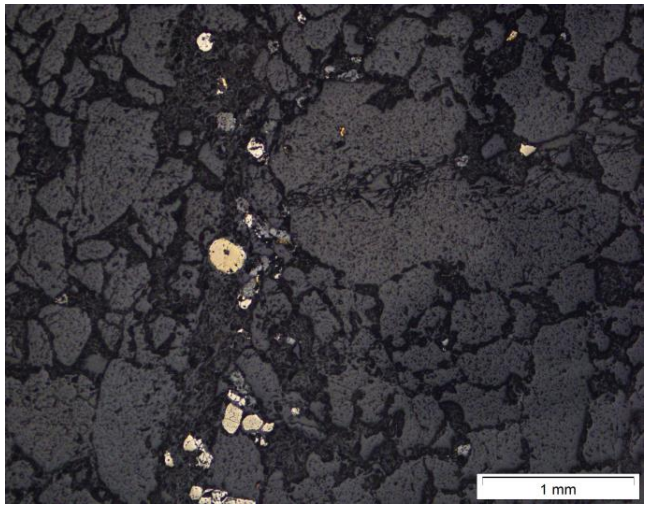

BVU5 Rounded pyrite and carbon nodules in phyllosilicate matrix, with gold contained in a quartz clast

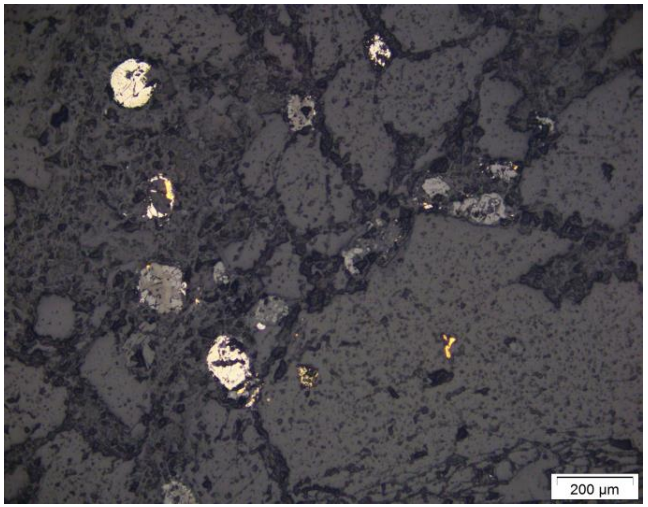

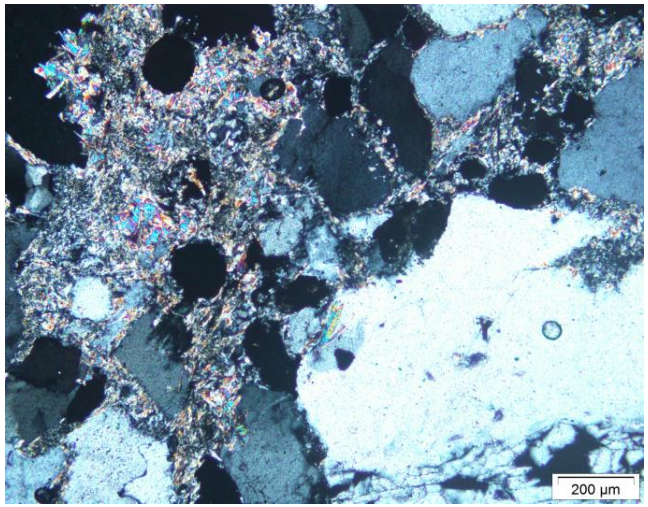

WD20 Irregular carbon nodule within quartz clasts, with gold surrounding pyrite fragment adjacent to the grain

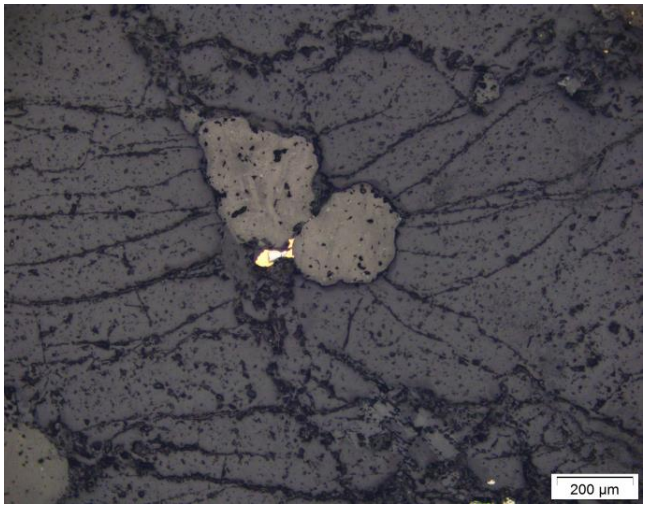

WD20 Concentrically laminated pyrite grain being replaced by globular carbon seam material

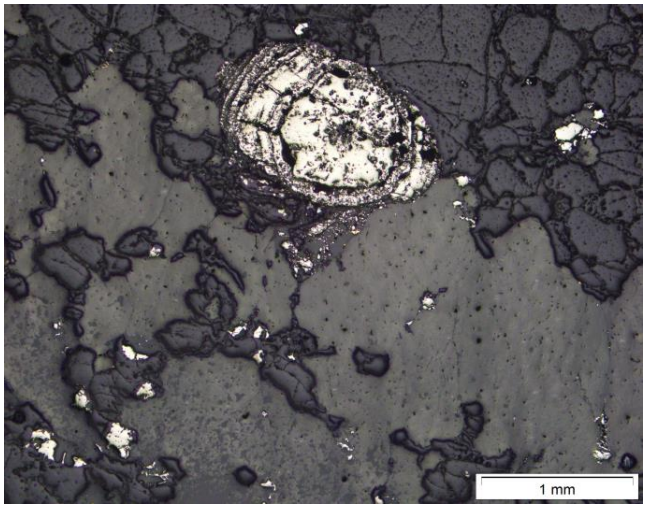

Dominion Reef

BDN2 : Pyrite veinlets and fracture infill

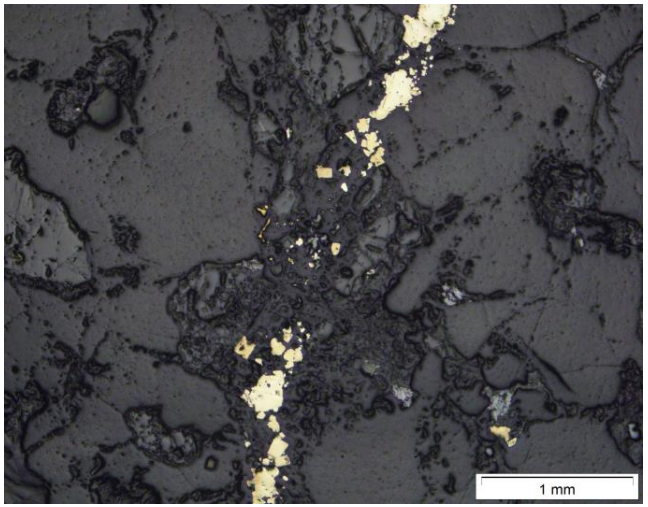

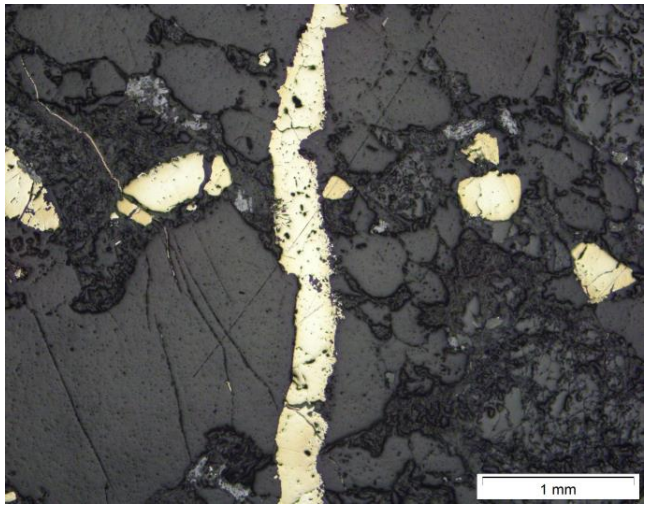

Main Reef Leader

MGS4061 Phyllosilicate materials replacing and cutting through a pyrite grain

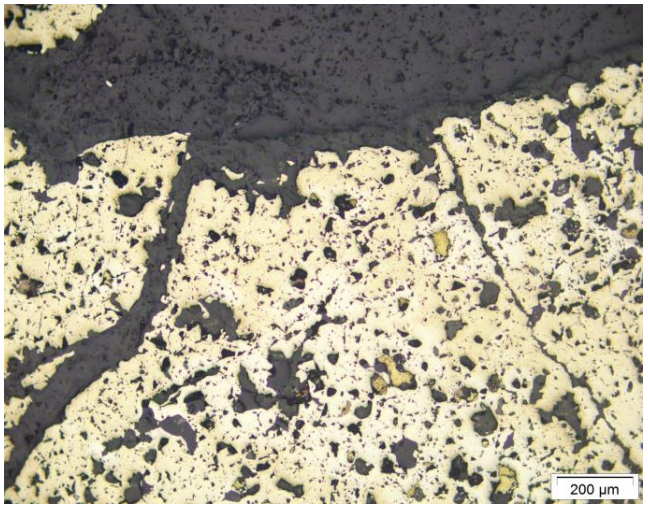

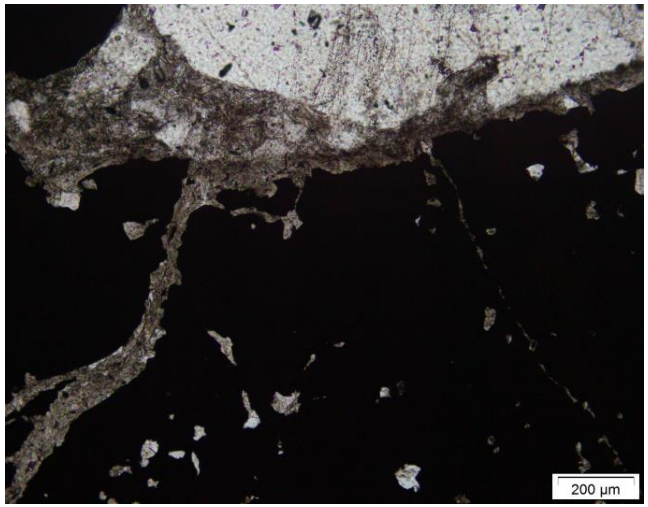

May Reef

MGS4355 Silicate replacement texture in rounded pyrite grains

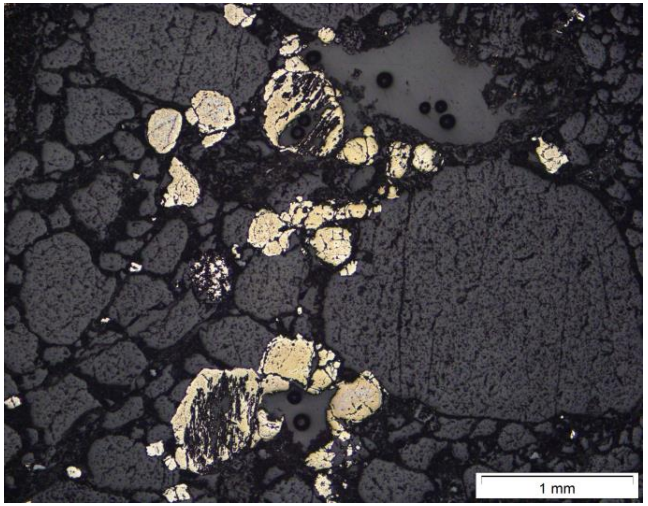

South Reef

EG37 Nodular carbon interstitial to quartz and pyrite grains

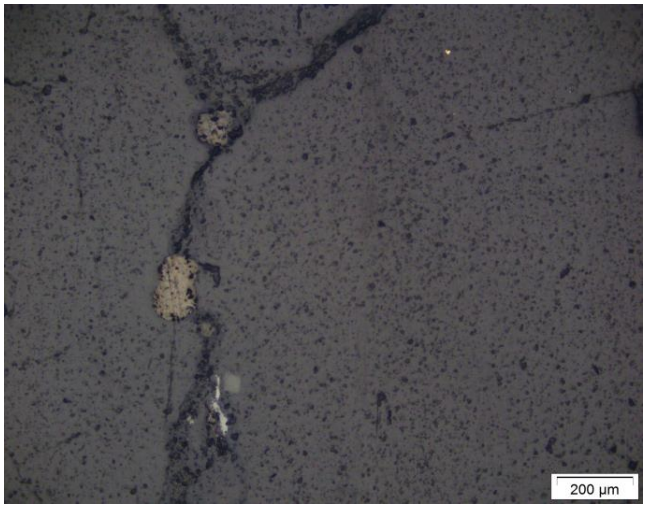

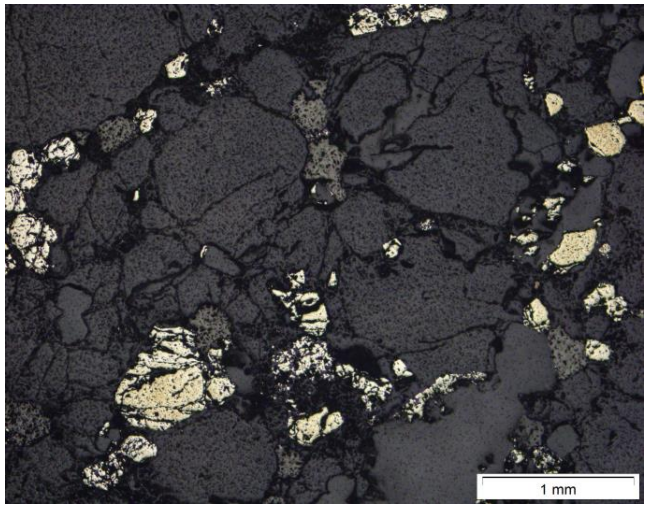

Steyn Reef

PSGM Masses of carbon with no apparent spindle forms but abundant gold

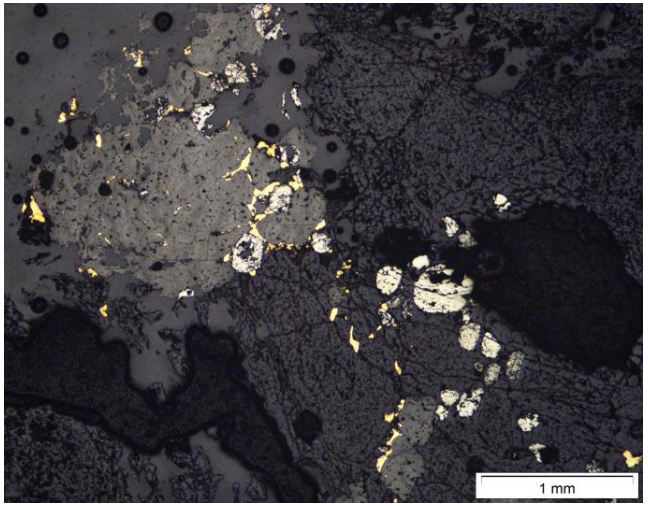

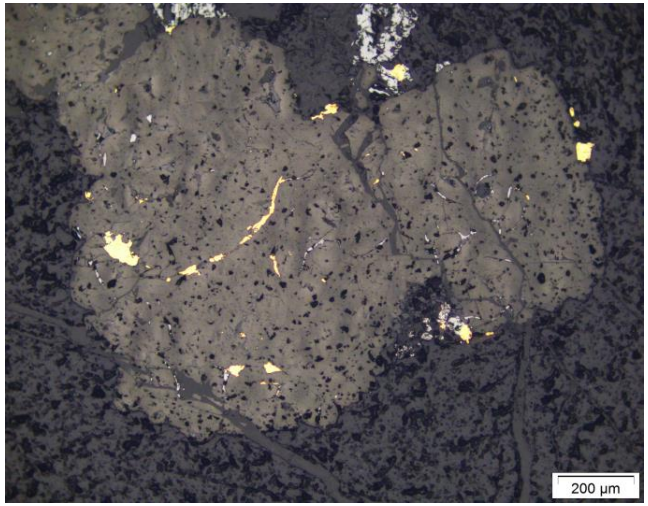

Vaal Reef

MGS6511 Rounded pyrite gains aligned with the samples bedding plane

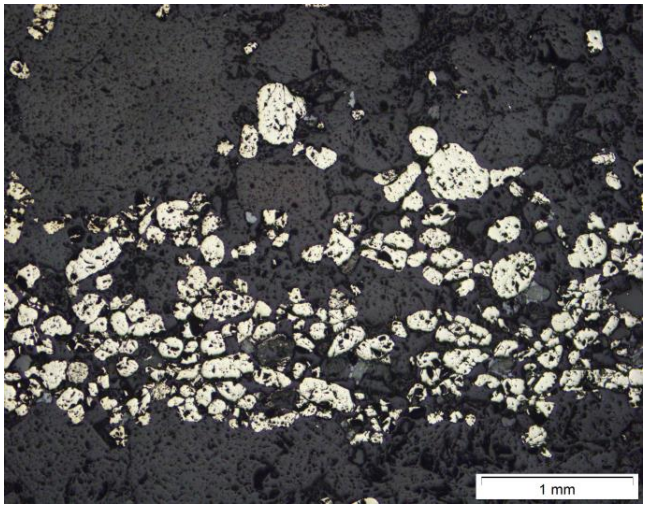

MGS6513 Secondary pyrite between quartz grains

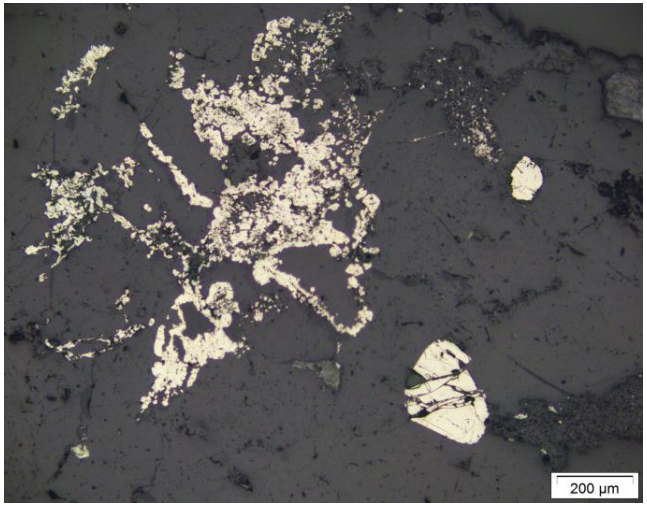

VR4C ore block fragmented uraninite in carbon masses, with gold more abundant around pyrite that in the carbon

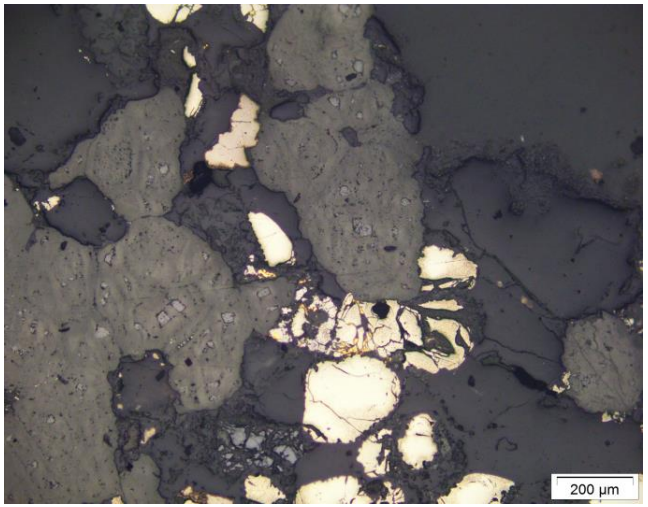

VR4C OB clear carbon spindles containing fragmented uraninite displacing around fragmented pyrite grains

VCR

VCR1 Carbon nodule cut by chlorite with secondary quartz and sericite surrounding the nodule

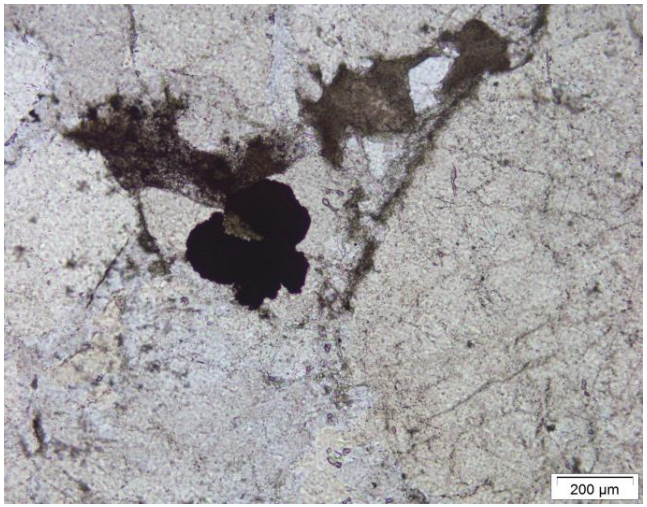

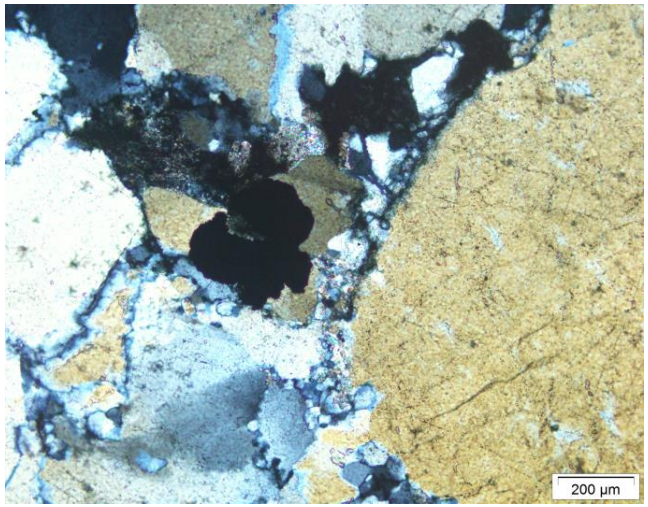

Appendix D: Additional SEM Images

Images in this section show mineral fragments identified as relict uraninite in Chapter 3. However, the features are very fine grained and required SEM EDS spot analyses for confirmation of mineral content and texture. The positions of the spot analyses are noted, with the detected elements for each.

DFN10 -

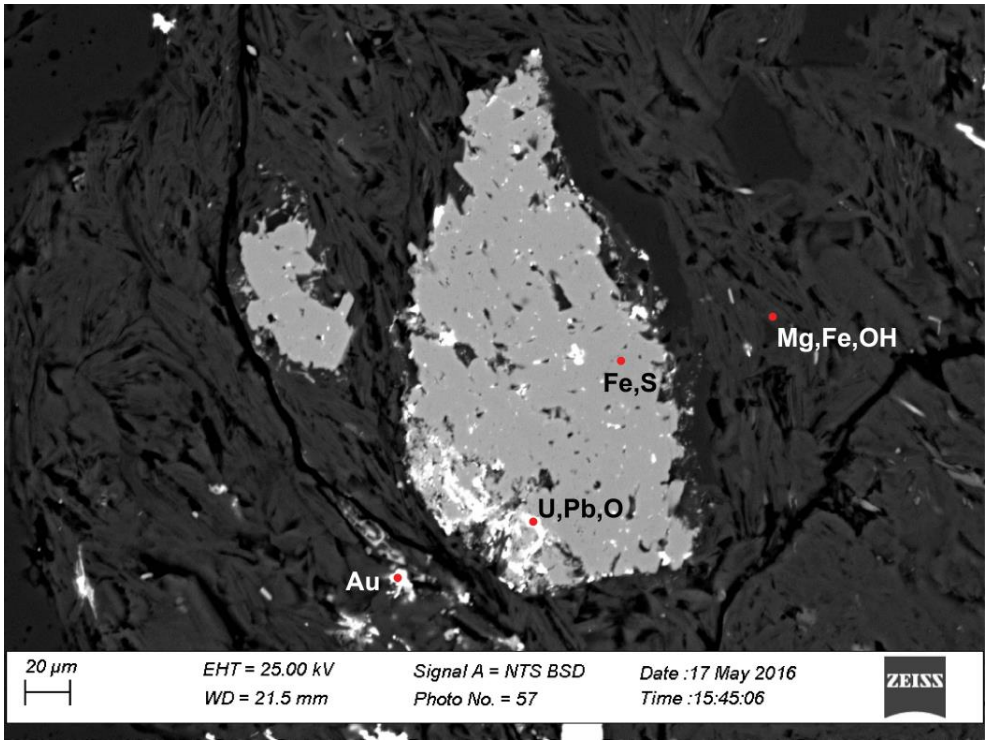

MGS4071

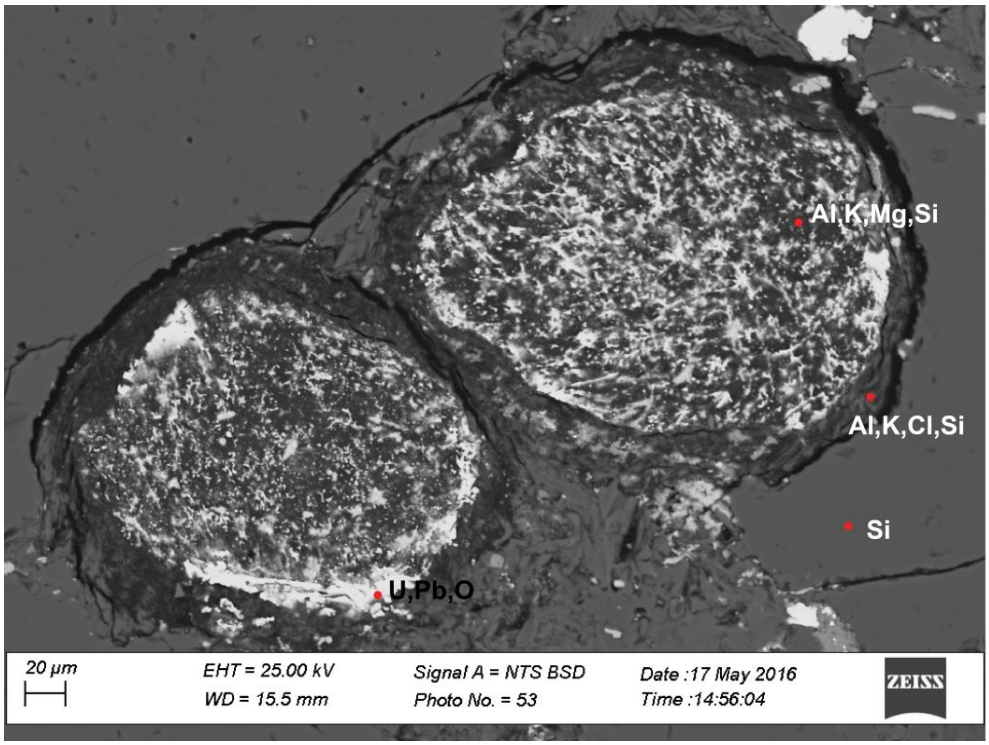
Al,K,Mg,Si
Al,K,Cl,Si
Si
U,Pb,O
20 µm
EHT = 25.00 kV
WD = 15.5 mm
Signal A = NTS BSD
Photo No. = 53
Date :17 May 2016
Time :14:56:04
ZEISS

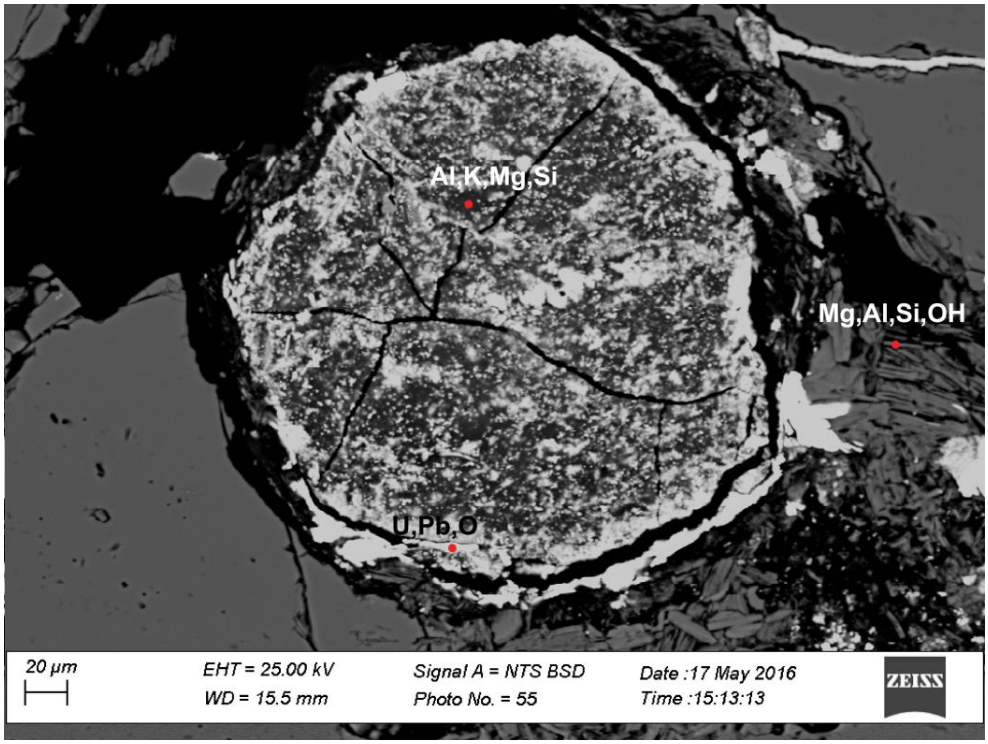
Al,K,Mg,Si
Mg,Al,Si,OH
U,Pb,O
20 µm
EHT = 25.00 kV
WD = 15.5 mm
Signal A = NTS BSD
Photo No. = 55
Date :17 May 2016
Time :15:13:13
ZEISS

Appendix E: PIXE Data from Carbon Seams

CREEF01 Quantitative Analyses and Regions

Light Element Filter Regions

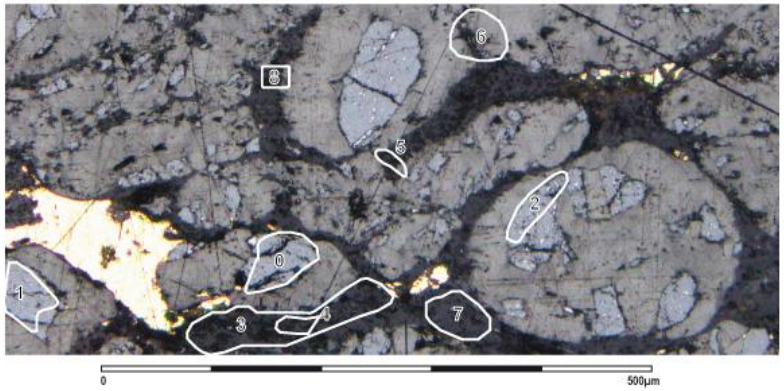

Heavy Element Filter Regions

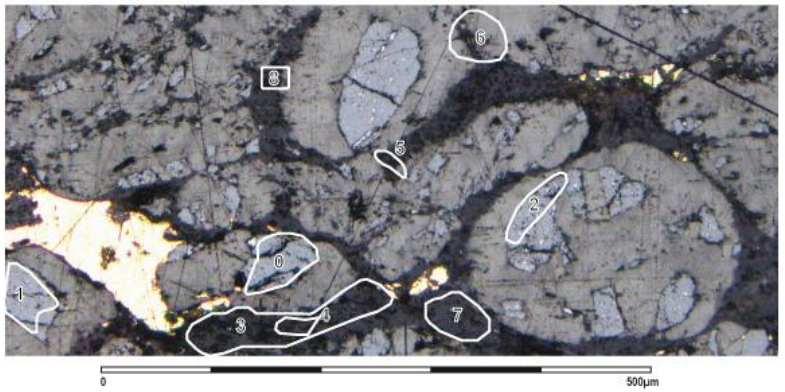

Regions of Interest												
eure_w339_2	Element	*0*	1	2	3	4	5	6	7	8	9	10
Point of interest		U content	U content	U content	Si content	Ti rim	Ti Rim	Cr mineral	K content	Cl content	S content	S content
Light Element Filter	Al %	n.d.	n.d.	n.d.	6.42 ±0.26	6.01 ±0.51	2.80 ±0.92	2.93 ±0.40	6.95 ±0.30	<1.63	<0.89	<0.58
	Si %	n.d.	n.d.	n.d.	5.0 ±0.13	4.0 ±0.13	3.11 ±0.15	2.22 ±0.06	4.92 ±0.18	<0.24	0.25 ±0.05	0.24 ±0.06
	P	n.d.	n.d.	n.d.	n.d.	1400 ±290	<951	2030 ±156	<303	<877	<608	<321
	S	n.d.	n.d.	n.d.	2200 ±58	505 ±149	5600 ±670	4600 ±170	820 ±76	14000 ±860	29000 ±500	28000 ±300
	K	n.d.	n.d.	n.d.	7200 ±160	5400 ±310	7100 ±190	7500 ±110	9000 ±220	460 ±490	210 ±60	640 ±130
	Ca	6000 ±600	6300 ±570	4400 ±420	750 ±30	780 ±50	890 ±70	1300 ±30	500 ±30	2000 ±159	1200 ±38	2200 ±46
	Ti	n.d.	n.d.	n.d.	1400 ±42	4200 ±132	4700 ±190	418 ±31	1800 ±57	<117	<62	<44
	V	n.d.	n.d.	n.d.	n.d.	272 ±123	<159	n.d.	119 ±50	<107	<52	<36
	Cr	<545	<646	<747	359 ±14	219 ±44	260 ±56	332 ±34	530 ±55	<115	<45	<29
	Mn	n.d.	n.d.	n.d.	137 ±14	178 ±63	<134	<79	179 ±22	<131	<45	<32
	CeL	n.d.	n.d.	n.d.	n.d.	n.d.	n.d.	1600 ±159	n.d.	n.d.	n.d.	n.d.

All values in ppm (± Σ uncertainty), unless indicated as wt%. Elements not detected are denoted with n.d.

Regions of Interest												
eure_w339_3	Element	0	1	2	3	4	5	6	7	8	9	10
Point of interest		U content	U content	U content	Cr content	Ti rim	Ti Rim	Cr mineral	Ti content	Ti content	Au content	Ni content
Heavy Element Filter	Fe	2800 ±383	3800 ±419	3000 ±256	3300 ±81	4100 ±105	2000 ±97	3800 ±59	5000 ±110	269 ±44	1500 ±130	6200 ±204
	Ni	575 ±90	634 ±132	597 ±123	216 ±21	<112	<92	<35	101 ±16	<75	n.d.	5100 ±97
	Co	n.d.	n.d.	n.d.	n.d.	n.d.	n.d.	n.d.	n.d.	n.d.	n.d.	985 ±98
	As	6100 ±731	7100 ±1060	0	697 ±46	279 ±90	363 ±176	118 ±94	535 ±58	<204 ±168	n.d.	19000 ±335
	Sr	n.d.	n.d.	n.d.	n.d.	n.d.	n.d.	579 ±55	<198	<404	n.d.	720 ±181
	Y	4400 ±316	2800 ±394	2100±482	4300 ±65	4700 ±283	920 ±188	426 ±53	426 ±163	889 ±185	469 ±41	17000 ±397
	Pd	<596	<598	<893	n.d.	n.d.	n.d.	n.d.	n.d.	n.d.	n.d.	n.d.
	Ag	<628	<562	<989	1400 ±101	n.d.	<1731	<32000	1200 ±165	<1300	22000 ±772	<924
	Cd	<743	<694	<1137	435 ±143	n.d.	n.d.	n.d.	n.d.	n.d.	n.d.	n.d.
	Nd	n.d.	n.d.	n.d.	n.d.	n.d.	n.d.	<1043	<868	<1203	n.d.	n.d.
	YbL	n.d.	n.d.	n.d.	n.d.	<313	<273	n.d.	n.d.	n.d.	n.d.	167 ±273
	AuL	5300 ±253	1760 ±192	<623	18600 ±259	<190	16300 ±349	<74	17700 ±197	<243	363000 ±3685	125 ±179
	HgL	<473	<538	<644	n.d.	n.d.	n.d.	219 ±39	<193	n.d.	5700 ±364	n.d.
	PbL %	12.14 ±0.15	13.75 ±0.19	16.73 ±0.45	1.5 ±0.02	0.58 ±0.02	1.48 ±0.05	0.72 ±0.02	1.6 ±0.03	3.05 ±0.06	0.23 ±0.02	0.08 ±0.02
	ThL %	1.56 ±0.09	1.79 ±0.12	2.88 ±0.18	0.11 ±0.01	<0.05	0.13 ±0.03	0.1 ±0.01	0.08 ±0.02	<0.08	n.d.	0.05±0.05
	UL %	30.95 ±0.33	28.51 ±0.34	30.92 ±0.44	3.24 ±0.07	1.2 ±0.04	4.47 ±0.1	0.97 ±0.02	3.63 ±0.09	8.42 ±0.34	0.58 ±0.04	0.20 ±0.05

All values in ppm (± Σ uncertainty), unless indicated as wt%. Elements not detected are denoted with n.d.

DFN10 Quantitative Analyses and Regions

Light Element Filter Regions

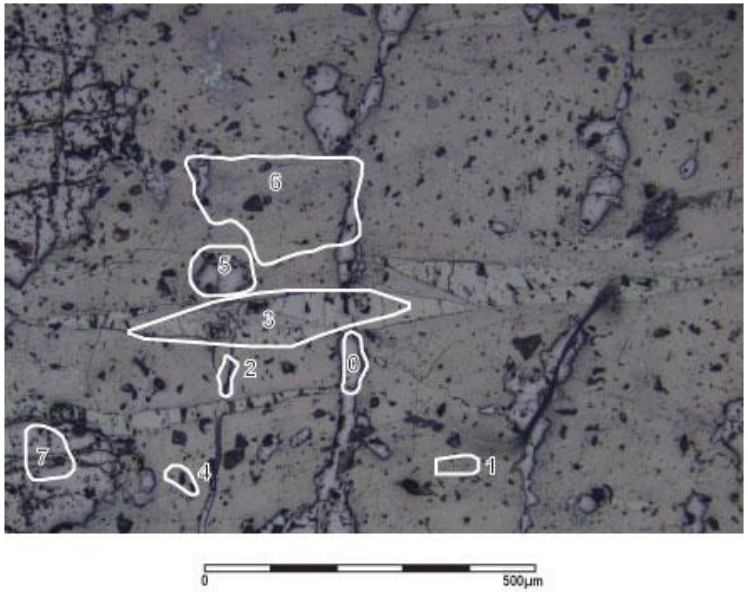

Heavy Element Filter Regions

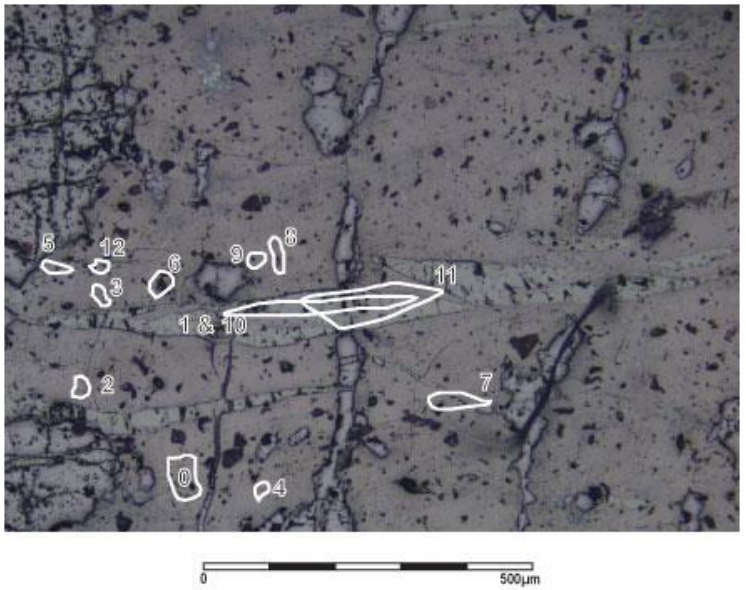

Regions of Interest									
wood_w351_19	Element	0	1	2	3	4	5	6	7
Point of interest		Si content	S content	Cl content	Ca content	Ti content	Si content	S content	Cr content
Light Element Filter	Al	<0.78	<2.47	n.d.	n.d.	n.d.	1.13 ±0.3	<0.2	n.d.
	Si %	20.62 ±0.2	5.12 ±0.29	0.26 ±0.09	0.06 ±0.02	0.48 ±0.11	24.22 ±0.14	1.34 ±0.1	19.96 ±0.31
	P	n.d.	1800 ±502	<717	<163	<959	<174	278 ±54	n.d.
	S	1400 ±116	14000 ±1090	2600 ±196	<82	3400 ±236	308 ±29	4600 ±188	<113
	K	511 ±62	<671	3400 ±180	<65	<443	136 ±25	596 ±39	131 ±32
	Ca	665 ±57	787 ±121	1000 ±86	<62	823 ±193	317 ±46	677 ±26	95 ±28
	Ti	4400 ±133	5500 ±224	5500 ±193	52000 ±334	4000 ±152	533 ±33	4500 ±68	11300 ±165
	V	126 ±19	<183	133 ±37	n.d.	5400 ±196	104 ±12	611 ±14	n.d.
	Cr	<54	<158	n.d.	n.d.	221 ±153	<34	<15	n.d.
	Mn	<54	<157	n.d.	n.d.	n.d.	n.d.	n.d.	n.d.
	CeL	<57	<190	n.d.	118 ±12	<125	<29	<15	n.d.

All values in ppm (± Σ uncertainty), unless indicated as wt%. Elements not detected are denoted with n.d.

Regions of Interest														
wood_w351_20	Element	0	1	2	3	4	5	6	7	8	9	10	11	12
Point of interest		Ti content	Mn content	Fe content	Co content	Y content	Zr content	Au content	Hg content	Pb content	U content	Mn content	Ca content	Cu content
Heavy Element Filter	Fe	279 ±34	853 ±25	13200±258	953 ±111	202 ±62	336 ±59	649 ±64	278 ±64	191 ±30	263 ±56	801 ±21	387 ±10	5400±175
	Co	n.d.	n.d.	n.d.	1800 ±120	<137	<128	960 ±61	0	<57	<105	<15	<6	n.d.
	Ni	n.d.	n.d.	n.d.	2200±127	<161	<147	1300 ±93	<75	<69	<127	<16	<7	494 ±51
	Cu	n.d.	n.d.	n.d.	n.d.	n.d.	n.d.	n.d.	n.d.	n.d.	n.d.	n.d.	n.d.	5200 ±134
	Ga	n.d.	<18	<91	<225	<119	<85	n.d.	n.d.	n.d.	n.d.	n.d.	n.d.	n.d.
	As	375 ±56	157 ±14	418 ±105	7800±199	475 ±202	197 ±97	4500 ±175	489 ±70	<162	<256	166 ±13	196 ±5	163 ±34
	Sr	<202	192 ±19	<273	<525	<487	<394	<462	<370	<246	<555	176 ±15	161 ±7	n.d.
	Y	2100 ±137	72 ±17	587 ±166	963 ±153	4400 ±345	3400 ±257	1460 ±151	<311	1400± 228	1200 ±311	69 ±12	49 ±5	<371
	Zr	<379	<78	<633	631 ±194	<1130	2500 ±312	1000 ±167	<317	<481	<1270	<57	<23	n.d.
	Ag	<1278	<281	<1916	19000 ±1312	0	<2555	25000 ±1311	<1924	<1300	0	<195	<47	n.d.
	Gd L	<471	n.d.	n.d.	n.d.	n.d.	n.d.	n.d.	n.d.	n.d.	n.d.	n.d.	n.d.	n.d.
	Au L	<140	<35	2080 ±130	106000 ±1240	<337	<207	135000 ±2479	<390	<167	<333	<31	<15	n.d.
	Hg L	n.d.	n.d.	n.d.	1020 ±348	<367	<220	1800 ±380	57000 ±696	<192	<385	<34	<16	n.d.
	Pb L	1200 ±122	133 ±26	4100 ±251	<788	5900 ±536	990 ±200	<706	<381	23000 ±369	16000 ±552	115 ±21	124 ±9	n.d.
	Th L	656 ±133	<78	2100 ±258	922 ±282	2100 ±388	2300 ±308	835 ±242	<500	1400 ±211	3500 ±506	61 ±20	29 ±9	n.d.
	U L %	2.54 ±0.09	0.14 ±0.01	3.04 ±0.08	1.94 ±0.08	5.57 ±0.12	5.46 ±0.14	2.46 ±0.1	0.35 ±0.03	2.03 ±0.05	9.02 ±0.2	0.12 ±0	0.09 ±0	0.23 ±0.02

All values in ppm (± Σ uncertainty), unless indicated as wt%. Elements not detected are denoted with n.d.

S3: LGM3 Quantitative Analyses and Regions

Light Element Filter Regions

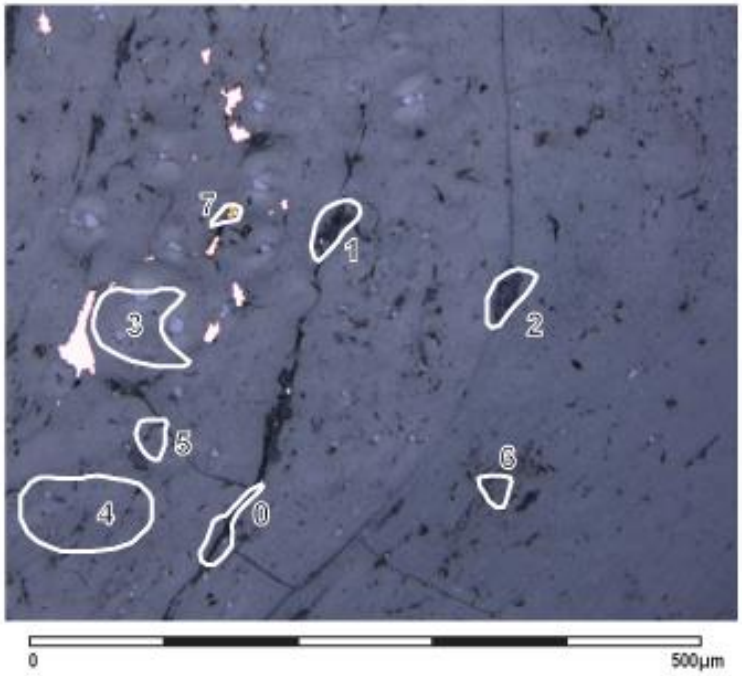

Heavy Element Filter Regions

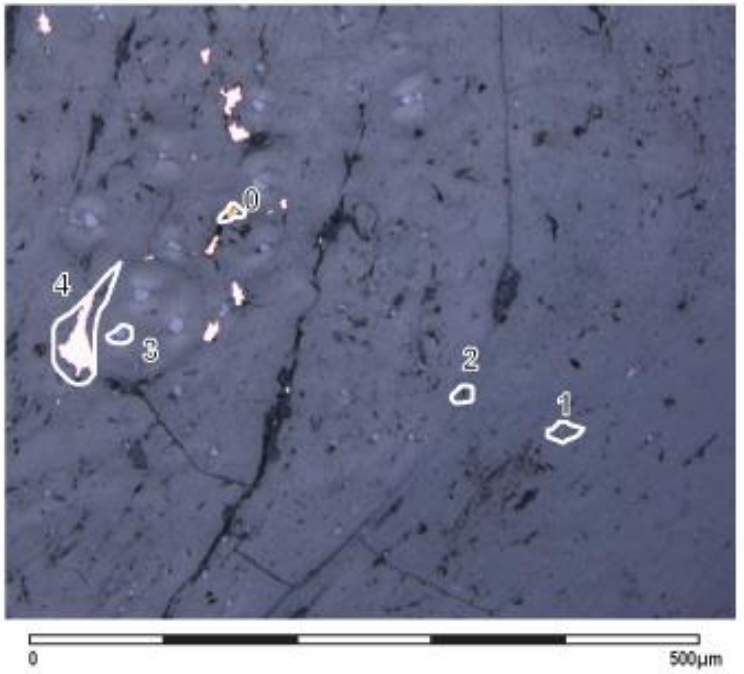

Regions of Interest									
wood_w351_26	Element	0	1	2	3	4	5	6	7
Point of interest		Al content	Si content	S content	Cl content	K content	Ca content	Ti content	Fe content
Light Element Filter	Al %	4.72 ±0.53	3.4 ±0.31	0	0.4 ±0.09	0.35 ±0.09	n.d.	1.41 ±0.33	4.09 ±0.5
	Si %	5.34 ±0.16	12.91 ±0.34	1.33 ±0.09	0.32 ±0.02	3.09 ±0.17	2.15 ±0.13	1.21 ±0.08	4.26 ±0.18
	P	n.d.	n.d.	n.d.	n.d.	n.d.	14600 ±1194	n.d.	1000 ±234
	S	1700 ±159	1800 ±134	7600 ±687	6000 ±227	3700 ±79	1200 ±126	5500 ±457	1300 ±188
	Cl	1400 ±105	291 ±56	834 ±93	2700 ±51	1240 ±57	466 ±90	<315	547 ±117
	K	1300 ±60	731 ±70	850 ±108	698 ±41	1300 ±30	1000 ±137	598 ±265	1100 ±84
	Ca	8700 ±253	5400 ±163	6000 ±156	4800 ±108	8900 ±165	29000 ±382	5100 ±110	10000 ±272
	Ti	<58	1600 ±47	135 ±21	<28	100 ±8	n.d.	6700 ±136	<77
	V	<54	64 ±26	<45	<23	<19	n.d.	<114	<69
	Cr	<47	80 ±24	<44	<19	<18	n.d.	<89	<67
	Mn	<51	<56	<46	<21	<19	n.d.	<100	<79

All values in ppm (± Σ uncertainty), unless indicated as wt%. Elements not detected are denoted with n.d.

Regions of Interest						
wood_w351_27	Element	0	1	2	3	4
Point of interest		Fe content	Ni content	Cu content	Y content	Au content
Heavy Element Filter	Fe	2600 ±176	322 ±87	2800 ±269	277 ±108	272 ±39
	Co	<127	<196	<175	<177	<86
	Ni	<113	1150 ±100	<211	<225	<115
	Cu	0	0	2300 ±173	<228	<121
	As	791 ±132	2800 ±255	736 ±202	<695	563 ±146
	Sr	<476	<563	<883	<1323	<295
	Y	<589	1300 ±309	<1100	4500 ±694	<210
	Ag	<4405	<5205	<8180	0	29000 ±2000
	Ba	<49000	<58000	0	0	<15000
	La	<64000	<76000	0	0	<19000
	Au L	3700 ±289	<419	<642	<883	340000 ±21000
	Hg L	<415	<464	<710	<985	6200 ±733
	Pb L	1600 ±280	6200 ±495	3400 ±455	57000 ±1500	<606
	Th L	<736	<1000	<1200	7800 ±1000	<637
	U L	5100 ±506	17000 ±879	<1406	191000 ±5309	3300 ±980

All values in ppm (± Σ uncertainty), unless indicated as wt%. Elements not detected are denoted with n.d.

S4: MGS6512 Quantitative Analyses and Regions

Light Element Filter Regions

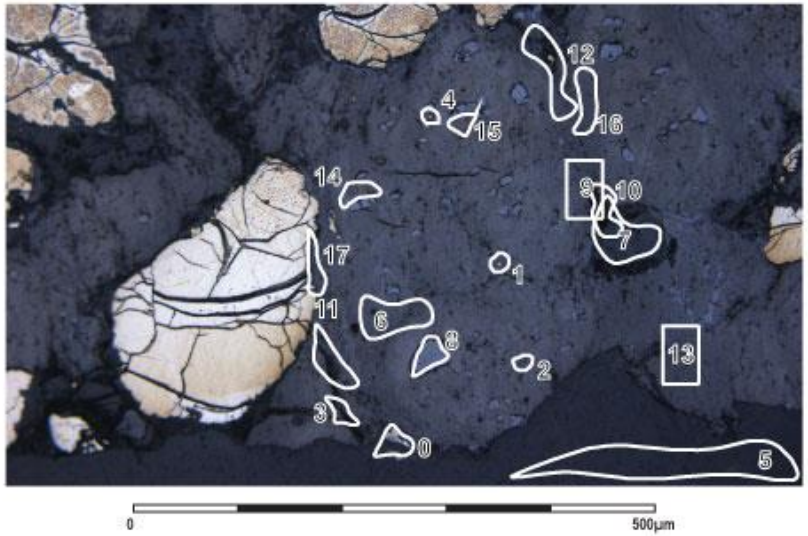

Heavy Element Filter Regions

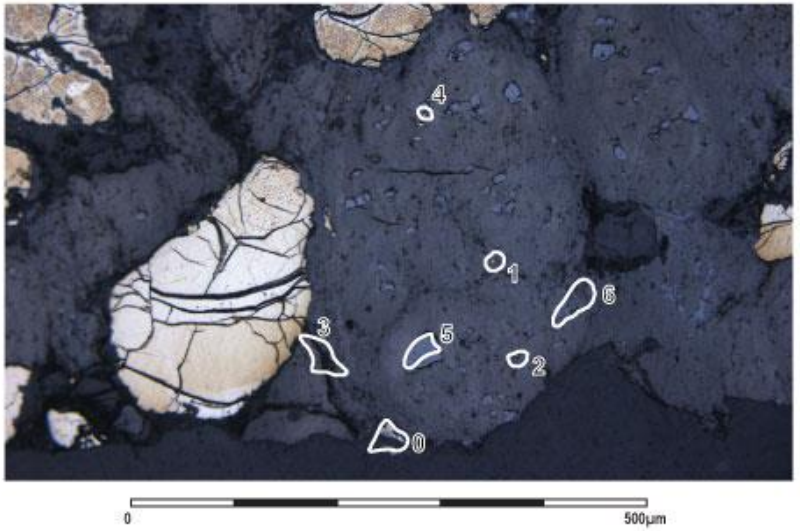

Regions of Interest										
wood_w351_43	Element	0	1	2	3	4	5	6	7	8
Point of interest		Fe content	Cu content	Zn content	Y content	Au rim	Cl Rim	S mineral	K content	Ca content
Light Element Filter	Al %	<0.7	<2.25	<2.19	<0.88	<2.16	0	<0.48	5.37 ±0.58	<0.84
	Si %	0.67 ±0.09	0.7 ±0.14	0.72 ±0.11	0.46 ±0.07	<0.32	<0.03	0.37 ±0.06	5.12 ±0.25	<0.11
	P	1700 ±460	2900 ±674	<1131	5000 ±959	<1180	<121	1500 ±422	<258	662 ±257
	S %	4.17 ±0.11	3.14 ±0.14	0.57 ±0.04	1.23 ±0.04	2.12 ±0.12	0.03 ±0.01	3.12 ±0.03	0.16 ±0.01	1.3 ±0.08
	Cl	<113	<435	618 ±224	<175	<457	7800 ±125	<92	<116	<165
	K	200 ±90	302 ±358	1200 ±388	173 ±367	<378	<28	687 ±102	12000 ±305	546 ±487
	Ca	139 ±25	232 ±57	507 ±69	753 ±82	414 ±64	34 ±6	196 ±12	310 ±23	944 ±126
	Ti	1700 ±60	795 ±78	14000 ±277	205 ±39	<144	<15	2200 ±43	9400 ±111	258 ±34
	V	<48	<178	337 ±182	<71	<134	<13	75 ±19	612 ±103	<55
	Cr	56 ±16	<189	269 ±70	<82	<151	<11	96 ±12	932 ±59	<65
	Mn	<86	<234	<238	<105	191 ±65	<10	80 ±12	392 ±39	371 ±28

All values in ppm (± Σ uncertainty), unless indicated as wt%. Elements not detected are denoted with n.d.

Regions of Interest										
wood_w351_43	Element	9	10	11	12	13	14	15	16	17
Point of interest		Al content	Si content	P content	Ti content	Ti rim	Ca Rim	Ca mineral	Ca content	Ca content
Light Element Filter	Al %	4.55 ±0.38	3.24 ±0.38	<0.36	0.72 ±0.26	<0.1	<1.03	<1.04	<0.56	<0.72
	Si %	5.54 ±0.3	8.28 ±0.27	0.83 ±0.05	2.04 ±0.05	0.51 ±0.02	<0.14	<0.14	2.19 ±0.1	1.12 ±0.06
	P	<144	<282	4500 ±525	2000 ±256	1100 ±270	599 ±206	798 ±238	2000 ±276	5300 ±829
	S	0.03 ±0	0.29 ±0.01	1.38 ±0.02	1.61 ±0.03	1.95 ±0.04	1.69 ±0.05	2.21 ±0.1	1.51 ±0.05	1.4 ±0.08
	Cl	<67	<114	<71	n.d.	517 ±89	<199	<206	<100	<137
	K	6091 ±178	6000 ±186	667 ±311	n.d.	765 ±199	178 ±426	<436	2300 ±209	436 ±434
	Ca	145 ±13	423 ±45	694 ±48	744 ±124	389 ±31	629 ±73	831 ±87	766 ±34	962 ±71
	Ti	4100 ±45	10000 ±138	592 ±22	11400 ±186	2300 ±28	96 ±23	<68	12000 ±196	616 ±35
	V	366 ±73	655 ±84	<30	335 ±80	68 ±18	<71	<69	585 ±124	<55
	Cr	1521 ±49	735 ±34	40 ±30	266 ±18	96 ±7	<79	n.d.	n.d.	n.d.
	Mn	389 ±30	183 ±27	62 ±29	99 ±26	125 ±16	296 ±36	467 ±39	<69	96 ±72

All values in ppm (± Σ uncertainty), unless indicated as wt%. Elements not detected are denoted with n.d.

Regions of Interest								
wood_w351_44	Element	0	1	2	3	4	5	6
Point of interest		Fe content	Cu content	Zn content	Y content	Au rim	Pb Rim	Pb mineral
Heavy Element Filter	Fe	18.2 ±0.4	2.17 ±0.05	0.24 ±0.03	0.02 ±0.01	0.05 ±0.01	0.08 ±0.01	0.39 ±0.01
	Ni	247 ±24	<357	<352	<191	<182	<116	<69
	Cu	920 ±54	21000 ±366	<368	<170	0	0	<68
	Zn	<79	<376	26000 ±601	<131	<295	<133	<85
	Y	1400 ±80	2800 ±557	5200 ±612	2600 ±629	2000 ±436	8500 ±573	4200 ±356
	Ag	<550	0	<5900	<931	<5900	<785	<377
	Ce	<10000	<93000	<11000	n.d.	n.d.	n.d.	n.d.
	Ce L	<8100	<14000	<12000	n.d.	n.d.	n.d.	n.d.
	Nd	<19000	<18000	<203000	n.d.	n.d.	n.d.	n.d.
	Nd L	<2900	<5000	<4500	<2100	n.d.	n.d.	n.d.
	Dy L	n.d.	n.d.	n.d.	2200 ±189	n.d.	n.d.	n.d.
	Er L	n.d.	n.d.	n.d.	865 ±198	n.d.	n.d.	n.d.
	Yb L	n.d.	n.d.	n.d.	1000 ±196	n.d.	n.d.	n.d.
	Au L	<140	<596	<1109	<312	26000 ±958	<325	<193
	Pb L %	0.55 ±0.02	3.6 ±0.08	3.31 ±0.08	3.42 ±0.05	2.98 ±0.09	9.45 ±0.26	12.49 ±0.18
	Th L %	0.16 ±0.01	0.78 ±0.11	0.99 ±0.12	2.32 ±0.07	0.39 ±0.07	0.84 ±0.12	1 ±0.06
	U L %	1.31 ±0.04	7.7 ±0.24	8.44 ±0.21	11.97 ±0.19	8.94 ±0.22	32.4 ±0.61	4.68 ±0.07

All values in ppm (± Σ uncertainty), unless indicated as wt%. Elements not detected are denoted with n.d.

Appendix E: PIXE Data from Carbon Seams

PSGM Carbon Nodule Quantitative Analyses and Regions

Heavy Element Filter Regions

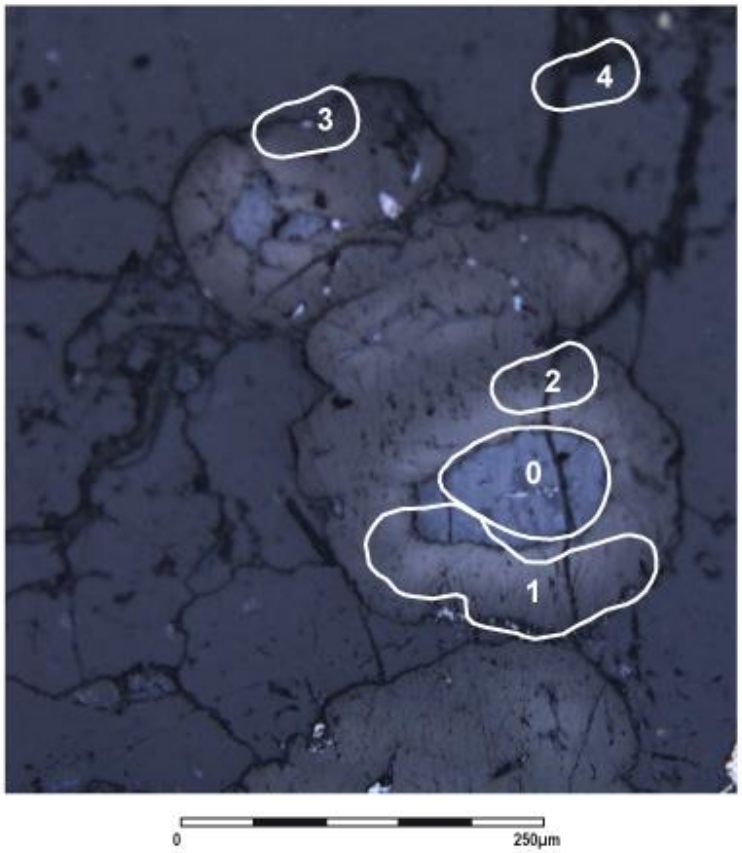

Regions of Interest						
wood_w351_9	Elements	0	1	2	3	4
Point of interest		U content	As content	As content	Au content	Au content
Hea±y Element Filter	Ti	<777	571±133	<471	<525	947±379
	Cr	<100	<39	<68	<68	145±37
	Mn	286±41	<25	<46	<43	104±25
	Fe	356±30	1299±25	924±37	305±19	4265±60
	Co	<31	1918±17	579±32	141±12	925±29
	Ni	40±11	610±9	177±15	39±8	297±16
	Cu	<33	20±3	<26	n.d.	n.d.
	Zn	<30	<11	<23	n.d.	n.d.
	As	<208.±208	5863±43	3407±82	1061±72	2779±46
	Y	2973±222	79±14	<101	n.d.	593±49
	Zr	n.d.	66±15	<123	n.d.	875±79
	Ag	<208	<81	<352	821±97	<382
	Sb	n.d.	<237	n.d.	n.d.	n.d.
	Ce	<2344	<1491	<6444	n.d.	n.d.
	Ce L	<1709	<681	<1218	n.d.	n.d.
	Au L	<106	<32	<61	6000±128	1831±54
	Pb L	33308±529	1948±62	3090±127	25304±240	325±45
	Th L	22301±524	366±22	<156	343±74	3100±102
	U L %	23.8722	0.3386	0.341	0.9357	1.8658

All values in ppm (± Σ uncertainty), unless indicated as wt%. Elements not detected are denoted with n.d.

CREEFEM4 Quantitative Analyses and Regions

Light Element Filter Regions

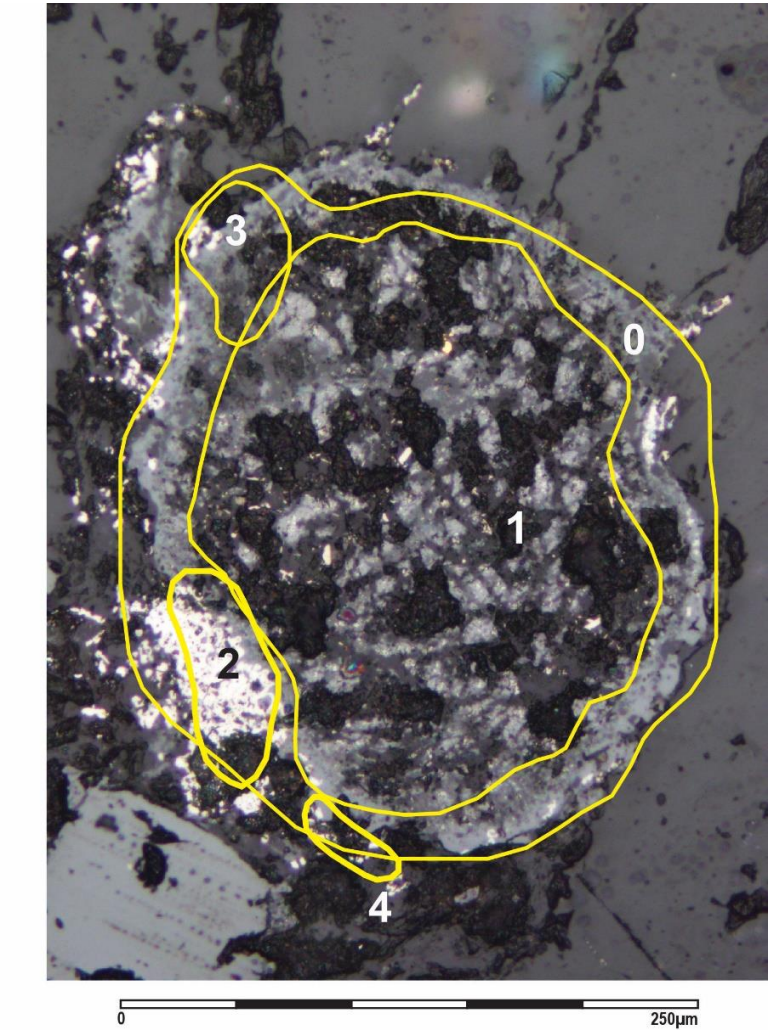

Heavy Element Filter Regions

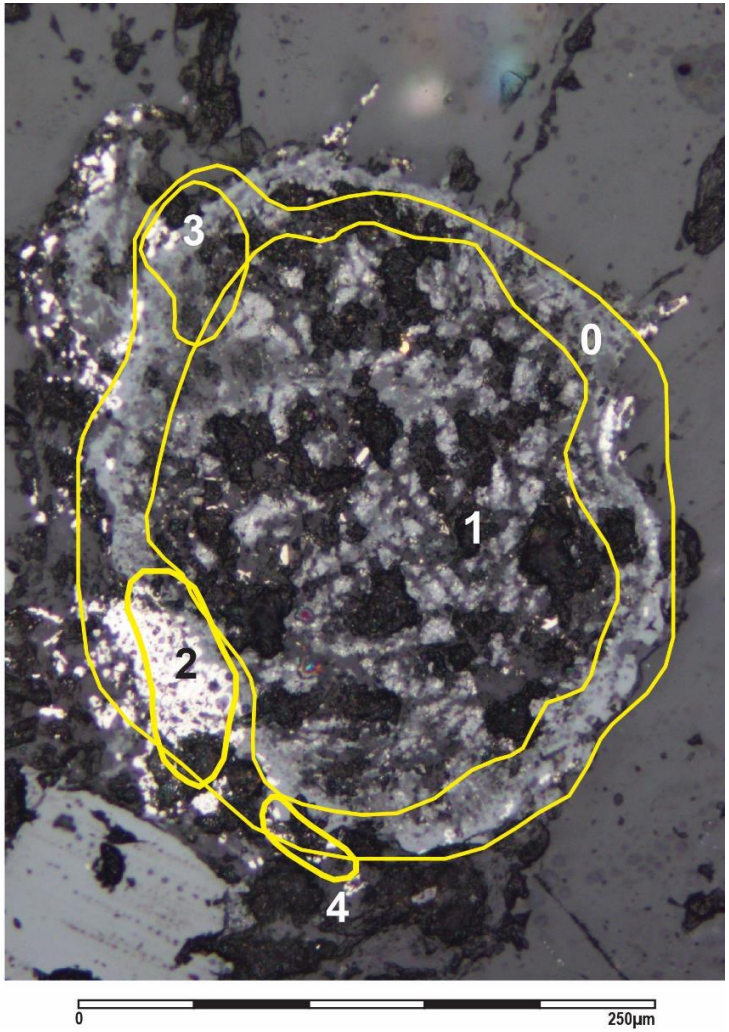

Regions of Interest						
wood_w351_13	Element	0	1	2	3	4
Point of interest		Ti content	U content	As content	Ti content	Ti content
Light Element Filter	Al %	2.12v0.16	1.91v0.12	0.75v0.03	1.63v0.08	1.08v0.09
	Si %	5.3v0.01	2.09v0.02	0.89v0.01	1.44v0.01	1.11v0.01
	P	936±83	1412±161	274±81	1238±79	660±114
	S	3514±70	3827±64	13040±1072	3316±145	3828±238
	Cl	<37	<55	<60	<90	<176
	K	1749±280	561±352	1077±64	2508±389	1287±480
	Ca	521±36	739±59	131±25	634±44	563±84
	Ti	3230±30	2909±29	2140±35	14790±322	18114±332
	Cr	214±8	87±13	498±16	572±23	1040±41
	Mn	29±10	49±9	<46	<60	141±32

All values in ppm (± Σ uncertainty), unless indicated as wt%. Elements not detected are denoted with n.d.

Regions of Interest						
wood_w351_12	Element	0	1	2	3	4
Point of interest		Ti content	As content	Ti content	Ti content	Ti content
Heavy Element Filter	Fe	7402±114	7008±152	28431±474	6505±135	5179±226
	Co	1424±41	217±48	12032±173	2564±71	2008±69
	Ni	8685±130	876±36	80680±1053	19358±428	11822±263
	As	19860±225	1919±257	186017±1572	51321±322	31363±380
	Sr	840±40	1105±56	<125	2404±128	1317±125
	Y	6481±190	9331±261	312±54	3259±222	4387±372
	Ag	92±29	<71	<326	<355	<791
	Sb	n.d.	n.d.	1262±195	<726	<2302
	Ba	478±88	<477	n.d.	n.d.	n.d.
	Ba L	<1328	<1675	n.d.	n.d.	n.d.
	La	1190±120	1272±171	n.d.	n.d.	n.d.
	La L	<809	<1025	n.d.	n.d.	n.d.
	Ce	1836±141	2046±194	n.d.	<4557	<14463
	Ce L	<485	<617	n.d.	<3004	<5295
	Nd	1138±170	1334±246	n.d.	n.d.	n.d.
	Nd L	350±184	692±293	n.d.	n.d.	n.d.
	Er L	n.d.	594±90	n.d.	n.d.	n.d.
	Yb L	n.d.	834±66	n.d.	n.d.	n.d.
	Au L	n.d.	n.d.	n.d.	n.d.	n.d.
	Pb L %	4.06±0.07	6.08±0.12	0.38±0.03	1.51±0.04	1.65±0.05
	Th L %	1.74±0.04	2.56±0.06	0.08±0.01	1.00±0.04	1.32±0.06
	U L %	11.88±0.26	16.44±0.64	1.35±0.05	12.75±0.32	17.32±0.50

All values in ppm (± Σ uncertainty), unless indicated as wt%. Elements not detected are denoted with n.d.

Appendix G: EPMA WDS Maps Data from PIXE Samples

The maps in this section were obtained in order to confirm elements found in low concentrations (i.e. from weak spectra) in the PIXE study (Chapter 4). However, as can be seen from the WDS maps presented here, PIXE region analyses provided a far more accurate confirmation.

DFN10

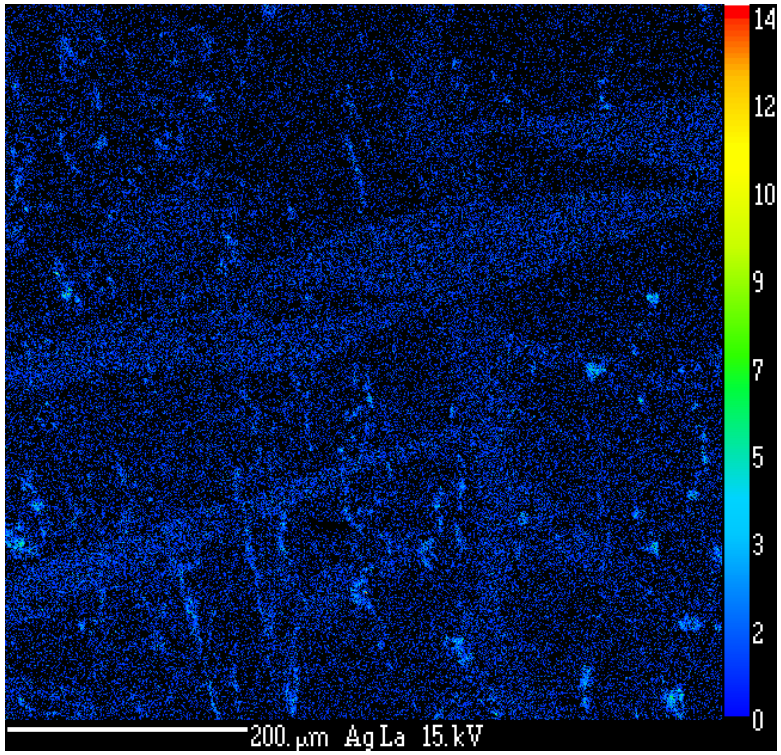

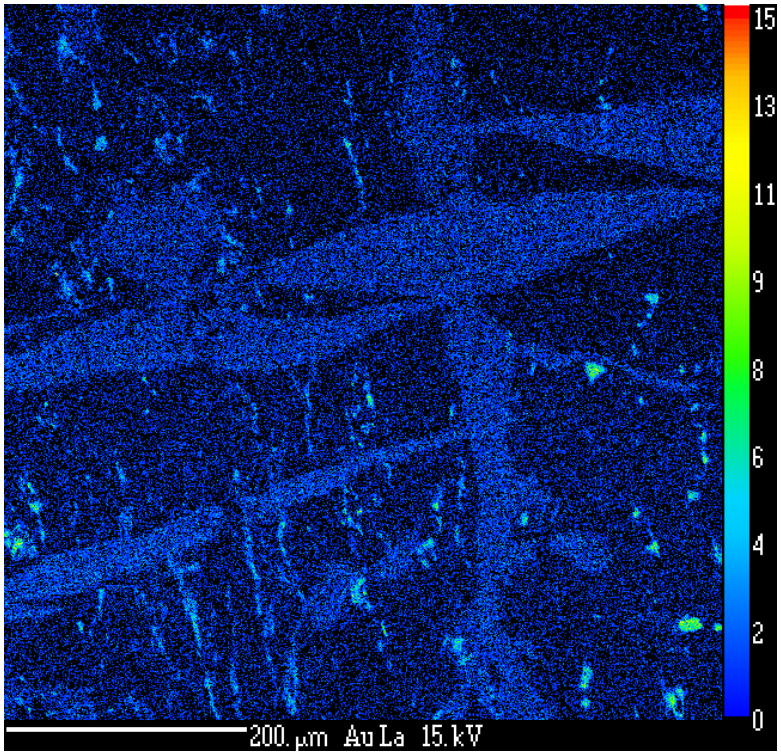

LGM3

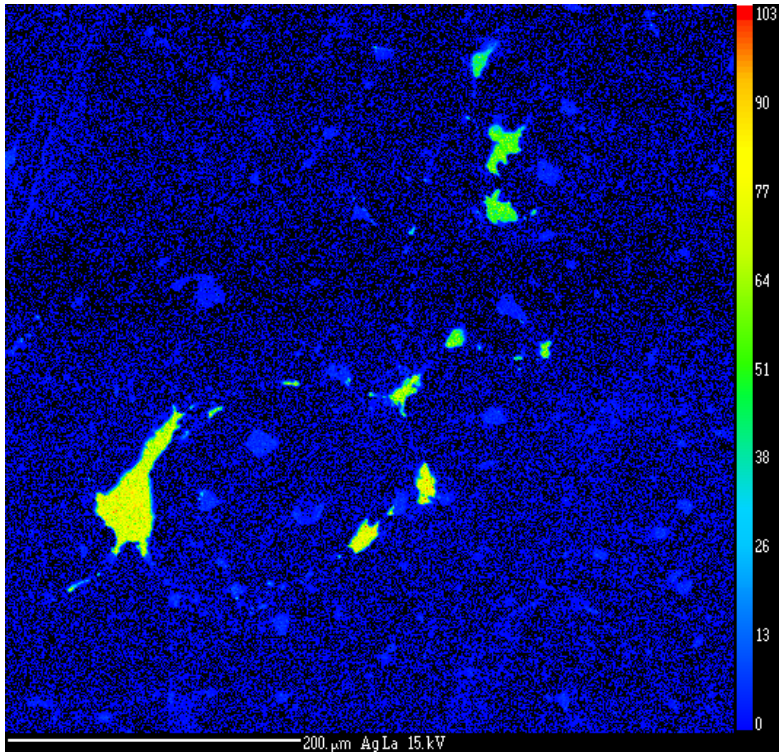
103
90
77
64
51
38
26
13
0
200.µm AgLa 15.kV

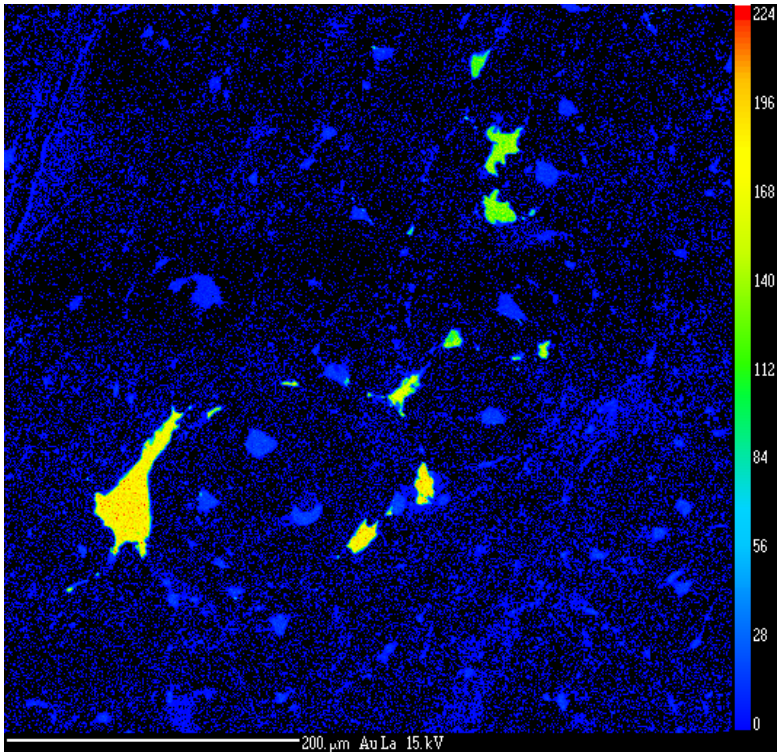
224
196
168
140
112
84
56
28
0
200.µm AuLa 15.kV

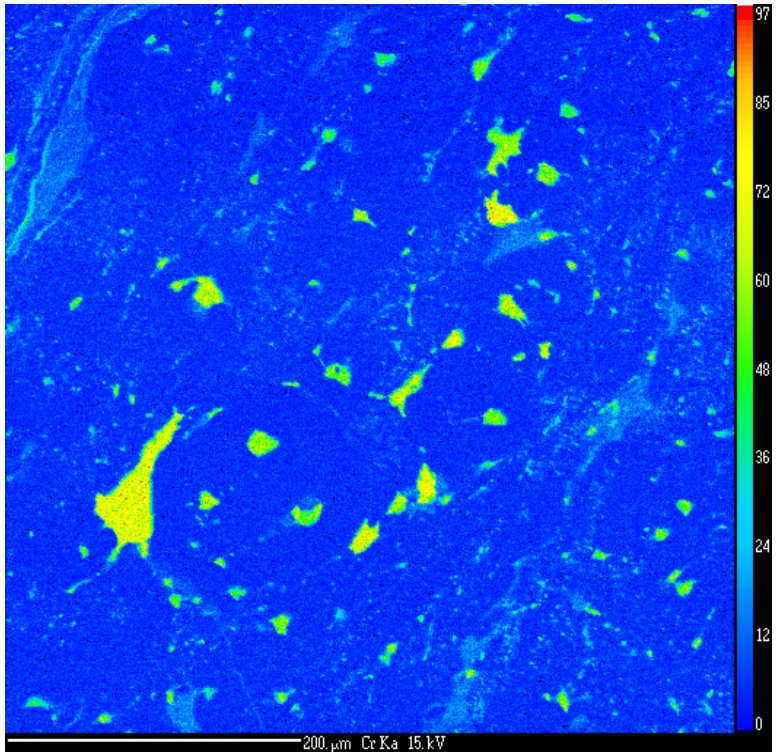
97
85
72
60
48
36
24
12
0
200. µm Cr Ka 15. kV

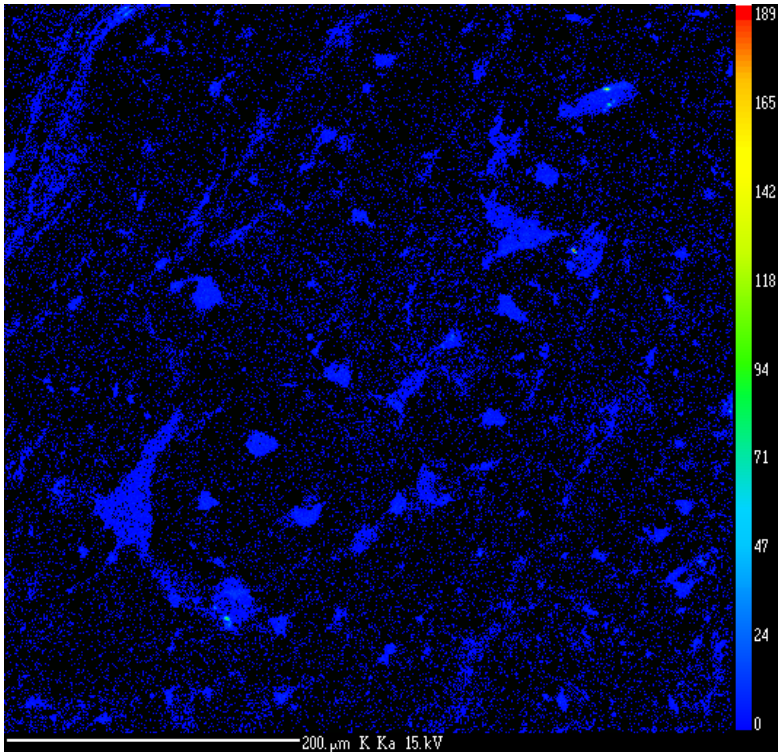
189
165
142
118
94
71
47
24
0
200. µm K Ka 15. kV

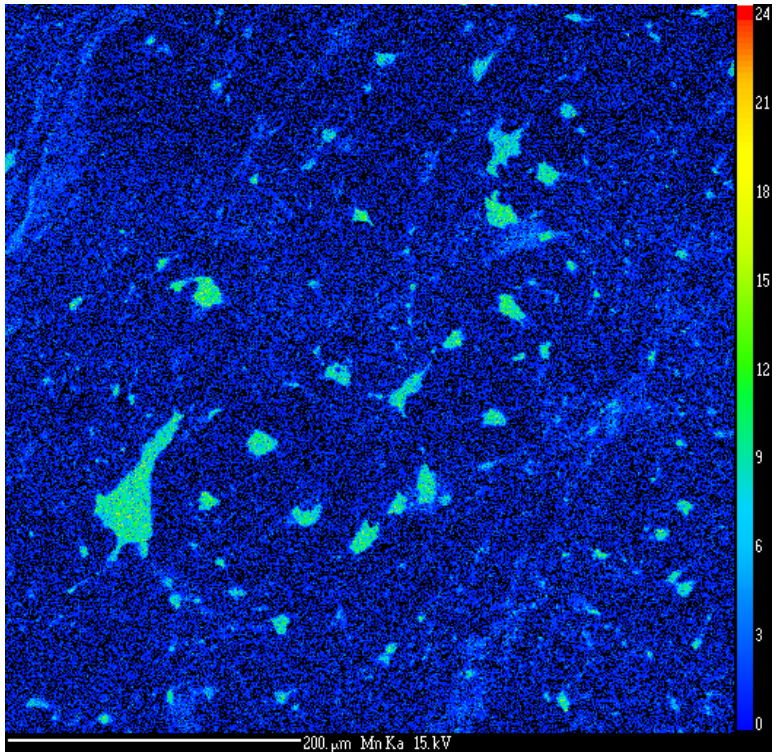
24
21
18
15
12
9
6
3
0
200. µm Mn Ka 15. kV

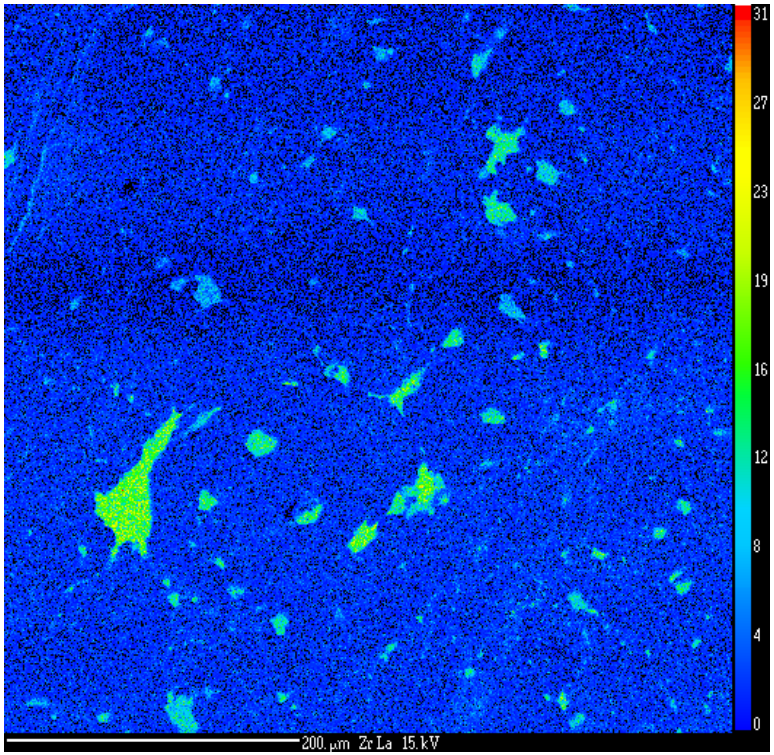
31
27
23
19
16
12
8
4
0
200. µm Zr La 15. kV

PSGM

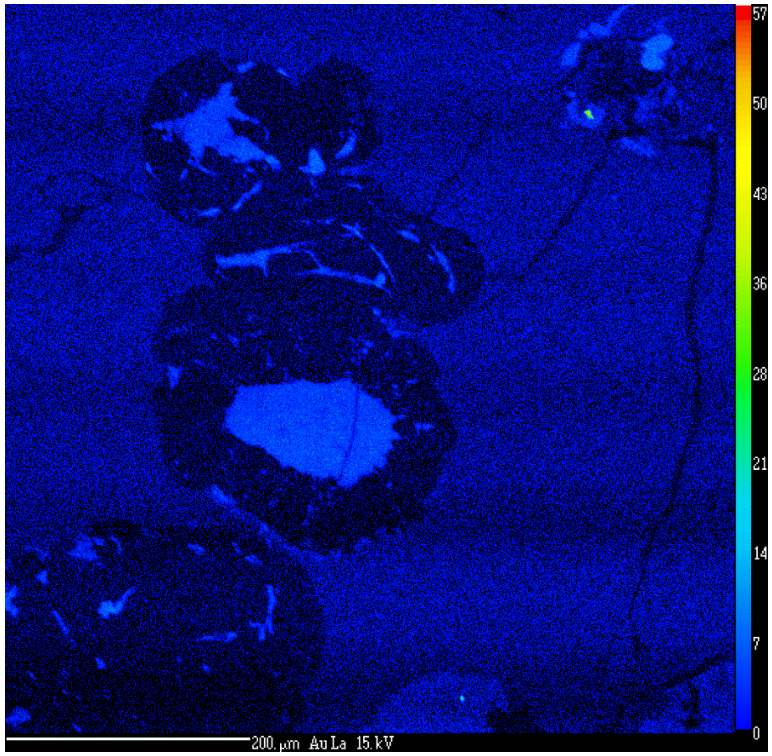
57
50
43
36
28
21
14
7
0
200.µm AuLa 15.kV

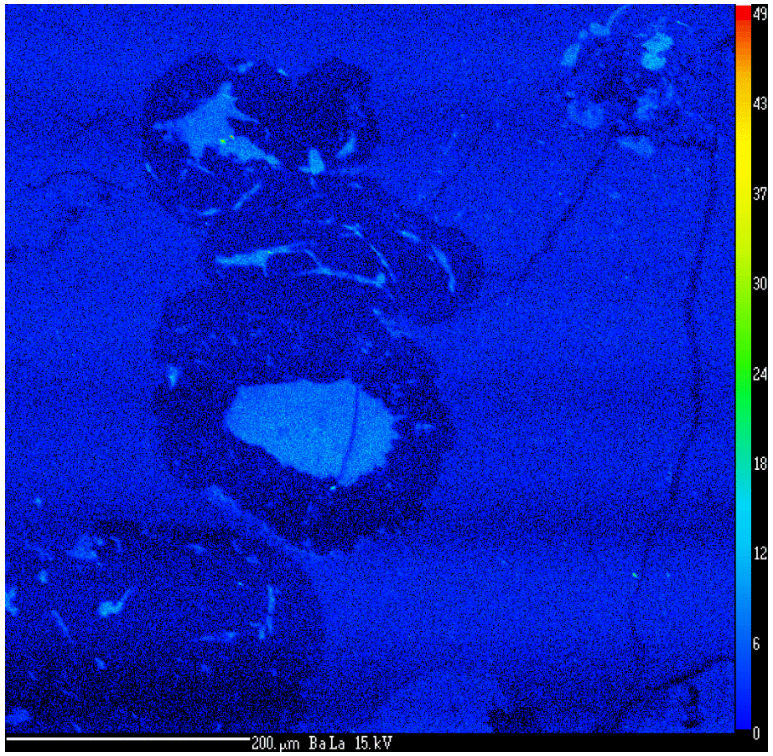
49
43
37
30
24
18
12
6
0
200.µm BaLa 15.kV

Appendix H: CCVD Supplementary Data

XRF results for the uraniferous powders used in CCVD reactions

Table 1 below shows the full XRF analyses (major and trace elements) of the uraniferous powders used in CCVD reactions.

Table1a: XRF data for uraniferous powders used in Chapter 5

Major Elements								
wt%	**DH034 <32µm**	**IDAM10 <32µm**	**HILG19 <32µm**	**HILG13 <32µm**	**DH034 32 - 75µm**	**IDAM10 32 - 75µm**	**HILG19 32 - 75µm**	**HILG13 32 - 75µm**
SiO_2	76.51	45.51	60.22	68.27	77.05	45.79	61.58	72.78
Al_2O_3	11.18	8.18	16.74	14.23	10.99	7.78	17.4	13.03
Fe_2O_3	0.13	1.54	0.34	0.32	0.13	1.6	0.3	0.18
FeO	1.07	12.47	2.72	2.62	1.06	12.95	2.41	1.43
MnO	0.03	0.52	0.06	0.01	0.03	0.54	0.04	0.01
MgO	0.68	3.75	0.87	0.2	0.75	3.91	0.72	0.14
CaO	1.55	21.22	3.59	0.83	1.48	21.17	2.09	0.73
Na_2O	1.77	1.27	2.93	2.1	1.78	1.19	2.95	1.97
K_2O	5.53	0.27	8.9	8.66	5.29	0.24	9.76	8.03
TiO_2	0.1789	0.0778	0.4379	0.1994	0.1932	0.081	0.3355	0.1374
P_2O_5	0.37	1.66	2.2	0.71	0.31	1.3	1.14	0.47
Cr_2O_3	-0.0001	0.002	-0.0013	-0.0087	-0.0008	0.0113	-0.005	-0.005
NiO	-0.0014	0.0043	-0.0012	0.0014	0.0022	0.0011	-0.0009	-0.0016
TOTAL	99	96.47	99	98.15	99.07	96.55	98.71	98.9
LOI	0.93	0.42	1.02	1.29	0.99	0.5	1.12	0.71

Table1b: XRF data for uraniferous powders used in Chapter 5

Minor Elements								
(ppm)	**DH034 <32µm**	**IDAM10 <32µm**	**HILG19 <32µm**	**HILG13 <32µm**	**DH034 32 - 75µm**	**IDAM10 32 - 75µm**	**HILG19 32 - 75µm**	**HILG13 32 - 75µm**
Sc	6.6	140.74	9.56	7.61	10.41	143.62	8.6	4.02
V	19.92	28.72	27.38	18.46	19.6	23.22	24.55	10.67
Cr	9.26	39.56	-3.93	6.24	5.53	27.71	6.01	6.16
Co	10.22	43.46	2.51	3.74	3.55	39.77	5.79	3.77
Ni	5.4	13.55	5.32	9.01	4.82	10.42	2.05	3.18
Cu	13.31	16.27	70.57	43.59	8.89	14.55	66.16	21.1
Zn	6.4	126	19.05	5.04	12.66	126.42	17.57	2.83
Ga	14.55	27.79	19.84	19.73	14.45	26.72	19.58	16.42
Rb	301.67	-25.06	415.1	382.09	302.11	-20.17	435.4	352.35
Sr	62.86	71.61	108.2	230.44	60.55	68.24	104.95	135.62
Y	510.91	358.07	253.64	86.65	309.41	303.9	130.79	58.98
Zr	297.89	34.07	330.4	47.81	203.62	33.64	305	91.97
Nb	33.55	12.71	22.4	44.27	27.31	9.94	18.16	20.64
Mo	6.25	12.4	449.03	227.17	2.71	10.96	176.04	110.83
Ba	246.87	16.44	411.25	489.02	232.93	6.34	456.51	416.63
Pb	214.71	453.15	131.39	151.85	131.78	358.12	131.18	89.41
Th	280.82	254.97	87.81	208.8	153.99	224.28	68.39	80.08
U	2445.83	6729.08	504.77	7904.27	1347.55	5293.85	419.06	3251.84

CCVD Experiment Data

Table 2 reflects the mass changes that were recorded for the various CCVD experiments. For each sample, experiments were performed in triplicate at: 300, 450 and 600°C. The average of the three experiments, at each temperature, was represented in Figures 2, 3 and 4 in the manuscript.

Table 2a: Experiment mass changes recorded for each CCVD experiment.

CCVD Experiment Results Table 1, <32 µm powders									
Experiment Number	Temperature °C	Sample	Boat #	Sample Mass Before (g)	Sample and Boat Mass After (g)	Boat Mass (g)	Sample Mass After (g)	Mass of Product (g)	% Change
CVD36	300	IDAM10, <32 µm	3	0.1009	1.7568	1.6565	0.1003	-0.0006	-0.59%
CVD37	300	IDAM10, <32 µm	1	0.0993	1.9591	1.8600	0.0991	-0.0002	-0.20%
CVD38	300	IDAM10, <32 µm	3	0.0997	1.7560	1.6564	0.0996	-0.0001	-0.10%
CVD72	450	IDAM10, <32 µm	3	0.1003	1.7566	1.6562	0.1004	0.0001	0.10%
CVD73	450	IDAM10, <32 µm	1	0.1002	1.9602	1.8601	0.1001	-0.0001	-0.10%
CVD74	450	IDAM10, <32 µm	3	0.0999	1.7566	1.6564	0.1002	0.0002	0.25%
CVD24	600	IDAM10, <32 µm	1	0.0999	1.9809	1.8600	0.1209	0.0210	21.02%
CVD26	600	IDAM10, <32 µm	3	0.0998	1.7853	1.6565	0.1288	0.0290	29.06%
CVD27	600	IDAM10, <32 µm	1	0.1008	1.9891	1.8600	0.1291	0.0283	28.08%
CVD48	300	DH034, <32 µm	3	0.0994	1.7561	1.6565	0.0996	0.0002	0.20%
CVD49	300	DH034, <32 µm	1	0.0998	1.9599	1.8602	0.0997	-0.0001	-0.10%
CVD50	300	DH034, <32 µm	3	0.1003	1.7566	1.6564	0.1002	-0.0001	-0.10%
CVD82	450	DH034, <32 µm	3	0.1005	1.7578	1.6565	0.1013	0.0008	0.80%
CVD83	450	DH034, <32 µm	1	0.0997	1.9611	1.8604	0.1007	0.0010	1.00%
CVD84	450	DH034, <32 µm	3	0.1000	1.7572	1.6567	0.1005	0.0005	0.50%
CVD111	600	DH034, <32 µm	1	0.1002	1.9660	1.8603	0.1057	0.0055	5.49%
CVD112	600	DH034, <32 µm	3	0.1001	1.7684	1.6565	0.1119	0.0118	11.79%
CVD113	600	DH034, <32 µm	1	0.0998	1.9704	1.8605	0.1099	0.0101	10.12%
CVD114	600	DH034, <32 µm	3	0.1000	1.7717	1.6565	0.1152	0.0152	15.20%
CVD57	300	HILG19, <32 µm	1	0.0996	1.9595	1.8601	0.0994	-0.0002	-0.20%
CVD58	300	HILG19, <32 µm	3	0.0994	1.7555	1.6563	0.0992	-0.0002	-0.20%
CVD59	300	HILG19, <32 µm	1	0.1003	1.9598	1.8601	0.0997	-0.0006	-0.60%
CVD88	450	HILG19, <32 µm	3	0.1002	1.7519	1.6563	0.0956	-0.0046	-4.59%
CVD89	450	HILG19, <32 µm	1	0.1002	1.9653	1.8602	0.1051	0.0049	4.89%
CVD90	450	HILG19, <32 µm	3	0.1000	1.7635	1.6565	0.1070	0.0070	7.00%
CVD105	600	HILG19, <32 µm	1	0.1000	2.0438	1.8603	0.1835	0.0835	83.50%
CVD106	600	HILG19, <32 µm	3	0.1001	1.8510	1.6565	0.1945	0.0944	94.31%
CVD107	600	HILG19, <32 µm	1	0.1002	2.0334	1.8603	0.1731	0.0729	72.75%
CVD66	300	HILG13, <32 µm	3	0.1004	1.7566	1.6561	0.1005	0.0001	0.10%
CVD67	300	HILG13, <32 µm	1	0.1003	1.9603	1.8599	0.1004	0.0001	0.10%
CVD68	300	HILG13, <32 µm	3	0.1000	1.7565	1.6563	0.1002	0.0002	0.20%
CVD94	450	HILG13, <32 µm	3	0.0999	1.7652	1.6563	0.1089	0.0090	9.01%
CVD95	450	HILG13, <32 µm	1	0.0999	1.9652	1.8601	0.1051	0.0052	5.21%
CVD96	450	HILG13, <32 µm	3	0.1001	1.7620	1.6563	0.1057	0.0056	5.59%
CVD97	600	HILG13, <32 µm	1	0.1001	2.0697	1.8602	0.2095	0.1094	109.29%
CVD99	600	HILG13, <32 µm	1	0.0998	2.1315	1.8604	0.2711	0.1713	171.64%
CVD100	600	HILG13, <32 µm	3	0.0996	1.8948	1.6566	0.2382	0.1386	139.16%

Table 2a: Experiment mass changes recorded for each CCVD experiment

CCVD Experiment Results Table 1, 3 2- 75 µm powders									
Experiment Number	Temperature °C	Sample	Boat #	Sample Mass Before (g)	Sample and Boat Mass After (g)	Boat Mass (g)	Sample Mass After (g)	Mass of Product (g)	% Change
CVD33	300	IDAM10, 32 - 75 µm	1	0.1002	1.9599	1.8600	0.0999	-0.0003	-0.30%
CVD34	300	IDAM10, 32 - 75 µm	3	0.0993	1.7556	1.6563	0.0993	0.0000	0.00%
CVD35	300	IDAM10, 32 - 75 µm	1	0.1008	1.9603	1.8601	0.1002	-0.0006	-0.60%
CVD30	450	IDAM10, 32 - 75 µm	1	0.1001	1.9604	1.8601	0.1003	0.0002	0.20%
CVD31	450	IDAM10, 32 - 75 µm	3	0.1058	1.7622	1.6562	0.1060	0.0002	0.19%
CVD32	450	IDAM10, 32 - 75 µm	1	0.0997	1.9600	1.8601	0.0999	0.0002	0.20%
CVD28	600	IDAM10, 32 - 75 µm	3	0.1006	1.7634	1.6564	0.1070	0.0064	6.36%
CVD20	600	IDAM10, 32 - 75 µm	1	0.0974	1.9758	1.8601	0.1157	0.0183	18.79%
CVD29	600	IDAM10, 32 - 75 µm	1	0.0997	1.9857	1.8603	0.1254	0.0257	25.78%
CVD45	300	DH034, 32 - 75 µm	1	0.1013	1.9615	1.8602	0.1013	0.0000	0.00%
CVD46	300	DH034, 32 - 75 µm	3	0.1005	1.7567	1.6563	0.1004	-0.0001	-0.10%
CVD47	300	DH034, 32 - 75 µm	1	0.1006	1.9605	1.8602	0.1003	-0.0003	-0.30%
CVD78	450	DH034, 32 - 75 µm	3	0.0998	1.7575	1.6565	0.1010	0.0012	1.20%
CVD80	450	DH034, 32 - 75 µm	3	0.1001	1.7572	1.6564	0.1008	0.0007	0.70%
CVD81	450	DH034, 32 - 75 µm	1	0.1004	1.9609	1.8600	0.1009	0.0005	0.50%
CVD16	600	DH034, 32 - 75 µm	1	0.1001	1.9609	1.8601	0.1008	0.0007	0.70%
CVD18	600	DH034, 32 - 75 µm	3	0.1017	1.7589	1.6564	0.1025	0.0008	0.81%
CVD19	600	DH034, 32 - 75 µm	1	0.1014	1.9625	1.8602	0.1023	0.0010	0.95%
CVD54	300	HILG19, 32 - 75 µm	3	0.0999	1.7561	1.6565	0.0996	-0.0003	-0.30%
CVD55	300	HILG19, 32 - 75 µm	1	0.1000	1.9597	1.8599	0.0998	-0.0002	-0.20%
CVD56	300	HILG19, 32 - 75 µm	3	0.0997	1.7558	1.6563	0.0995	-0.0002	-0.20%
CVD85	450	HILG19, 32 - 75 µm	1	0.1002	1.9639	1.8602	0.1037	0.0035	3.49%
CVD86	450	HILG19, 32 - 75 µm	3	0.1000	1.7561	1.6566	0.0995	-0.0005	-0.50%
CVD87	450	HILG19, 32 - 75 µm	1	0.0999	1.9640	1.8604	0.1036	0.0037	3.70%
CVD108	600	HILG19, 32 - 75 µm	3	0.1001	1.8746	1.6564	0.2182	0.1181	117.98%
CVD109	600	HILG19, 32 - 75 µm	1	0.0998	2.0493	1.8603	0.1890	0.0892	89.38%
CVD110	600	HILG19, 32 - 75 µm	3	0.1003	1.8936	1.6567	0.2369	0.1366	136.19%
CVD63	300	HILG13, 32 - 75 µm	1	0.1007	1.9605	1.8601	0.1004	-0.0003	-0.30%
CVD64	300	HILG13, 32 - 75 µm	3	0.0995	1.7559	1.6563	0.0996	0.0001	0.10%
CVD65	300	HILG13, 32 - 75 µm	1	0.1005	1.9605	1.8601	0.1004	-0.0001	-0.10%
CVD91	450	HILG13, 32 - 75 µm	1	0.1000	1.9614	1.8600	0.1014	0.0014	1.40%
CVD92	450	HILG13, 32 - 75 µm	3	0.1003	1.7578	1.6565	0.1013	0.0010	1.00%
CVD93	450	HILG13, 32 - 75 µm	1	0.0999	1.9611	1.8602	0.1009	0.0010	1.00%
CVD102	600	HILG13, 32 - 75 µm	3	0.1000	1.7748	1.6568	0.1180	0.0180	18.00%
CVD103	600	HILG13, 32 - 75 µm	1	0.1001	1.9746	1.8603	0.1143	0.0142	14.19%
CVD104	600	HILG13, 32 - 75 µm	3	0.1000	1.7750	1.6563	0.1187	0.0187	18.70%

Mass of Product formed vs Elemental Concentrations for 32 – 75 µm powders

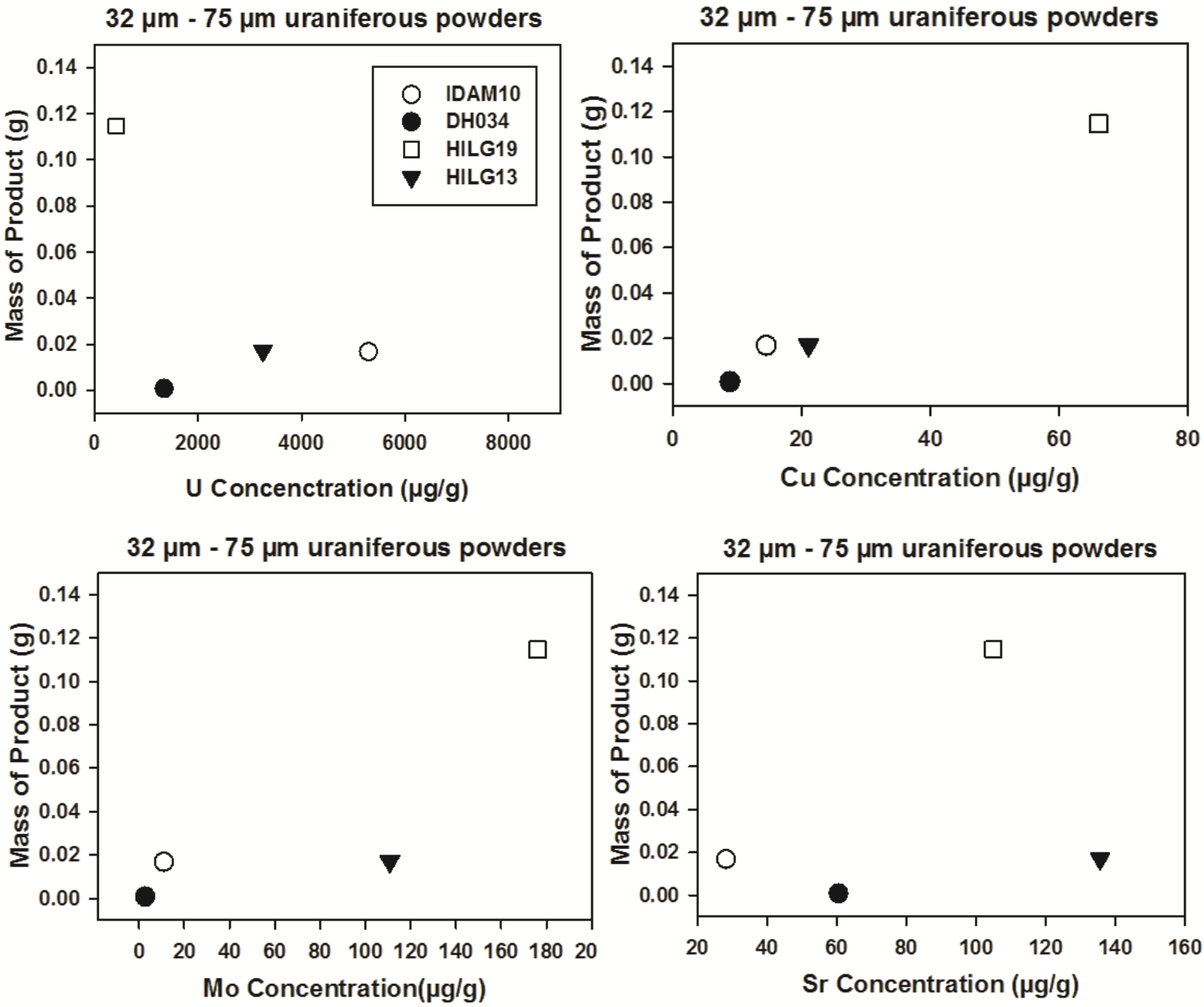

Figure 1 above shows the 32 – 75 µm data of the U, Cu, Mo and Sr concentrations vs the mass of product formed. The <32 µm data for the same types are displayed in Chapter 5

ICP-OES Data from initial and leached samples

Table 3a showing concentrations of U, Mo, Cu, As and Sr as determined by ICP-OES of microwave digested HILG19 powders

Microwave Digestion					
	U	**Mo**	**Cu**	**As**	**Sr**
32 um	8.31	3.795	1.112	0.307	1.212
dilution considered (mg/Kg)	831	379.5	111.2	30.7	121.2
75 um	6.968	2.94	0.906	0.292	1.085
dilution considered (mg/Kg)	696.8	294	90.6	29.2	108.5

Table 3b showing concentrations of U, Mo, Cu, As and Sr as determined by ICP-OES of solution created by leaching HILG19 powders with $CaHCO_3$

Extraction using $CaHCO_3$					
	U	**Mo**	**Cu**	**As**	**Sr**
32 um	16.08	0.324	0.026	0.113	0.054
dilution considered (mg/Kg)	402	8.1	0.65	2.825	1.35
75 um	14.49	0.299	0.0295	0.123	0.0515
dilution considered (mg/Kg)	362.25	7.475	0.7375	3.075	1.2875

Laser Raman Data Showing change in carbon signature of experimental products

Figure 2 displaying the increasingly graphitic nature of CCVD products as reaction temperature was raised.

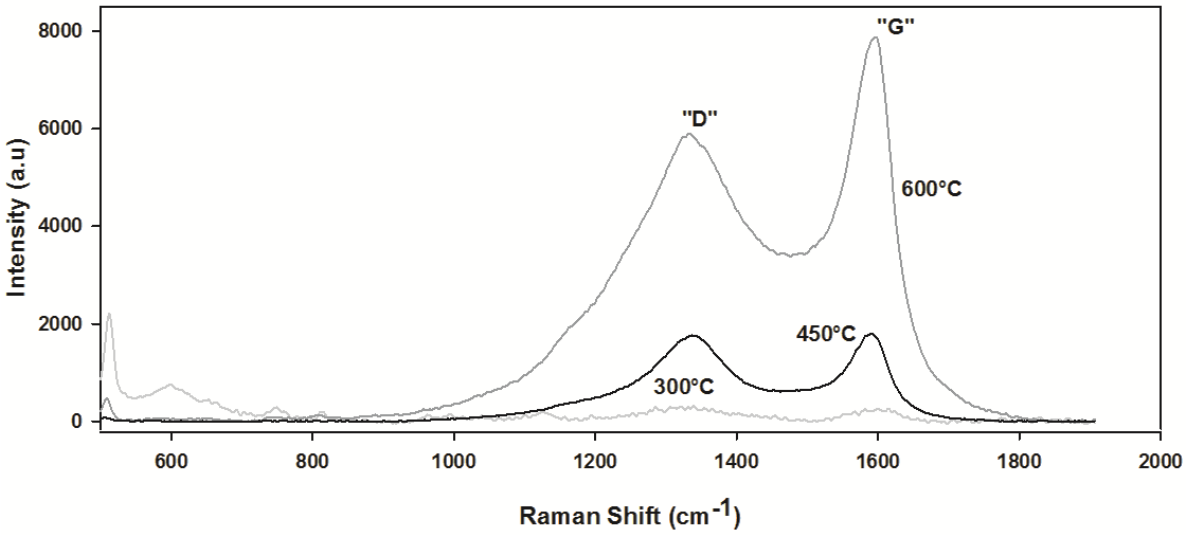

Figure 2a. Raman graph of HILG19 <32 µm CCVD products, at successively higher temperatures the intensity of the "G" peak increased in relation to the "D" peak.

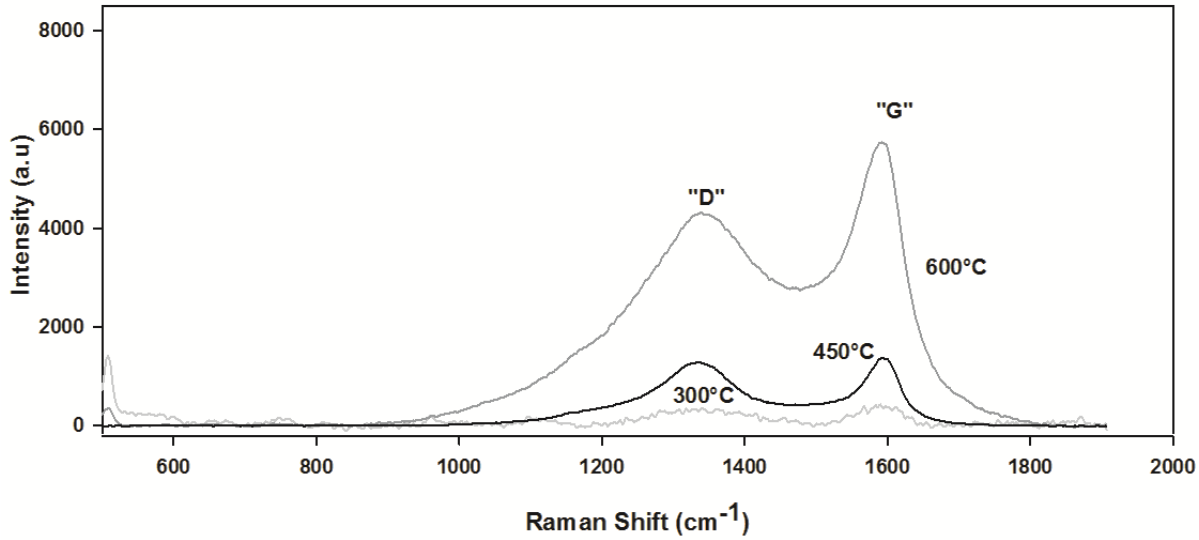

Figure 2b. Raman graph of HILG19 32 - 75 µm CCVD products, at successively higher temperatures the intensity of the "G" peak increased in relation to the "D" peak.

TGA Graphs

TGA first derivative graphs showing the thermal properties of unreacted HILG19 32 – 75 µm powder (Figure 4a) compared to 450 and 600 °C products that formed onto the same substrate (Figure 4(b)).

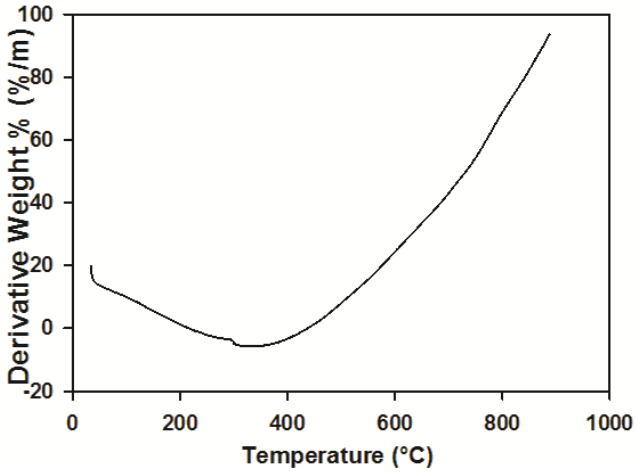

Figure 4a. TGA first derivative graph of unreacted HILG19 32 – 75 µm powder

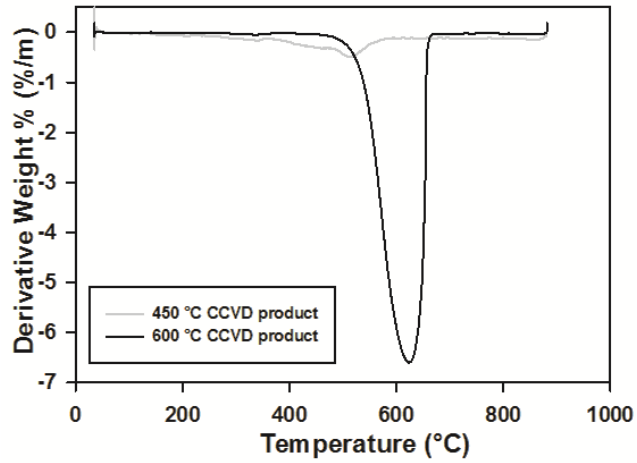

Figure 4b. TGA first derivative of 450 and 600°C CCVD products formed onto HILG19 32 – 75 µm powders

Appendix I: µCT and Auto-SEM supplementary Data

Table 1 Showing Auto-SEM EDS results calculated for the 19 stitched fields from Chapter 6

Mineral	Area %	Weight %	Grain Size (µm)	Grain Size Std Dev (µm)	Average Composition
Quartz	44.04	58.08	344.28	703.97	O 53.47; Si 46.53;
Hydrocarbon	35.03		268.89	472.26	
Kaolinite	5.58	7.50	318.29	161.64	O 50.82; Si 25.05; Al 24.13;
Pyrophyllite	4.92	6.87	134.06	119.60	O 51.34; Si 30.82; Al 17.84;
Muscovite	4.78	6.73	171.26	235.98	O 47.09; Al 22.33; Si 22.16; K 8.41; F 0;
Illite	1.96	2.64	94.62	57.77	O 48.8; Si 23.56; Al 23.28; K 4.37;
Gold	1.60	12.40	190.91	138.45	Au 100;
Pyrite	1.05	2.61	312.25	305.42	S 45.79; Fe 41.88;
Uraninite	0.35	1.57	129.63	17.76	U 85.69; O 14.31;
Greenockite	0.16	0.39	65.55	12.48	Cd 71.69; S 28.31;
Chamosite (Chlorite)	0.08	0.13	200.05	27.79	O 44.39; Al 19.95; Fe 17.93; Si 17.73;
Chalcopyrite	0.07	0.14	93.26	60.13	S 34.72; Fe 34.26; Cu 31.02;
Montmorillonite	0.06	0.07	63.80	0.00	O 53.53; Si 33.98; Al 12.49;
Fe Oxide	0.04	0.07	65.72	13.16	Fe 75.44; O 24.56;
Wavellite/Trolleite	0.04	0.05	151.11	56.69	O 58.94; Al 25.36; P 15.7;
Chloritoid	0.03	0.06	65.95	13.92	O 45.03; Al 23.77; Si 16.93; Fe 14.19; Mg 0.07;
Talc	0.03	0.04	73.74	26.68	O 52.78; Al 23.19; Si 16.3; Mg 7.72;
Rutile	0.02	0.03	71.72	33.62	Ti 59.61; O 40.39;
Other	0.16	0.62			
Total	**100.00**	**100.00**			

For high resolution petrographic images of Figure 6.2, 6.4 & 6.6 see digital Appendix I.

Appendix J: Solvothermal Supplementary Data

Experiment Data

Experiment Number	Solution	Pressure Added (kPa N_2 (g))	Pressure during reaction (kPa)	Solid Sample Mass Before (g)	Sample Mass on Filter Paper	Filter Paper Mass	Sample Mass After	Change	%
Solvo7	0.05 M Sucr only	-	1000	0.0000	1.7627	1.5807	0.1820	0.1820	81.80%
Solvo8	0.05 M Sucr + HILG19 <32 µm	-	1000	0.0992	1.7345	1.5003	0.2342	0.1350	76.58%
Solvo9	0.05 M Sucr + HILG13 <32 µm	-	1000	0.0999	1.7168	1.5163	0.2005	0.1006	79.95%
Solvo10	0.05 M Sucr + HILG19 <32 µm	400	1200	0.0999	1.8185	1.5174	0.3011	0.2012	69.89%
Solvo11	0.05 M Sucr + HILG19 <32 µm	800	1800	0.1001	1.8298	1.5011	0.3287	0.2286	67.13%
Solvo12	0.05 M Sucr + HILG13 <32 µm	800	1800	0.1003	1.8280	1.6434	0.1846	0.0843	81.54%
Solvo13	0.05 M Sucr + HILG13 <32 µm	400	1200	0.1001	1.9528	1.6000	0.3528	0.2527	64.72%
Solvo14	0.05 M Sucr + HILG13 <32 µm	400	1200	0.1000	1.8937	1.5457	0.3480	0.2480	65.20%
Solvo15	0.05 M Sucr + HILG13 <32 µm	800	1800	0.1003	1.9577	1.5772	0.3805	0.2802	61.95%
Solvo16	0.05 M Sucr + HILG19 <32 µm	800	1800	0.1001	1.9042	1.5446	0.3596	0.2595	64.04%
Solvo17	0.05 M Sucr + HILG19 <32 µm	Sample Lost							
Solvo18	0.05 M Sucr + HILG19 <32 µm	400	1200	0.1000	2.0241	1.6826	0.3415	0.2415	65.85%
Solvo19	0.05 M Sucr + HILG19 <32 µm	-	1000	0.1003	2.0222	1.6076	0.4146	0.3143	58.54%
Solvo20	0.05 M Sucr + HILG13 <32 µm	-	1000	0.1000	1.8753	1.5627	0.3126	0.2126	68.74%
Solvo21	0.05 M Sucr + HILG19 <32 µm	Sample Lost							
Solvo22	0.05 M Sucr + HILG13 <32 µm + 0.1	800	1800	0.1000	Not filtered due to acid content				
Solvo23	0.1 M Aurochl. Acid + HILG19 <32 µm	800	1800	0.1001	Not filtered due to acid content				

ICP-OES Data

Experiment Number/Solution	**Concentration of Gold (mg/L)**
Original Gold Solution	9540
Estimated Concentration in 10 mL + 60 mL sucrose/deionised water solution	1362
Solvo 22	0.55
Solvo 23	319.25

TEM EDS Spectra for Gold Particle in Figure 7.8